

---

---



Università degli Studi di Catania



Scuola Superiore di Catania

International Ph.D. course in Nanoscience: Cycle XXIII

---

# Local transport properties in graphene for electronic applications

A thesis submitted in partial fulfilment of the requirements for the  
degree of:

Doctor of Philosophy in Nanoscience

by

Sushant Sudam Sonde

Coordinators: Prof. Emanuele Rimini,  
Prof.ssa. Maria Grazia Grimaldi

Tutors: Dr. Vito Raineri,  
Dr. Filippo Giannazzo

---

In cooperation with



CNR IMM

Istituto per la Microelettronica e Microsistemi  
Strada VIII, 5, 95121, Catania, Italy

---

---



# Abstract

In view of possible applications in electrostatically tunable two-dimensional field-effect devices, this thesis is aimed at discussing electronic properties in substrate-supported graphene. Original methods based on various variants of Scanning Probe Microscopy techniques are utilized to analyze graphene exfoliated-and-deposited (DG) on  $\text{SiO}_2/\text{Si}$ ,  $\text{SiC}(0001)$  and high- $\kappa$  dielectric substrate (Strontium Titanate) as well as graphene grown epitaxially (EG) on  $\text{SiC}(0001)$ .

Scanning Capacitance Spectroscopy is discussed as a probe to evaluate the electrostatic properties (quantum capacitance, local density of states) and transport properties (local electron mean free path) in graphene. Furthermore, based on this method two important issues adversely affecting room temperature charge transport in graphene are addressed to elucidate the role of:

1. Lattice defects in graphene introduced by ion irradiation and
2. Charged impurities and Surface Polar Phonon scattering at the graphene /substrate interface.

Moreover, a comparative investigation of current transport across EG/ $\text{SiC}(0001)$  and DG/ $\text{SiC}(0001)$  interface by Scanning Current Spectroscopy and Torsion Resonance Conductive Atomic Force Microscopy is discussed to explain electrical properties of the so-called ‘buffer layer’ commonly observed at the interface of EG/ $\text{SiC}(0001)$ . This study also clarifies the local workfunction variation in EG due to electrically active buffer layer.

---

# Contents

<b>Abstract</b>	<b>ii</b>
<b>1 Introduction</b>	<b>1</b>
1.1 Nanoscale science and technology: A primer . . . . .	1
1.2 Nanoelectronics in retrospect . . . . .	4
1.3 Carbon materials for prospective nanoelectronics . . . . .	5
1.4 Graphene . . . . .	8
1.5 Graphene and other 2D Semiconductor structures . . . . .	9
1.6 Bandstructure of graphene and elementary electronic properties .	12
1.6.1 Cyclotron mass . . . . .	15
1.6.2 Density of states . . . . .	15
1.7 Graphene for electronics applications: Opportunities and challenges	16
1.8 Motivation and scope of thesis work . . . . .	17
<b>References</b>	<b>21</b>
<b>2 Experimental set-up</b>	<b>27</b>
2.1 Introduction . . . . .	27
2.2 Atomic Force Microscope . . . . .	28
2.2.1 Scanning capacitance microscopy and spectroscopy . . . .	30
2.2.1.1 The measuring principle . . . . .	31
2.2.1.2 Constant $\Delta V$ measurements . . . . .	32
2.2.2 Scanning Current Spectroscopy . . . . .	34
2.2.3 Torsion Resonance - Conductive Atomic Force Microscopy	35
2.3 Sample preparation . . . . .	35
2.3.1 Mechanical exfoliation . . . . .	35

2.3.1.1	Micro-Raman spectroscopy and atomic force microscopy . . . . .	36
2.3.1.2	Optical contrast microscopy . . . . .	40
2.3.2	Epitaxial growth . . . . .	42
2.3.2.1	Atomic force microscopy and transmission electron microscopy . . . . .	43
2.3.2.2	Torsion Resonance Conductive Atomic Force Microscopy . . . . .	44
2.4	Summary . . . . .	48
	<b>References</b>	<b>50</b>
<b>3</b>	<b>Local electrostatic and transport properties in graphene</b>	<b>55</b>
3.1	Introduction . . . . .	55
3.2	Screening length and quantum capacitance . . . . .	56
3.2.1	Nanoscale capacitance measurements on graphene . . . . .	57
3.2.2	The effectively biased area in graphene . . . . .	60
3.2.3	The quantum capacitance and local density of states in graphene . . . . .	63
3.2.4	Discussion . . . . .	68
3.2.5	Influence of dielectric environment . . . . .	69
3.2.5.1	Graphene on high- $\kappa$ . . . . .	70
3.2.5.2	Enhanced $A_{eff}$ . . . . .	70
3.3	Local electron mean free path by scanning capacitance spectroscopy	72
3.4	Summary . . . . .	75
	<b>References</b>	<b>77</b>
<b>4</b>	<b>Ion irradiation and defect formation in graphene</b>	<b>79</b>
4.1	Introduction . . . . .	79
4.2	Sample preparation . . . . .	80
4.3	Raman spectroscopic investigation . . . . .	81
4.4	Nanoscale capacitive behaviour . . . . .	89
4.4.1	Local Capacitance . . . . .	90
4.4.2	$A_{eff}$ and Fermi velocity . . . . .	92
4.5	Local electron mean free path and mobility . . . . .	94
4.6	Summary . . . . .	99
	<b>References</b>	<b>102</b>

## CONTENTS

---

<b>5</b>	<b>Local electrical properties of graphene/SiC(0001)</b>	<b>107</b>
5.1	Introduction . . . . .	107
5.2	Electrical properties of the graphene / 4H-SiC(0001) interface . .	108
5.2.1	Current transport across graphene/SiC interface . . . . .	109
5.2.2	Modified Schottky barrier height . . . . .	113
5.3	Effect on electrostatic properties . . . . .	115
5.4	Effect on the local transport properties . . . . .	119
5.4.1	Local electron mean free path . . . . .	121
5.4.2	Charge scattering at the graphene/substrate interface . .	125
5.5	Summary . . . . .	127
	<b>References</b>	<b>128</b>
<b>6</b>	<b>Conclusions</b>	<b>133</b>
6.1	Introduction . . . . .	133
6.2	Conclusions . . . . .	134
	<b>List of Publications</b>	<b>137</b>
	<b>Curriculum vitae</b>	<b>142</b>
	<b>Acknowledgments</b>	<b>145</b>



# List of Figures

- 1.1 Illustration of the carbon valence orbitals. (a) The three inplane  $\sigma$  ( $s$ ,  $p_x$ ,  $p_y$ ) orbitals in graphene and the  $\pi$  ( $p_z$ ) orbital perpendicular to the sheet. The inplane  $\sigma$  and the  $\pi$  bonds in the carbon hexagonal network strongly connect the carbon atoms and are responsible for the large binding energy and the elastic properties of the graphene sheet. The  $\pi$  orbitals are perpendicular to the surface of the sheet. The corresponding bonding and the antibonding  $\sigma$  bands are separated by a large energy gap of  $\sim 12$  eV (b), while the bonding and antibonding  $\pi$  states lie in the vicinity of the Fermi level ( $E_F$ ). Consequently, the  $\sigma$  bonds are frequently neglected for the prediction of the electronic properties of graphene around the Fermi energy. Dirac cones located at the six corners of the 2D Brillouin zone are illustrated in (c) (adopted from [44]). . . . . 9
  
- 1.2 Quantum Hall effect in graphene. The plateau in  $\sigma_{xy}$  at half integers of  $4e^2/h$  is a hallmark of massless Dirac fermions.  $\rho_{xx}$  vanishes for the same carrier concentrations. . . . . 11
  
- 1.3 Honeycomb lattice and the Brillouin zone in graphene. (a) the lattice structure in graphene is made of two interpenetrating triangular lattices ( $a_1$  and  $a_2$  are the lattice unit vectors and  $\delta_i$ ,  $i=1, 2, 3$  are the nearest-neighbor vectors), (b) corresponding Brillouin zone. The Dirac cones are located at the K and K' points (adopted from [49]). . . . . 12

1.4	Electronic band structure of graphene from ab-initio calculations. The bonding $\sigma$ and the antibonding $\sigma^*$ bands are separated by a large energy gap. The bonding $\pi$ (highest valence band) and the antibonding $\pi^*$ (lowest conduction band) bands touch at the K(K') points of the Brillouin zone. The Fermi energy ( $E_F$ ) is set to zero and $\phi$ indicates the work function (by the dashed horizontal line). Above the vacuum level $\phi$ , the states of the continuum are difficult to describe and merge with the $\sigma^*$ bands. The 2D hexagonal Brillouin zone is illustrated with the high-symmetry points $\Gamma$ , M, K and K' (adopted from [44]). . . . .	14
2.1	Interatomic force as a function of distance between tip and sample. Various modes of operation of AFM are also indicated. . . .	29
2.2	Experimental set-up for Scanning Capacitance Microscopy . . . .	31
2.3	Schematic block diagram of resonating circuit used for ultra high frequency capacitor sensor . . . . .	33
2.4	Schematic representation of (a) Conductive Atomic Force Microscopy, and (b) Torsion Resonance Conductive Atomic Force Microscopy applied to graphene. . . . .	34
2.5	(a) Optical microscopy of a few layers graphene sample, (b) MicroRaman spectra measured on some selected positions indicated by the red, green and blue dots in the optical image, and (c) Atomic force microscopy image of the flake. . . . .	37
2.6	(a) AFM height map of the few layers graphene sample and (b) height profile along the indicated line. . . . .	38
2.7	(a) Height of a few layers of graphene sheet versus the estimated number of layers in the sheet. (b) Force-distance curves measured on FLG and (c) on SiO <sub>2</sub> . The black curves are collected with the tip approaching to the surface, while the red ones with the curves retracting from the surface. (d) Schematic explanation of the offset affecting the Step-height between single layers of graphene and SiO <sub>2</sub> . . . . .	39
2.8	(a) AFM image and (b) height linescan for a single layer graphene flake deposited on 100 nm thick SiO <sub>2</sub> . (c) Optical microscopy on the same sample illuminated with light of 600 nm wavelength. (d) Illustration of the procedure to extract the optical contrast profile from the reflected light intensity. . . . .	41



## LIST OF FIGURES

---

2.9	Optical contrast as a function of the flake thickness (and the number of graphene layers) for samples deposited on 300 nm SiO <sub>2</sub> and illuminated with light of 400 nm (black triangles) and 600 nm (red squares) wavelengths. The lines represent the calculated contrast as a function of the number of layers. . . . .	41
2.10	MicroRaman spectra collected on several positions on the epitaxial graphene grown on 4H-SiC(0001) substrate. The spectrum collected on starting substrate (bare SiC) is also shown for comparison. . . . .	43
2.11	Estimation of number of graphene layers by etching graphitized SiC surface. The trenches are clearly seen in the phase images (a1), (b1) and (c1) (the scale bars are 5μm). The height profile taken over the etched regions on pristine 4H-SiC sample gives an estimation of overetched SiC. Progressively deeper trenches in (b) and (c) give an estimated 3, and 9 layers of graphene. . . . .	45
2.12	Fig. 3 High-resolution Transmission Electron Micrographs of graphitized 4H-SiC(0001) (a) Sample 1, and (b) Sample 2. Graphene layers appear evident on SiC substrate. . . . .	45
2.13	Torsion Resonance Atomic Force Microscopy map in (a) and the corresponding Torsion Resonance Conductive Atomic Force Microscopy map in (b). In (c) are shown histograms extracted from the current map in (b). Evaluated three regions (region with graphene coverage (curves (ii) and (iii)) and region devoid of graphene (curve (i)) are indicated distinctly. . . . .	47
2.14	TR morphology (a) and current map (b) collected on EG2 sample.	48
3.1	Schematic illustration of the experimental system, when the AFM tip is on SiO <sub>2</sub> (a) and on graphene (b) . . . . .	58
3.2	Typical set of 25 $ \Delta C $ - $V_g$ characteristics measured with the tip at a fixed position on SiO <sub>2</sub> (a) and at a fixed position on the graphene monolayer (b). In (c), set of 25 $ \Delta C $ - $V_g$ characteristics measured on an array of 5 × 5 different tip positions in the region across the graphene monolayer and SiO <sub>2</sub> . The red and green curves are the calculated average values, respectively. In the inserts, the histograms of $ \Delta C $ at fixed bias ( $V_g$ =-8 V) is reported. . . . .	61

3.3	On the left axis, the average ratio $N= \Delta C_{tot} / \Delta C_{MOS} $ between the capacitance variations measured with the tip on graphene and with the tip on $\text{SiO}_2$ , for samples with 300 nm oxide thickness (a) and 100 nm oxide thickness (b). On the right axis, the average screening radius $r_s$ calculated from $N(V_g)$ for the sample with 300 nm oxide thickness (a) and 100 nm oxide thickness (b). . . .	62
3.4	Screening charge density distribution for different values of the applied bias $V_g$ , for the sample with 300 nm oxide thickness (a) and 100 nm oxide thickness (c). Local potential on graphene $V_{gr}(r)$ for different values of $V_g$ , for the sample with 300 nm oxide thickness (b) and 100 nm oxide thickness (d). . . . .	65
3.5	Potential drop in graphene $\Delta V_{gr}$ (a), quantum capacitance $C_q$ (b), density of states DOS (c) versus $V_g$ for the sample with 300 nm oxide thickness (black line) and 100 nm oxide thickness (red line). In (d) the minimum area ADOS necessary to accommodate the charge induced by the bias $V_g$ , according to the density of states in graphene, is reported on the right scale, whereas the effective area determined from the data in Figure 3.3 is reported on the right scale. . . . .	67
3.6	The $r_s$ vs $V_g$ curves for all the tip positions on graphene (a) and, in the inset, the histogram of the $r_s$ values distribution for fixed $V_g=-5$ V. Similarly, in (b), the $C_q$ vs $V_g$ curves for all the tip positions and, in the inset, the histogram of the $C_q$ values distribution for fixed $V_g=-5$ V are shown. Finally, in (c), the DOS vs $V_g$ curves for all the tip positions and, in the inset, the histogram of the DOS values distribution for fixed $V_g=-5$ V are shown. . . . .	68
3.7	(a) Optical micrograph showing graphene deposited on STO. Monolayer region can be seen with lighter contrast in a multilayer stack. (b) Tapping mode AFM micrograph of a representative DG-STO flake and (c) corresponding height profile in a linescan on monolayer-SrTiO <sub>3</sub> region. . . . .	70
3.8	Representative characteristics obtained by Scanning Capacitance Spectroscopy (SCapS) on (a) graphene deposited on SrTiO <sub>3</sub> (DG-STO) and (b) graphene deposited on SiO <sub>2</sub> (DG-SiO <sub>2</sub> ). Two distinct families of curves correspond to tip position ‘on graphene’ and ‘on substrate’ as indicated. A typical scan comprises of an array of $5 \times 5$ positions with an inter-step distance of $1 \mu\text{m} \times 1 \mu\text{m}$ . .	71

## LIST OF FIGURES

---

3.9	$A_{eff}$ as evaluated from the local capacitive measurements on DG-STO and DG-SiO <sub>2</sub> as a function of $E_F$ is showed in (a). The corresponding $C_q$ is depicted in (b). A relative increase in $C_q$ of $\sim 10\times$ can be seen from the histograms in (c). . . . .	73
3.10	Local capacitance measurements (a) can be used to evaluate the electron mean free path in graphene (b) supported by insulating and/or semiinsulating substrates. . . . .	75
4.1	Typical optical (a) and AFM (b) images on a sample containing both monolayer (i) bilayer (ii) and multi-layer (iii) regions. The spots on the optical image indicate the spatial resolution of the Raman measurements. . . . .	81
4.2	Raman spectra on a single layer graphene not irradiated and irradiated with 500 keV C ions at $1\times 10^{13}$ , $2\times 10^{13}$ , $5\times 10^{13}$ and $1\times 10^{14}$ cm <sup>-2</sup> fluences. In the insert, the D peak for the four fluences is reported (here intensities are normalized). . . . .	83
4.3	AFM images acquired on $1\times 1$ $\mu\text{m}$ scan areas on SiO <sub>2</sub> and supported graphene for not irradiated samples and for irradiated (fluences of $1\times 10^{13}$ , $5\times 10^{13}$ and $1\times 10^{14}$ cm <sup>-2</sup> ). Power spectra of the AFM maps were calculated for all the samples and reported in a-d. . . . .	86
4.4	Raman spectra taken after $10^{14}$ ion/cm <sup>2</sup> irradiation in a single-, double- and multi-layer graphene pieces together with the spectrum of an as prepared single layer graphene . . . . .	87
4.5	Ratio of the D peak and G peak intensities ( $I_D/I_G$ ) as a function of the ion fluence for a single layer, a double layer and a multi-layer of graphene. . . . .	88
4.6	G' peak for the irradiated ( $10^{13}$ ions/cm <sup>2</sup> ) single and double layers together with the signals obtained in the D line region, duplicated in frequency to compare them with the second order signal. . . . .	89
4.7	SCapS curves obtained on (a) pristine graphene, (b) graphene irradiated with a fluence of $1\times 10^{13}$ ions/cm <sup>2</sup> , and (c) $1\times 10^{14}$ ions/cm <sup>2</sup> . . . . .	91
4.8	N (left axis) and $A_{eff}$ (right axis) obtained on (a) pristine graphene, and graphene irradiated with a fluence of (b) $1\times 10^{13}$ ions/cm <sup>2</sup> and (c) $1\times 10^{14}$ ions/cm <sup>2</sup> . . . . .	92

4.9	Histograms showing quantitative variations for (a) $N$ , (b) $A_{eff}$ and (c) $\nu_F$ . The cases for pristine graphene are depicted in (1), while (2) and (3) indicate the cases for graphene irradiated with a fluence of $1 \times 10^{13} \text{cm}^{-2}$ and $1 \times 10^{14} \text{cm}^{-2}$ respectively. The two distributions observed distinctly indicate probed sites that are defected and non-defected, especially, the broader distribution at lower values are associated with defected sites. . . . .	93
4.10	Density of states (left axis) and quantum capacitance per unit area (right axis) obtained on (a) pristine graphene, (b) graphene irradiated with a fluence of $1 \times 10^{13} \text{ions/cm}^2$ and (c) a fluence of $1 \times 10^{14} \text{ions/cm}^2$ . Distributions of DOS at fixed backgate bias ( $V_g=1 \text{ V}$ ) for (d) pristine graphene and graphene irradiated with fluences of (e) $1 \times 10^{13} \text{ions/cm}^2$ and (f) $1 \times 10^{14} \text{ions/cm}^2$ . . . . .	95
4.11	$ \Delta C $ vs $V_g$ measurements on arrays of several tip positions on (a) not irradiated graphene, and on irradiated graphene at fluences (b) $1 \times 10^{13}$ , and (c) $1 \times 10^{14} \text{cm}^{-2}$ , respectively. Curves measured with the tip on $\text{SiO}_2$ reported for comparison. Histograms of the capacitance values at $V_g=1 \text{ V}$ for (d) not irradiated graphene, and irradiated graphene at (e) $1 \times 10^{13}$ , and (f) $1 \times 10^{14} \text{cm}^{-2}$ . (g) Percentage of counts under peaks 1 and 2 in the distributions vs the irradiated fluence. . . . .	97
4.12	Local electron mean free path vs $V_g^{1/2}$ and $n^{1/2}$ for several tip positions on (a) not irradiated graphene and on irradiated graphene at fluences (b) $1 \times 10^{13}$ , and (c) $1 \times 10^{14} \text{cm}^{-2}$ . . . . .	98
4.13	Local mobility vs $V_g$ and $n$ for several tip positions on (a) not irradiated graphene, and on irradiated graphene at fluences (b) $1 \times 10^{13}$ , and (c) $1 \times 10^{14} \text{cm}^{-2}$ . Histograms of $\mu$ and $l$ at $V_g = 1 \text{ V}$ on (d) not irradiated graphene and (e,f) on irradiated graphene with the two fluences. . . . .	100
5.1	Schematic representation of graphene/substrate interface for (a) graphene grown epitaxially on 4H-SiC(0001) (EG), (b) graphene exfoliated and deposited on 4H-SiC(0001) (DG-SiC), and (c) graphene exfoliated and deposited on $\text{SiO}_2$ (DG-SiO <sub>2</sub> ). Commonly observed buffer layer between the last SiC bilayer and first graphene layer at the interface in EG is depicted in (a). Such buffer layer is absent in DG-SiC and DG-SiO <sub>2</sub> . . . . .	109

## LIST OF FIGURES

---

5.2	(a) Current map of DG on 4H-SiC(0001) at tip voltage of 1 V. The tip positions on graphene and on 4H-SiC are shown. (b) Typical set of SCurS I-V characteristics. Two distinct families of curves are associated with the tip positions on graphene and on 4H-SiC are indicated. . . . .	110
5.3	MicroRaman spectra collected on several positions on the epitaxial graphene grown on 4H-SiC(0001) substrate along with the spectrum collected on starting substrate (bare SiC) is also shown for comparison. The number of graphene layers was found to vary rapidly at micrometer scale. The estimated number of layers are depicted on each spectrum. . . . .	111
5.4	(a) Topography and (b) corresponding current map of EG on 4H-SiC(0001). The tip positions on regions covered by EG and on regions devoid of EG are indicated. The corresponding I-V curves are reported in (c). . . . .	112
5.5	Histograms of SBHs evaluated for Pt/graphene/4H-SiC and Pt/4H-SiC in the cases of (a) DG and (b) EG. . . . .	113
5.6	Band diagrams of graphene/4H-SiC(0001) Schottky contact for (a) DG-SiC(0001) and (b) EG-SiC(0001). In contrast to DG, due to presence of positively charged buffer layer, the EG film is negatively doped. . . . .	114
5.7	Tapping mode AFM micrograph of (a) a prototypical graphene flake deposited on 4H-SiC(0001) and (b) graphene epitaxially grown on 4H-SiC(0001). Corresponding linescan on a monolayer exfoliated graphene in (c) and TR-CAFM map on epitaxial graphene in (d). . . . .	116
5.8	A typical set of SCS curves obtained on (a) graphene deposited on 4H-SiC(0001), (b) graphene epitaxially grown on 4H-SiC(0001). Two families of curves corresponding to SCS signal (i) on graphene and (ii) on 4H-SiC(0001) can be distinguished. . . . .	118
5.9	Screening length as evaluated in DG and EG. Wider variations in $r_s$ for EG can be observed and are indicative of local variations in electrostatic properties in EG. . . . .	119
5.10	Local variations, as evaluated from screening length ( $r_s$ ), in quantum capacitance ( $C_q$ ) are shown in (a) and (b) while those in local density of states (LDOS) are shown in (c) and (d) for (i) DG and (ii) EG. . . . .	120

- 5.11 Representative characteristics obtained by SCapS on (a) graphene deposited on 4H-SiC(0001) (DG-SiC), (b) graphene epitaxially grown on 4H-SiC(0001) (EG-SiC), and (c) graphene deposited on SiO<sub>2</sub> (DG-SiO<sub>2</sub>). Two distinct families of curves correspond to tip placement (i) “on graphene” and (ii) “on substrate” are indicated. A typical scan comprises of an array of 5×5 positions with an interstep distance of 1×1 μm<sup>2</sup>. . . . . 122
- 5.12 Evaluated electron mean-free path in graphene ( $l_{gr}$ ) for (i) DG-SiC, (ii) EG-SiC, and (iii) DG-SiO<sub>2</sub> is depicted in (a). In (b) are depicted the corresponding histograms plotted at  $n_{Vg-n_0} = 1.5 \times 10^{11} \text{ cm}^{-2}$ . An average increase of  $\sim 4\times$  and  $\sim 1.5\times$  can be seen in  $l_{gr}$  for DG-SiC and EG-SiC, respectively, as compared to  $l_{gr}$  for DG-SiO<sub>2</sub>. . . . . 124
- 5.13 A representative graph of prominent limiting contributions to the room temperature electron mean free path in graphene evaluated for the cases of (a) DG-SiC and (b) DG-SiO<sub>2</sub>:  $l_{SPP}$  (red up-triangles) and  $l_{ci}$  (green circles). The  $l_{ci}$  is simulated by varying the charged-impurity density  $N_{ci}$ . The best match between  $l_{eq\_sim}$  (black solid line) and  $l_{avg\_exp}$  (blue diamonds) was found for  $N_{ci} = 7 \times 10^{10} \text{ cm}^{-2}$  (DG-SiC),  $1.8 \times 10^{11} \text{ cm}^{-2}$  (DG-SiO<sub>2</sub>). . . 126

# List of Tables

5.1 The characteristic SPP frequencies and the corresponding Fröhlich coupling constants for  $\text{SiO}_2$  and 4H-SiC. . . . . 126





# Chapter 1

## Introduction

### 1.1 Nanoscale science and technology: A primer

Nanoscale science and technology is forming and use of materials, structures, devices, and systems that have unique properties because of their small size as well as it includes the technologies that enable the control of materials at the nanoscale. National Nanotechnology Initiative (NNI) [1] defines Nanoscale science and technology as ‘the understanding and control of matter at dimensions of roughly 1 to 100 nm, where unique phenomena enable novel applications.’

#### What does it involve?

Current research in nanoscience and technology involves three main thrusts of research [2]:

- nanoscale science (or ‘nanoscience’ – the science of interaction and behavior at the nanoscale),
- nanomaterials development (the actual experimental development of nanoscale materials, including their use in device applications), and
- modeling (computer modeling of interactions and properties of nanoscale materials).

With nanoscience and technology, we start on the atomic scale and, controlling atomic/molecular placement and arrangement, we build up the technology into

unique devices, materials, and structures. This new type of formation requires new types of synthesis, requiring a new understanding of the formation of materials on the nanoscale. Furthermore, many materials have extremely unique properties when they are developed at a nanoscale. Many materials configure themselves in different atomic arrangements not seen in the bulk form of the same materials. Understanding the changes that these materials undergo as they are formed on a smaller scale is vital to developing the use of these materials in devices.

Nanoscale science and technology is a multidisciplinary field. Since, on the nanoscale, the laws of nature merge the laws of the very small (quantum mechanics) and the laws of the large (classical physics), physics is very important to understanding nanotechnology; since the material is vital to the function of device and structure, the science and engineering of materials are vital to developing nanotechnology. Additionally, specific applications require extensive knowledge from chemistry and biology as well.

## Characterization tools

Nanoscale science and technology has been propelled further by the characterization tools capable of ‘seeing at the nanoscale’ by enabling us to perceive further and deeper than we were able to before. Prominent amongst them are,

- **Electron microscopy:** The development of electron microscopy has made possible imaging materials at the nanoscale. For a typical low-voltage scanning electron microscope (SEM) with a beam energy of 5 kiloelectron volts (keV), the wavelength of the electron beam is around 0.0173 nm. For a 100 keV transmission electron microscope (TEM), the wavelength is even smaller, 0.0037 nm. For a 400 keV electron beam, the wavelength is 0.00028 nm. Of course, this theoretical limit and the actual resolution of the microscope are affected significantly by aberrations, defects, astigmatisms, and other practical considerations to reduce the resolution [3]. However, with certain configurations, these electron microscopes can even distinguish individual atoms. This enables us to discover and investigate nanomaterials and study how their atomic makeup impacts their properties.
- **Scanning probe microscopy (SPM):** It is not a ‘microscope’ in a conventional way [4]. In general, a scanning probe ‘feels’ the specimen and different aspects of it can be observed and understood by the acquired images. Scanning probe microscopes provide researchers with several new

## 1.1. Nanoscale science and technology: A primer

---

directions in which to study a material or manipulate it. For one, they provide three-dimensional information about the surface of the specimen instead of the two-dimensional information that electron microscopes provide. Samples viewed by some types of SPM do not require any special treatments that irreversibly alter the sample. Furthermore, it is easier to study macromolecules and biological samples with an SPM than it is with electron microscopes. Electron microscopes require a vacuum, while SPMs can typically be used in a standard room environment or even in liquid. Scanning probe microscopy does have its limits such as low throughput, probe tip wear, atmospheric disturbance. Despite this SPM based techniques are important for characterization and manipulation at nanoscale.

### Nanomaterials

Current nanoscale science and technology has a heavy focus on the discovery, characterization, and utilization of nanomaterials. Formation of such materials can be done either by breaking to smaller fractions from larger, known as ‘top-down’ technology; or the formation of materials from atomic or molecular structures known as ‘bottom-up’ technology. The materials that are being developed can be divided into two basic categories: organic (i.e., carbon based) and inorganic (i.e., not carbon based).

Carbon nanomaterials include,

- the buckyballs (all three spatial dimensions are confined to nanoscale – referred to as zero dimensional materials),
- carbon nanotubes (two spatial dimensions are confined to nanoscale – referred to as one dimensional materials) and very recently,
- graphene (one spatial dimension is confined to nanoscale – referred to as two dimensional materials).

The equivalent of these in inorganic materials are quantum dots (QDs), nanowires and ‘thin films’.

Considering that the topic of this thesis work is fabrication, identification and characterization of graphene for its use in prospective electronic applications, the next section traces current semiconductor technology’s path into nanoscale regime, and how this has led to the technology facing fundamental limitations. This to a greater extent has motivated pursuits for alternative technologies. The succeeding section reviews carbon materials in nanoelectronics; their relative

advantages to incumbent technology and the research efforts that have been made to establish carbon materials into mainstream electron device applications.

## 1.2 Nanoelectronics in retrospect

The semiconductor sector is one of the highest tempo fields of the business in the world, whether in communications, in the automobile industry, in relation to broadband and access technology, in mobile communications, healthcare equipments or memory products [5]. With its unparalleled technological successes semiconductor products have brought about a revolution in all strata of today's modern life. Advances powered by semiconductors give businesses and consumers new flexibility, freedom, and opportunity. Activities that once confined people to the home or office can now be performed at any time any place, almost anywhere in the world. The semiconductor industry is bringing new opportunities, socio-economic advance and new human development to nations and societies around the world [6].

For the past four decades Silicon (Si) has been the flag-bearer of this mega industry—almost synonymous with it. Si, found in ordinary sand, is the second most abundant element in the earth's crust after oxygen. With robust bandgap of 1.1 eV together with higher specific resistance resulting in far lower reverse current, Si surpassed other materials (especially Germanium, bandgap of 0.67 eV) as a material of choice to make transistors [?]. But the greatest asset of Si proved to be the fact that it readily sustains a protective oxide layer grown on its surface [7]. Frosh and Derick went on to demonstrate how this silicon dioxide ( $\text{SiO}_2$ ) coating could be used as a selective mask in the diffusion process [8] leading to its use for junction formation. The experience gained by fabrication of junctions via  $\text{SiO}_2$  masking in bipolar devices led D. Kahng and M. M. Atalla to report the first MOSFET (Metal-Oxide-Semiconductor Field-Effect-Transistor) on a Si substrate in 1960 [9]. The observation of junction passivation by Hoerni in the planar process in 1960 led to its use for improved junction characteristics [10]. Using  $\text{SiO}_2$  it was possible to construct planar semiconducting structures, each layer essentially separated by a thin oxide layer.  $\text{SiO}_2$  proved to be an extremely good insulator on which Al wiring could subsequently be adherently deposited [11]. This planar technology opened a new era in the semiconductor integration propelling the growth of Semiconductor industry by many-folds. Thus, Silicon's superior behavior at high temperature and great versatility of its oxide surface layer in manufacturing processes led to its current dominance of the semiconductor industry.

### 1.3. Carbon materials for prospective nanoelectronics

---

In 1965, Gordon Moore observed that the total number of devices on a chip would double every 12 months. He predicted that the trend would continue in the 1970's but would slow down in the 1980s, when the total number of devices would double every 24 months. Known widely as 'Moore's law', it became the guiding principle for the Semiconductor industry. These observations made the case for continued wafer and die size growth, defect density reduction and increased transistor density as manufacturing matured and technology scaled [12]. Throughout all this equally important has been the circuit cleverness, i.e. the reduction in number of devices and chip area to implement the given circuit or function. Hence, the driving force for continued integration complexity has been the reduction in cost per function for the chip [13]. The 1970's brought on the widespread use of dimensional scaling as the predominant means to increase device density and lower transistor cost via R. Dennard's scaling methodology [14].

Since then device scaling has been the engine driving the integrated circuit (IC) microelectronics revolution [15]. The critical elements in device scaling are the gate dielectric thickness, the channel length and the junction (and now) extension junction depth [16]. These dimensions have long reduced from their early 1970's values of 50–100 nm, 7.5  $\mu\text{m}$  and 1  $\mu\text{m}$  respectively to 1.1–1.6 nm, 45 nm and 25 nm (extension junction depth) for the high performance microprocessor (MPU) for the 100 nm technology generation as described in ITRS [17]. Si technology has already entered the regime of nanotechnology (sub 100 nm) by roadmap driven feature size reduction. But as the device features are pushed towards the deep sub-100 nm regime, the conventional scaling methods of the semiconductor industry face increasing technological and fundamental challenges [18].

## 1.3 Carbon materials for prospective nanoelectronics

The obstacles for Si circuitry has called for a need for development of alternative device technologies which are designed and interconnected in an appropriate architecture for nanoscale regime. This provides an opportunity to develop new concepts and/or new materials for the electronic applications. Though some paradigm shifting approaches involve development of spin-based devices, others continue to pursue traditional electron transport based devices, but involve replacement of the conducting channel in the FET with carbon nanomaterials

such as one-dimensional (1D) carbon nanotubes (CNT) or two-dimensional (2D) graphene layers, which have superior electrical properties [19]. As an added possibility the semiconducting CNTs, being a direct bandgap material, provide an ideal system to study optics and optoelectronics in one dimension and explore the possibility of basing both electronics and optoelectronic technologies on the same material.

From a device integration point of view metallic, particularly multiwalled, CNTs offer the possibility of use as high-performance interconnects in very-large-scale integrated systems [20], whereas semiconducting CNTs are useful candidates to be used as a basis of novel transistors. Indeed, the first CNT-FETs were reported in 1998 [21, 22]. The atomic and electronic structures of the CNT give it a number of unique advantages as a FET channel. First, its small diameter (1–2 nm) allows the gate to control the potential of the channel optimally. The strong coupling with the gate makes the CNT the ultimate ‘thin-body’ semiconductor system and allows the devices to be made shorter while avoiding the short-channel effects [23], which basically involve the loss of control of the device by the gate field. The fact that all bonds in the CNT are satisfied and the surface is smooth also has important implications. Scattering by surface states and roughness, which affects conventional FETs, especially at high gate voltage values, is absent. The key advantage is the low scattering in the CNT and the high mobility of the FET channel.

For the use in logic applications CNTFETs offer multiple advantages over Si MOSFETs because of their much lower capacitance of the order of  $\sim 10$  aF (for a  $d_{CNT}$  (diameter of CNT) = 1 nm,  $L$  (length of CNT) = 10 nm,  $t_{ox}$  (gate oxide thickness) = 5 nm device) and their somewhat lower operating voltage. Furthermore, the small size of the CNTs allow the fabrication of aligned arrays with high packing density. Also CNTFETs have lower switching energy per logic transition. The dynamic switching energy of a device is given by:  $1/2(C_{dev} + C_{wire})V^2$ , where  $C_{dev}$  and  $C_{wire}$  are the device and wiring capacitance contributions, respectively. To minimize the switching energy, minimum-sized devices, and interconnects should be used, as well as the minimum supply voltage. Then the CNT can have a considerable advantage, of up to a factor of six, because of its smaller intrinsic capacitance and size [24].

The fabrication and evaluation of CNT-based devices has advanced beyond single devices to include logic gates [25, 26, 27, 28] and, more recently more complex structures such as ring oscillators have been fabricated [29] using the energy efficient CMOS (complementary-MOS) architecture (by utilizing the ambipolar behavior of the undoped CNT).

In addition to be used as transistors, CNTFET devices can also be used as

### 1.3. Carbon materials for prospective nanoelectronics

---

a light emitter or a light detector. Choosing between these different modes of operation only requires changes in the electrical inputs. In order to fabricate LEDs, or other electroluminescent devices, one must generate and bring together significant populations of electrons and holes. The quasi-1D character of the CNT confines the two types of carriers, which are driven towards each other. Indeed, radiative recombination in an ambipolar CNTFET was reported in ref. [30]. Although the mechanism of that emission is similar to that of an LED, there is an important difference: the CNT is not doped so there is no clear p-n junction. As a result, the light does not originate from a fixed point along the CNT, but its origin can be translated by simply changing the gate voltage, which determines the local potential in a long CNT device [30]. Single CNT photoconductivity was reported for the first time in 2003 [31, 32]. The resonant excitation of a CNT generates an electric current and can be used as a nanosized photodetector, a photo switch, or as a spectroscopic tool. Alternatively, in the open-circuit configuration the device generates a photovoltage.

Opportunities also exist for integrating nanotube electronics with other chemical, mechanical, or biological systems. For example, nanotube electronic devices function perfectly well under biological conditions (i.e., salty water) and have dimensions comparable to typical biomolecules (e.g., DNA, whose width is approximately 2 nm). This makes them an excellent candidate for electrical sensing of individual biomolecules. There are also a host of other device geometries beyond the simple wire and FET structures that are under exploration, for example the p-n and p-n-p devices [33] and [34], nanotube/nanotube junctions [35, 36, 37], and electromechanical devices [38, 39].

However the major challenge faced by CNT based technology is the device manufacturability. Although a great deal of work has been done, the progress to date has been modest [40]. For example, in tube synthesis, the diameter of the tubes can be controlled, but not the chirality. As a result, the tubes are a mixture of metal and semiconductors. In chemical vapor deposition (CVD) growth of CNT, the general location for tube growth can be controlled by patterning the catalyst material, but the number of tubes and their orientation relative to the substrate are still not well defined. Furthermore, the high growth temperature (900 °C) for CVD tubes is incompatible with many other standard Si processes. The alternative approach, depositing tubes on a substrate after growth, avoids this high temperature issue but suffers from the chirality and positioning limitations. In addition to the patterning and device architecture related challenges CNT based devices possess unacceptably large contact resistance. To date, there are no reliable, rapid, and reproducible approaches to creating complex arrays of nanotube devices. This manufacturing issue is by far

the most significant impediment to using nanotubes in electronics applications.

However, the problems faced by CNT based electronics can be obviated while retaining their essential electronic properties by using the fundamental building block of both a graphite crystal and a CNT – the graphene layer.

## 1.4 Graphene

A two-dimensional (2D) allotrope of carbon is called graphene. It is made out of carbon atoms arranged on a honeycomb structure made out of hexagons. Graphene assumes an important role in understanding the electronic properties of all other carbon allotropes. As evidence, Fullerenes [41] are molecules where carbon atoms are arranged spherically, and hence, from the physical point of view, are zero-dimensional objects with discrete energy states. Fullerenes can be obtained from graphene with the introduction of pentagons (that create positive curvature defects), and hence, fullerenes can be thought as wrapped-up graphene. Carbon nanotubes [42, 43] are obtained by rolling graphene along a given direction and reconnecting the carbon bonds. Hence carbon nanotubes have only hexagons and can be thought of as one-dimensional (1D) objects. Graphite is a three dimensional (3D) allotrope of carbon.

Graphene layer is shown schematically in Figure 1.1(a). The atomic structure is characterized by two types of C–C bonds ( $\sigma$ ,  $\pi$ ) constructed from the four valence orbitals ( $2s$ ,  $2p_x$ ,  $2p_y$ ,  $2p_z$ ), where the  $z$ -direction is perpendicular to the sheet [44]. Three  $\sigma$ -bonds join a C atom to its three neighbors. They are quite strong, leading to optical-phonon frequencies much higher than observed in diamond. In addition, the C–C bonding is enhanced by a fourth bond associated with the overlap of  $p_z$  (or  $\pi$ ) orbitals. The electronic properties of graphene, graphite and carbon nanotubes are determined by the bonding  $\pi$ - and antibonding  $\pi^*$ -orbitals, that form wide electronic valence and conduction bands (Figure 1.1(b)).

Theoretical calculations show that the  $\pi$ -band overlap in graphite disappears as the layers are further separated over their equilibrium distance in graphite. This leads to decoupled graphene layers that can be described as a zero-gap semiconductor. The  $\pi$ -band electronic dispersion for graphene near the six corners of the 2D hexagonal Brillouin zone is found to be linear. Thus, ‘cones’ of carriers (holes and electrons) appear in the corners of a 2D Brillouin zone whose points touch at the Fermi energy, as shown in Figure 1.1(c). The linear electronic band dispersion leads to the description of carriers in graphene as ‘massless Dirac fermions’. The six points where the cones touch are referred to



## 1.5. Graphene and other 2D Semiconductor structures

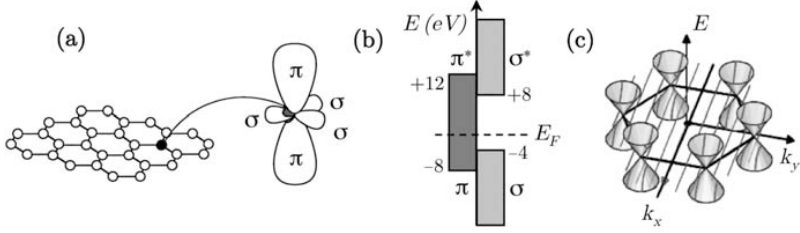


Figure 1.1: Illustration of the carbon valence orbitals. (a) The three inplane  $\sigma$  ( $s$ ,  $p_x$ ,  $p_y$ ) orbitals in graphene and the  $\pi$  ( $p_z$ ) orbital perpendicular to the sheet. The inplane  $\sigma$  and the  $\pi$  bonds in the carbon hexagonal network strongly connect the carbon atoms and are responsible for the large binding energy and the elastic properties of the graphene sheet. The  $\pi$  orbitals are perpendicular to the surface of the sheet. The corresponding bonding and the antibonding  $\sigma$  bands are separated by a large energy gap of  $\sim 12$  eV (b), while the bonding and antibonding  $\pi$  states lie in the vicinity of the Fermi level ( $E_F$ ). Consequently, the  $\sigma$  bonds are frequently neglected for the prediction of the electronic properties of graphene around the Fermi energy. Dirac cones located at the six corners of the 2D Brillouin zone are illustrated in (c) (adopted from [44]).

as the ‘Dirac’ points.

## 1.5 Graphene and other 2D Semiconductor structures

Graphene is a true two-dimensional electron system. There are, broadly speaking, four qualitative differences [45] between 2D graphene and 2D semiconductor systems found in Si inversion layers in MOSFETs, GaAs-AlGaAs heterostructures, quantum wells, etc.

1. First, 2D semiconductor systems typically have very large ( $>1$  eV) bandgaps so that 2D electrons and 2D holes must be studied using completely different electron-doped or hole-doped structures. By contrast, graphene is a gapless semiconductor with the nature of the carrier system changing at the Dirac point from electrons to holes (or vice versa) in a single structure. A direct corollary of this gapless (or small gap) nature of graphene, is of course, the ‘always metallic’ nature of 2D graphene, where the chemical

potential ('Fermi level') is always in the conduction or the valence band. By contrast, the 2D semiconductor becomes insulating below a threshold voltage, as the Fermi level enters the bandgap.

2. Graphene systems are chiral, whereas 2D semiconductors are non-chiral. Chirality of graphene leads to some important consequences for transport behavior. (For example,  $2k_F$  -backscattering is suppressed in MLG at low temperature.)
3. Monolayer graphene dispersion is linear, whereas 2D semiconductors have quadratic energy dispersion. This leads to substantial quantitative differences in the transport properties of the two systems.
4. Finally, the carrier confinement in 2D graphene is ideally two-dimensional, since the graphene layer is precisely one atomic monolayer thick. For 2D semiconductor structures, the quantum dynamics is two dimensional by virtue of confinement induced by an external electric field, and as such, 2D semiconductors are quasi-2D systems, and always have an average width or thickness  $\langle t \rangle$  ( $\approx 5$  nm to 50 nm) in the third direction with  $\langle t \rangle \leq \lambda_F$ , where  $\lambda_F$  is the 2D Fermi wavelength (or equivalently the carrier de Broglie wavelength). The condition  $\langle t \rangle < \lambda_F$  defines a 2D electron system.

In particular, for a system to be defined as 2D,  $\lambda_F = 2\pi/k_F > t$  where  $\lambda_F$  is the Fermi wavelength (i.e. the operational quantum wavelength of the system). For graphene, we have  $\lambda_F \approx (35/\sqrt{n'})$  nm, where  $n' = n/(10^{12} \text{ cm}^{-2})$ , and since  $t \approx 0.1$  nm to 0.2 nm (the monolayer atomic thickness), the condition  $\lambda_F \gg t$  is always satisfied, even for unphysically large  $n=10^{14} \text{ cm}^{-2}$ . The classic technique to verify the 2D nature of a particular system is to show that the orbital electronic dynamics is sensitive only to a magnetic field perpendicular to the 2D plane (or more precisely, that the system response depends only on the perpendicular component  $B \cos \vartheta$  of an applied magnetic field ( $B$ ) at angle  $\vartheta$  to the  $z$ -direction) of confinement. Therefore, the observation of magnetoresistance oscillations (Shubnikov-de Hass effect) depending only on  $B \cos \vartheta$ , proves the 2D nature, or if the cyclotron resonance properties depend only on  $B \cos \vartheta$ , then the 2D nature is established. Both of these are true in graphene. The most definitive evidence for 2D nature, however, is the observation of the quantum Hall effect, which is a quintessentially 2D phenomenon. Any system manifesting an unambiguous quantized Hall plateau is 2D in nature, and therefore the observation of the quantum Hall effect in graphene in 2005 by Novoselov et al. [46, 47] and Zhang et al. is an absolute evidence of its 2D nature (Figure 1.2).

## 1.5. Graphene and other 2D Semiconductor structures

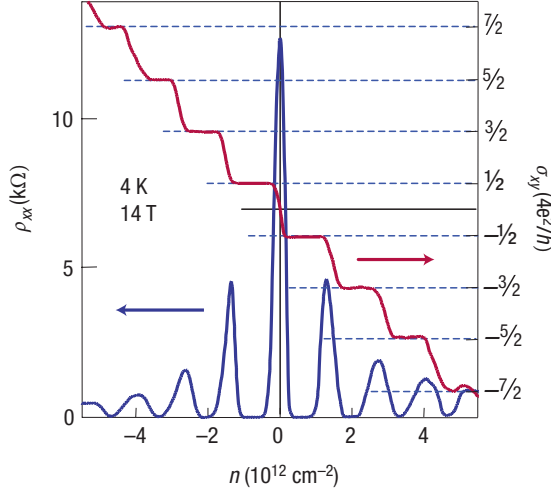


Figure 1.2: Quantum Hall effect in graphene. The plateau in  $\sigma_{xy}$  at half integers of  $4e^2/h$  is a hallmark of massless Dirac fermions.  $\rho_{xx}$  vanishes for the same carrier concentrations.

In fact, the quantum Hall effect in graphene persists to room temperature [48], indicating that graphene remains a strict 2D electronic material even at room temperature.

As a final note, from a structural viewpoint the existence of finite 2D flakes of graphene with crystalline order at finite temperature does not in any way violate the Hohenberg-Mermin-Wagner-Coleman theorem, which rules out the breaking of a continuous symmetry in two dimensions. This is because the theorem only asserts a slow power law decay of the crystalline (i.e. positional order) correlation with distance, and hence, very large flat 2D crystalline flakes of graphene (or for that matter, of any material) are manifestly allowed by this theorem. Hence, it is not forbidden to have finite 2D crystals with quasi-long-range positional order at finite temperatures, which is what we have in 2D graphene flakes [45].

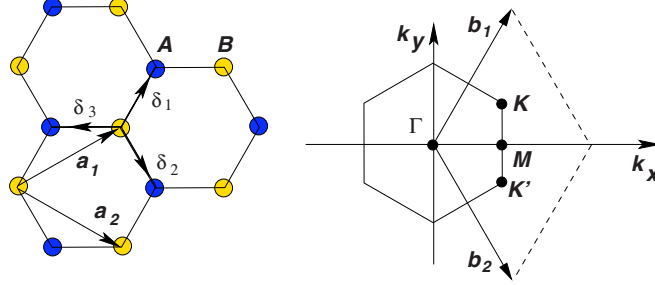


Figure 1.3: Honeycomb lattice and the Brillouin zone in graphene. (a) the lattice structure in graphene is made of two interpenetrating triangular lattices ( $a_1$  and  $a_2$  are the lattice unit vectors and  $\delta_i$ ,  $i=1, 2, 3$  are the nearest-neighbor vectors), (b) corresponding Brillouin zone. The Dirac cones are located at the K and K' points (adopted from [49]).

## 1.6 Bandstructure of graphene and elementary electronic properties [49]

Graphene honeycomb lattice along with its Brillouin zone is as shown in Figure 1.3.

The structure can be seen as a triangular lattice with a basis of two atoms per unit cell. The lattice vectors can be written as,

$$a_1 = \frac{a}{2}(3, \sqrt{3}) \quad a_2 = \frac{a}{2}(3, -\sqrt{3}) \quad (1.1)$$

where  $a \approx 1.42 \text{ \AA}$  is the carbon-carbon distance. The reciprocal-lattice vectors are given by,

$$b_1 = \frac{2\pi}{3a}(1, \sqrt{3}) \quad b_2 = \frac{2\pi}{3a}(1, -\sqrt{3}) \quad (1.2)$$

Of particular importance for the physics of graphene are the two points K and K' at the corners of the graphene Brillouin zone (BZ). These are named Dirac points. Their positions in momentum space are given by,

$$K = \left( \frac{2\pi}{3a}, \frac{2\pi}{3\sqrt{3}a} \right) \quad K' = \left( \frac{2\pi}{3a}, -\frac{2\pi}{3\sqrt{3}a} \right) \quad (1.3)$$

The three nearest-neighbor vectors in real space are given by,

## 1.6. Bandstructure of graphene and elementary electronic properties

$$\delta_1 = \frac{a}{2} (1, \sqrt{3}), \quad \delta_2 = \frac{a}{2} (1, -\sqrt{3}), \quad \delta_3 = -a (1, 0) \quad (1.4)$$

while the six second-nearest neighbors are located at,

$$\delta'_1 = \pm a_1 \quad \delta'_2 = \pm a_1 \quad \delta'_3 = \pm(a_2 - a_1)$$

The tight-binding Hamiltonian for electrons in graphene considering that electrons can hop to both nearest-and next-nearest-neighbor atoms has the form (using units such that  $\hbar=1$ )

$$H = -t \sum (a_{\sigma,i}^* b_{\sigma,j} + h.c) - t' \sum (a_{\sigma,i}^* a_{\sigma,j} + b_{\sigma,i}^* b_{\sigma,j} + h.c) \quad (1.5)$$

where  $a_{i,\sigma}$  ( $a_{i,\sigma}^*$ ) annihilates (creates) an electron with spin  $\sigma$  ( $\sigma=\text{up, down}$ ) on site  $R_i$  on sublattice A (an equivalent definition is used for sublattice B),  $t$  ( $\approx 2.8$  eV) is the nearest-neighbor hopping energy (hopping between different sublattices), and  $t'$  is the next nearest-neighbor hopping energy (hopping in the same sublattice). The energy bands derived from this Hamiltonian have the form:

$$E_{\pm}(k) = \pm t \sqrt{3 + f(k)} - t' f(k) \quad (1.6)$$

$$f(k) = 2 \cos(\sqrt{3} k_y a) + 4 \cos\left(\frac{\sqrt{3}}{2} k_y a\right) \cos\left(\frac{3}{2} k_x a\right)$$

where the plus sign applies to the upper ( $\pi$ ) and the minus sign the lower ( $\pi^*$ ) band. It is clear from Equation 1.6 that the spectrum is symmetric around zero energy if  $t'=0$ . For finite values of  $t'$  the electron-hole symmetry is broken and the  $\pi$  and  $\pi^*$  bands become asymmetric. Figure 1.4, shows the full band structure of graphene with both  $t$  and  $t'$ . The band structure close to one of the Dirac points (at the K or K' point in the BZ) can be obtained by expanding the full band structure, Equation 1.6, close to the K (or K') vector, Equation 1.3, as  $k = K + q$ , with  $|q| \ll K$ : [50],

$$E_{\pm}(q) \approx \pm v_F |q| + \mathcal{O}\left(\left(\frac{q}{K}\right)^2\right) \quad (1.7)$$

where  $q$  is the momentum measured relatively to the Dirac points and  $v_F$  is the Fermi velocity, given by  $v_F = 3ta/2$ , with a value  $v_F \approx 1 \times 10^6$  m/s.

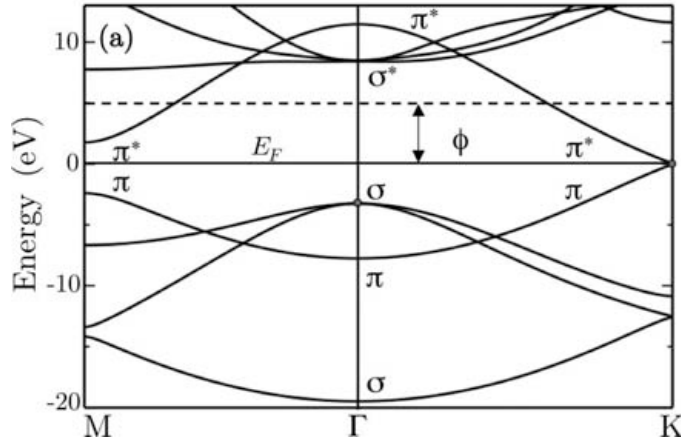


Figure 1.4: Electronic band structure of graphene from ab-initio calculations. The bonding  $\sigma$  and the antibonding  $\sigma^*$  bands are separated by a large energy gap. The bonding  $\pi$  (highest valence band) and the antibonding  $\pi^*$  (lowest conduction band) bands touch at the K(K') points of the Brillouin zone. The Fermi energy ( $E_F$ ) is set to zero and  $\phi$  indicates the work function (by the dashed horizontal line). Above the vacuum level  $\phi$ , the states of the continuum are difficult to describe and merge with the  $\sigma^*$  bands. The 2D hexagonal Brillouin zone is illustrated with the high-symmetry points  $\Gamma$ , M, K and K' (adopted from [44]).

## 1.6. Bandstructure of graphene and elementary electronic properties

---

### 1.6.1 Cyclotron mass

The energy dispersion expressed by Equation 1.7 resembles the energy of ultrarelativistic particles; these particles are quantum mechanically described by the massless Dirac equation. An immediate consequence of this massless Dirac-like dispersion is a cyclotron mass that depends on the electronic density as its square root [46, 47]. The cyclotron mass is defined, within the semiclassical approximation [51], as

$$m^* = \frac{1}{2\pi} \left[ \frac{\partial A(E)}{\partial E} \right]_{E=E_F} \quad (1.8)$$

with  $A(E)$  the area in  $k$ -space enclosed by the orbit and given by:

$$A(E) = \pi q(E)^2 = \pi \frac{E^2}{\nu_F^2} \quad (1.9)$$

Using Equation 1.9 in Equation 1.8 one obtains

$$m^* = \frac{E_F}{\nu_F^2} = \frac{k_F}{\nu_F} \quad (1.10)$$

The electronic density,  $n$ , is related to the Fermi momentum,  $k_F$ , as  $k_F^2/\pi = n$  (with contributions from the two Dirac points  $K$  and  $K'$  and spin included) which leads to:

$$m^* = \frac{\sqrt{\pi}}{\nu_F} \sqrt{n} \quad (1.11)$$

Fitting Equation 1.11 to the experimental data provides an estimation for the Fermi velocity and the hopping parameter as  $\nu_F = 10^6 \text{ ms}^{-1}$  and  $t \approx 3 \text{ eV}$ , respectively. Experimental observation of the  $\sqrt{n}$  dependence on the cyclotron mass provides evidence for the existence of massless Dirac quasiparticles in graphene [46, 47, 52, 53].

### 1.6.2 Density of states

For  $t' = 0$ , it is possible to derive an analytical expression for the density of states per unit cell, which has the form [54]:

$$D(E) = \frac{4}{\pi^2} \frac{|E|}{t^2} \frac{1}{\sqrt{Z_0}} F\left(\frac{\pi}{2}, \sqrt{\frac{Z_1}{Z_0}}\right) \quad (1.12)$$

$$Z_0 = \begin{cases} \left(1 + \left|\frac{E}{t}\right|\right)^2 - \frac{\left(\left(\frac{E}{t}\right)^2 - 1\right)^2}{4} & ; \quad -t \leq E \leq t \\ 4 \left|\frac{E}{t}\right| & ; \quad -3t \leq E \leq -t \vee t \leq E \leq 3t \end{cases}$$

$$Z_1 = \begin{cases} 4 \left|\frac{E}{t}\right| & ; \quad -t \leq E \leq t \\ \left(1 + \left|\frac{E}{t}\right|\right)^2 - \frac{\left(\left(\frac{E}{t}\right)^2 - 1\right)^2}{4} & ; \quad -3t \leq E \leq -t \vee t \leq E \leq 3t \end{cases}$$

where  $F(\pi/2, x)$  is the complete elliptic integral of the first kind. Close to the Dirac point, the dispersion is approximated by Equation 1.7 and the density of states per unit cell is given by (with a degeneracy of 4 included):

$$D(E) = \frac{2A_c}{\pi} \frac{\left|\frac{E}{t}\right|}{\nu_F^2} \quad (1.13)$$

where  $A_c$  is the unit cell area given by  $A_c = 3\sqrt{3}a^2/2$ .

## 1.7 Graphene for electronics applications: Opportunities and challenges

Graphene has been adopted as a material of choice by researchers involved in many fields. The first and most discussed is the electronic spectrum. Massless electrons along with very high mobility in graphene have given access to unusual quantum hall effect. And many other phenomena like Klein tunneling, zitterbewegung, the Schwinger production [55] and Casimir-like interactions between adsorbates on graphene [56] have been predicted. However, simultaneous observation of high mobility, sensitivity to field effect and ease of contacting made graphene an appealing candidate for field-effect transistor devices. A lot of progress has been made in that direction. Manufacturability of graphene transistor operating at 100 GHz has been demonstrated on wafer-scale [57]. Having said that, there remains a few issues, like (i) there is no consensus about the scattering mechanism that currently limits the mobility in graphene devices, (ii) having no electronic gap, it forbids/limits the possibility of graphene in logic applications. There have been several strategies implemented to open a gap. Amongst them (i) the inclusion of  $sp^3$  hydrocarbon defects in the  $sp^2$  lattice [58, 59], (ii) the distortion of the carbon atom lattice under uniaxial strain



## 1.8. Motivation and scope of thesis work

---

[60, 61, 62], (iii) electrostatically-gated bilayer graphene can be mentioned [63]. Influence of the SiC substrate on the epitaxial graphene on Si face has also been shown to induce substantial band gap ( $\sim 260$  meV) [64, 65]. Moreover, a bandgap can also be induced in semi metallic graphene by a direct consequence of the lateral confinement of the 2DEG in ribbon-shaped graphene [66, 67, 68, 69, 70]. However, this points to extremely challenging need to perform atomically precise tailoring of graphene over long distances for advanced graphene electronic architectures.

Moreover, chemically stable, robust and foldable graphene sheets possess enough optical transparency to be considered as transparent conductors in applications as coatings for solar cells, liquid crystal displays etc. for the replacement of indium tin oxide [71].

In addition to that, there has been demonstration of nonvolatile memories based on structures fabricated in graphene as voltage programmable bistable switches for memory elements [72]. Similarly, two terminal devices based on graphene nanocables have been shown to possess reversible resistance switching [73]. Additionally, hybrid nonvolatile memory device using graphene and ferroelectric thin film have been demonstrated based on resistance switching due to the electric dipole induced doping in graphene by the ferroelectric thin film [74]. Apart from that use of graphene in sensing application is foreseen based on the demonstration of sensing capability down to detecting individual gas molecules [75].

## 1.8 Motivation and scope of thesis work

As ongoing efforts to incorporate graphene into electronic applications, attempts are already being made to gain consistent control over electronic properties in graphene down to nanometer scale so as to explore its possibility as a complementary material to Si for prospective nanoelectronics. Notable amongst these include intentional control of the density and character of its charge carriers by doping [76, 77], and confining charge carriers to nanometer constrictions [78, 79]. Classically, most experiments probe the global response of graphene devices thus yielding properties averaged over the whole device. As a consequence, local properties and their distributions within the sample are inaccessible with standard transport measurements. In lower dimensional electronic systems (LDES), like graphene, the local phenomenon/effects might have much stronger impact than previously believed. Hence, naturally, developing techniques to analyze and/or control the local effects in graphene has attracted wide interests. Con-

sequently, such local probing techniques have helped gain significant insights into various aspects of functioning graphene devices. Notably, Scanning probe microscopy (SPM) based measurements have provided the most direct probe of local electronic properties. For example, Scanning Photocurrent Microscopy [80, 81] has been used to probe the ‘electrostatic potential landscape’ of graphene in view of analyzing the local changes in the electronic structure of the graphene sheets introduced by their interaction with deposited metal contacts and by local symmetry breaking/disorder at the sheet edges. On the other hand Raman microscopy has been used to probe mesoscopic inhomogeneity in the doping [82, 83], due, possibly, to the presence of charged impurities. Additionally, Raman microscopy has also been used to measure the temperature distribution [84] in a biased graphene flake, in turn giving insights into energy dissipation patterns in graphene field-effect transistors. Formation of sub-micron (resolution limited) electron and hole charge puddles near Dirac point in graphene, has been demonstrated by Martin et. al. [85] using Scanning Single Electron Transistor microscopy where they gauged the intrinsic size of the puddles to be  $\sim 30$  nm.

Atomic Force Microscope based scanning microscopy techniques have also been significantly used to get better insights in graphene electronic properties. For example, high-resolution scanning tunneling microscopy (STM) [86] experiments have directly imaged charge puddles of  $\sim 10$  nm in size and suggested they originate from individual charged impurities underneath graphene. Scanning Gate Microscopy (SGM) [87, 88] has revealed mesoscopic domains of electron and hole doped regions with substantial spatial fluctuations (on the order of  $10^{12}/\text{cm}^2$ ) in the carrier density due to extrinsic local doping coming from metal contacts, edges of graphene, structural defects and resist residues. The influence of electric field effect on the local work function in graphene was probed by acquiring surface potential maps with Scanning Kelvin Probe Microscopy (SKPM) [89].

In the wake of such proven local inhomogeneity in electrical properties of graphene the work presented in this thesis focuses on local evaluation of electrostatic and transport properties in substrate-supported graphene by the use of scanning probe microscopy based original methods with nanometer scale lateral resolution. The manuscript has been arranged in the following way:

- Chapter 2 is aimed at giving details on the characterization techniques and sample preparation methods used in this study. In particular, the basic operation of scanning tunneling microscope and atomic force microscope is introduced and various variants of characterization techniques

## 1.8. Motivation and scope of thesis work

---

based on atomic force microscopy aimed at applications to nanoscale electro-structural characterization are described. For example a description about Scanning Capacitance Spectroscopy (SCapS), Scanning Current Spectroscopy (ScurS), Torsion-Resonance Conductive Atomic Force Microscopy (TR-CAFM), TappingMode Atomic Force Microscopy (t-AFM) is included along with their possible applications to graphene characterization. Additionally, preparation of graphene samples by the methods of mechanical exfoliation of highly oriented pyrolytic graphite and high temperature annealing of hexagonal SiC substrates is discussed. Moreover, an important aspect of sample preparation is the determination of number of graphene layer. Therefore, an extensive study about the quantification of graphene layers is included. For exfoliated graphene, such quantification was carried out by cross comparison of optical contrast microscopy, morphological scans with t-AFM and Raman spectroscopy, whereas a combination of TR-CAFM scans, Raman spectroscopy, transmission electron microscopy and morphological scans on selectively etched regions in graphitized SiC enabled to locate epitaxial graphene layers.

- Chapter 3 focuses on evaluation of electrostatic properties, quantum capacitance and density of states, in graphene on insulating and semi-insulating substrates by locally measuring capacitance with SCapS. The ingenuity of this method, i. e. the ease in evaluation of electrostatic properties simply by comparing the capacitance variations on graphene and on supporting substrate, makes its application easier to graphene supported by other insulating and/or semi-insulating substrates without any need for special sample preparation. Thus, as an extension, the effect of dielectric environment of graphene on its electrostatic properties is discussed by comparison of graphene on silicon dioxide ( $\text{SiO}_2$ ) and graphene on Strontium Titanate (STO). Furthermore, such local capacitance measurements allow to evaluate the screening length in graphene, which then is shown to be equivalent to the local electron mean free path in graphene.
- Chapter 4 describes defect formation in graphene by controlled amount of irradiation with high energy ions. Comprehensive Raman spectroscopic investigation at micrometer scale is carried out to understand the evolution of defects with increasing irradiation dose and the study is supported by high-resolution t-AFM investigation. Furthermore, evolution of electronic properties, quantum capacitance, local electron mean free path, local mobility and Fermi velocity with increasing irradiation fluence is carried out by local capacitance measurements.

- Chapter 5 is intended to address the role of graphene/substrate interface on the electrostatic and transport properties of 2DEG in graphene. In particular, the studies carried out with nanoscale current transport across graphene/SiC to understand the local work function variations due to electrically active buffer layer is described. Above and beyond, the effect of interface related scattering mechanisms are discussed by evaluation and comparison of local electrostatic and transport properties on most relevant substrates in view of electronic applications (SiO<sub>2</sub> and SiC).
- Chapter 6 summarizes most important conclusions.

# References

- [1] <http://www.nano.gov/>
- [2] F. Allhoff, P. Lin, and D. Moore, What is nanotechnology and why does it matter : from science to ethics, (Wiley-Blackwell), (2010)
- [3] Z. L. Wang and Z.C. Kang, Functional and Smart Materials: Structural Evolution and Structure Analysis, 1<sup>st</sup> edn. (New York: Plenum Press), (1998)
- [4] G. Binnig, H. Rohrer, Ch. Gerber, E. Weibel, Phys. Rev. Lett. 49, 57 (1982)
- [5] Editor: Infineon Technologies AG, München, Semiconductors Technical information, technologies and characteristic data, 2nd Ed., Publicis Corporate Publishing, Erlangen (2004)
- [6] Semiconductor Industry Association, [http://www.sia-online.org/iss\\_economy.cfm](http://www.sia-online.org/iss_economy.cfm)
- [7] Riordan and Hoddeson, Crystal Fire, 221-222, (1997)
- [8] C. J. Frosch and L. Derick, J. of the Electrochem Soc., 104, 547, (1957). See also M.Riordan and L. Hoddeson, Physics Today, 42, (December 1997)
- [9] D. Kahng and M. M. Atalla, DRC, Pittsburg (1960); U.S patent No. 3,102,230 (1963)
- [10] J. A. Hoerni, Fairchild Technical Article and Paper Series No.TP-14(1961), paper first presented at the 1960 IRE International Electron Devices meeting, Washington D.C., October 27-29, (1960)

- [11] C. M. Osburn and H. R. Huff, <http://www.electrochem.org/dl/ma/201/pdfs/0366.pdf>.
- [12] S. Rusu et. al., Proc. of the 15th international conference on VLSI design, (2002).
- [13] D. K. Ferry et al., Semiconductor device scaling: Physics, Transport and the role of Nanowires, <http://www.eecs.uc.edu/~mcahay/Nano2006/Invited/Ferry.pdf>.
- [14] R. H. Dennard et al., IEEE J. Solid-State Circuits, vol. SC-9, 256, (1974)
- [15] G. E. Moore, SPIE 2438, 2-17, (1995)
- [16] H. R. Huff et al., ECS PV 2001-09, 263, (2001)
- [17] International Technology Roadmap for Semiconductors (ITRS), (<http://www.itrs.net>), (2001)
- [18] J. D. Meindl, IEEE IEDM Tech. Dig. 8 (1983)
- [19] P. Avouris, Phys. World 20, 40 (2007)
- [20] A. Naeemi, R. Sarvati, & J. D. Meindl, IEDM Digest, 699 (2004)
- [21] S. J. Tans, A. R. M. Verscheuren, & C. Dekker, Nature 393, 49 (1998)
- [22] R. Martel, T. Schmidt, H. R. Shea, T. Hertel, & P. Avouris, Appl. Phys. Lett. 73, 2447 (1998)
- [23] S. M. Sze, Physics of Semiconductor Devices. (Wiley, New York, 1981)
- [24] P. M. Solomon, in Future Trends in Microelectronics: Up the Nano Creek (eds S. Luryi, J. M. Xu, & A. Zaslavsky) 212 (Wiley, New York) (2007)
- [25] A. Javey, et al. Nature Mater. 1, 241 (2002)
- [26] A. Bachtold, P. Hadley, T. Nakanishi, & C. Dekker, Science 294, 1317 (2001)
- [27] V. Derycke, R. Martel, J. Appenzeller, & P. Avouris, Nano Lett. 1, 453 (2001)
- [28] X. Liu, C. Lee, C. Zhou, & J. Han, Appl. Phys. Lett. 79, 3329 (2001)

## REFERENCES

---

- [29] Z. Chen, et al. *Science* 311, 1735 (2006)
- [30] J. A. Misewich, et al. *Science* 300, 783 (2003)
- [31] M. Freitag, et al. *Nano Lett.* 3, 1067 (2003)
- [32] X. Qiu, M. Freitag, V. Perebeinos, & P. Avouris, *Nano Lett.* 5, 749 (2005)
- [33] C. Zhou, J. Kong, E. Yenilmez, and H. Dai, *Science* 290, 1552, (2000)
- [34] J. Kong, J. Cao, and H. Dai, *Appl. Phys. Lett.* 80, 73, (2002)
- [35] Z. Yao, H. W. C. Postma, L. Balents, and C. Dekker, *Nature* 402, 273, (1999)
- [36] J. Lefebvre, R. D. Antonov, M. Radosavljevic, J. F. Lynch, M. Llaguno, and A. T. Johnson, *Carbon* 38, 1745, (2000)
- [37] M. S. Fuhrer, J. Nygård, L. Shih, M. Forero, Y.-G. Yoon, M. S. C. Mazzoni, H. J. Choi, J. Ihm, S. G. Louie, Z. A. Zettl, and P. L. McEuen, *Science* 288, 494, (2000)
- [38] T. Rueckes, K. Kim, E. Joselevich, G. Y. Tseng, C. L. Cheung, and C. M. Lieber, *Science*, 289, 94, (2000)
- [39] T. W. Tomblor, Z. Chongwu, L. Alxseyev, K. Jing, D. Hongjie, L. Lei, C. S. Jayanthi, T. Meijie, and W. Shi-Yu, *Nature* 405, 769, (2000)
- [40] P. L. McEuen, M. S. Fuhrer, and H. Park, *IEEE Trans. on Nanotech.* 1, 78 (2002)
- [41] W. Andreoni, *The Physics of Fullerene-Based and Fullerene-Related Materials* (Springer, Berlin), (2000)
- [42] R. Saito, G. Dresselhaus, and M. S. Dresselhaus, *Physical Properties of Carbon Nanotubes*, (Imperial College Press, London) (1998)
- [43] J.-C. Charlier, X. Blase, and S. Roche, *Rev. Mod. Phys.* 79, 677 (2007)
- [44] A. Jorio, G. Dresselhaus, M. S. Dresselhaus (Eds.): *Carbon Nanotubes*, *Topics Appl. Physics* 111, 673, (Springer-Verlag Berlin Heidelberg) (2008)
- [45] S. Das Sarma, S. Adam, E. H. Hwang, and E. Rossi, arXiv:1003.4731v1 (2010)

- [46] K. S. Novoselov, A. K. Geim, S. V. Morozov, D. Jiang, Y. Zhang, M. I. Katsnelson, I. V. Grigorieva, S. V. Dubonos, and A. A. Firsov, *Nature* 438, 197 (2005)
- [47] Y. Zhang, Y.-W. Tan, H. L. Stormer, and P. Kim, *Nature* 438, 201 (2005)
- [48] K. S. Novoselov, Z. Jiang, Y. Zhang, S. V. Morozov, H. L. Stormer, U. Zeitler, J. C. Maan, G. S. Boebinger, P. Kim, and A. K. Geim, *Science* 315 (5817), 1379 (2007)
- [49] A. H. Castro Neto, F. Guinea, N. M. R. Peres, K. S. Novoselov and A. K. Geim, *Rev. of Mod. Phys.* 81, 109 (2009)
- [50] P. R. Wallace, *Phys. Rev.* 71, 622 (1947)
- [51] N. W. Ashcroft, and N. D. Mermin, *Solid State Physics* (Saunders College, Philadelphia) (1976)
- [52] R. S. Deacon, K.-C. Chuang, R. J. Nicholas, K. S. Novoselov, and A. K. Geim, *Phys. Rev. B* 76, 081406 (R) (2007)
- [53] Z. Jiang, E. A. Henriksen, L. C. Tung, Y.-J. Wang, M. E. Schwartz, M. Y. Han, P. Kim, and H. L. Stormer, *Phys. Rev. Lett.* 98, 197403 (2007)
- [54] J. P. Hobson, and W. A. Nierenberg, *Phys. Rev.* 89, 662 (1953)
- [55] D. Allor, T. D. Chen, D. A. McGady, *Phys. Rev. D* 78, 096009 (2008)
- [56] A. Shytov, D. Abanin, L. Levitov, <http://arxiv.org/abs/0812.4970> (2008)
- [57] Y.-M. Lin, C. Dimitrakopoulos, K. A. Jenkins, D. B. Farmer, H.-Y. Chiu, A. Grill, Ph. Avouris, *Science* 327, 662, (2010)
- [58] S. Ryu, M. Y. Han, J. Maultzsch, T. F. Heinz, P. Kim, M. L. Steigerwald, et al., *Nano Lett.* 8, 4597 (2008)
- [59] D. C. Elias, R. R. Nair, T. M. G. Mohiuddin, S. V. Morozov, P. Blake, M. P. Halsall, et al., *Science* 323, 610 (2009)
- [60] Z. H. Ni, T. Yu, Y. H. Lu, Y. Y. Wang, Y. P. Feng, Z. X. Shen, *ACS Nano* 2, 2301 (2008)
- [61] M. L. Teague, A. P. Lai, J. Velasco, C. R. Hughes, A. D. Beyer, M. W. Bockrath, et al., *Nano Lett.* 9, 2542 (2009)



REFERENCES

---

- [62] F. Guinea, B. Horovitz, P. Le Doussal, Solid State Commun. 148, 1140 (2009)
- [63] J. B. Oostinga, H. B. Heersche, X. Liu, A. F. Morpurgo, L. M. K. Vandersypen, Nat. Mater. 7, 151 (2008)
- [64] S. Y. Zhou, G. H. Gweon, A. V. Fedorov, P. N. First, W. A. De Heer, D. H. Lee, et al., Nat Mater. 6, 770 (2007)
- [65] S. Y. Zhou, G. H. Gweon, A. V. Fedorov, P. N. First, W. A. De Heer, D. H. Lee, et al., Nat Mater. 6, 916 (2007)
- [66] T. Ando, Physics of graphene – zero-mode anomalies and roles of symmetry. Prog. Theor. Phys. 176(Suppl.), 203 (2008)
- [67] M. Fujita, K. Wakabayashi, K. Nakada, K. Kusakabe, J. Phys. Soc. Jpn. 65, 1920 (1996)
- [68] K. Nakada, M. Fujita, G. Dresselhaus, M. S. Dresselhaus, Phys. Rev. B 54, 17954 (1996)
- [69] K. Wakabayashi, T. Aoki, Int. J. Mod. Phys. B 16, 4897 (2002)
- [70] M. Yamamoto, K. Wakabayashi, Appl. Phys. Lett. 95, 082109 (2009)
- [71] A. K. Geim, Science 324, 1530 (2009)
- [72] Y. Li, A. Sinitskii, J. M. Tour, Nat. Mater. 7, 966 (2008)
- [73] B. Standley et al., Nano Lett. 8, 3345 (2008)
- [74] Y. Zheng et al., Appl. Phys. Lett. 94, 163505 (2009)
- [75] F. Schedin et al., Nat. Mater. 6, 652 (2007)
- [76] X. Wang, X. Li, L. Zhang, Y. Yoon, P. K. Weber, H. Wang, and H. Dai, Science 324, 768 (2009)
- [77] I. Gierz, C. Riedl, U. Starke, C. R. Ast, and K. Kern, Nano Lett. 8, 4603 (2008)
- [78] M. Y. Han, B. Ozyilmaz, Y. Zhang, and P. Kim, Phys. Rev. Lett. 98, 206805 (2007)
- [79] Z. Chen, Y.-M. Lin, M. J. Rooks, and P. Avouris, Physica E 40, 228 (2007)

- [80] E. J. H. Lee, K. Balusubramanian, R. T. Weitz, M. Burghard, and K. Kern, *Nat. Nanotechnol.* 3, 486 (2008)
- [81] T. Mueller, F. Xia, M. Freitag, J. Tsang, and P. Avouris, *Phys. Rev. B* 79, 245430 (2009)
- [82] C. Casiraghi, S. Pisana, K. S. Novoselov, A. K. Geim, and A. C. Ferrari, *Appl. Phys. Lett.* 91, 233108 (2007)
- [83] A. Das, S. Pisana, S. Piscanec, B. Chakraborty, S. K. Saha, U. V. Waghmare, R. Wang, H. R. Krishnamurthy, A. K. Geim, A. C. Ferrari, and A. K. Sood, *Nat. Nanotechnol.* 3, 210 (2008)
- [84] M. Freitag, M. Steiner, Y. Martin, V. Perebeinos, Z. Chen, J. C. Tsang, and P. Avouris, *Nano Lett.* 9, 1883 (2009)
- [85] J. Martin, N. Akerman, G. Ulbricht, T. Lohmann, J. Smet, K. V. Klitzing, and A. Yacoby, *Nat. Phys.* 4, 144 (2008)
- [86] Y. Zhang, V. W. Brar, C. Girit, A. Zett, A., M. F. Crommie, *Nature Phys.* 5, 722 (2009)
- [87] R. Jalilian, L. A. Jauregui, G. Lopez, J. Tian, C. Roecker, M. M. Yazdanpanah, R. W. Cohn, I. Jovanovic, Y. P. Chen, <http://arxiv.org/abs/1003.5404> (2010)
- [88] M. R. Connolly, K. L. Chiou, C. G. Smith, D. Anderson, G. A. C. Jones, A. Lombardo, A. Fasoli, and A. C. Ferrari, *Appl. Phys. Lett.* 96, 113501 (2010)
- [89] Y.-J. Yu, Y. Zhao, S. Ryu, L. E. Brus, K. S. Kim, and P. Kim, *Nano Lett.* 9, 3430 (2009)

## Chapter 2

# Experimental set-up

### 2.1 Introduction

Scanning Probe Microscopy (SPM) based characterization tools, which allow investigation and manipulation of surfaces down to the atomic scale are important catalyst for the growth of nanoscale science and technology. A prominent example of that is the Scanning Tunneling Microscope (STM), which was introduced in 1981. STM is the first instrument capable of directly obtaining three-dimensional images of solid surfaces with atomic resolution [1]. Based on the design of STM later on in 1985 the Atomic Force Microscope (AFM) was introduced [2, 3]. The AFM is capable of measuring ultrasmall forces present between the AFM tip apex and the sample surface. Owing to its ability to be used on all engineering surfaces, which may be either electrically conductive or insulating, the AFM has become a popular surface profiler for topographic and normal force measurements on the micro and nanoscale [4].

Over the last few years various derivatives of SPM techniques have been developed. In the initial days, the SPMs were valued purely for their imaging capabilities. However, since a lot more physics of probe-sample interactions is known, SPM based methods have been developed for quantitative analyses of tribological, electronic, magnetic, biological, and chemical properties. For example apart from being used at extreme magnifications ranging from  $10^3$  to  $10^9$  in x, y and z directions for imaging macro to atomic dimensions with high resolution information and for spectroscopy, SPMs have been developed for various applications of scientific and industrial interest. For illustrative purpose, Fric-

tion Force Microscopy [5, 6], Scanning Electrostatic Force Microscopy (SEFM) [7, 8], Scanning Force Acoustic Microscopy (SFAM) [9, 10], Scanning Magnetic Microscopy (SMM) [11, 12], Scanning Near Field Optical Microscopy (SNOM) [13, 14], Scanning Kelvin Probe Microscopy (SKPM) [15, 16], Scanning Capacitance Microscopy (SCM) [17, 18, 19, 20] can be mentioned. AFMs have also been used for nanofabrication and nanomachining [4, 21].

Considering the versatility of applications and its capabilities to perform nanoscale characterization, AFM based characterization techniques are thus a natural choice to analyze local properties in graphene. The next sections of this chapter are intended

- to give a brief introduction to STM and AFM along with their basic operating principles. Furthermore, various variants of the AFM employed in this study, intended for local electrical characterization of substrate-supported graphene, are discussed.
- to describe the details of graphene sample preparation by the method of mechanical exfoliation of highly oriented pyrolytic graphite (HOPG) and high temperature annealing of SiC substrate to obtain epitaxial graphene. Identification and characterization of mono and few layers of graphene (FLG) is also explained.

## 2.2 Atomic Force Microscope

All SPM based methods have their origin in STM invented by Gerard Binnig and Heinrich Rohrer. STM is based on the principle of electron tunneling through a thin insulating film [22]. If a potential difference is applied to two metals separated by a thin insulating film, a current will flow because of the ability of the electrons to penetrate a potential barrier. To be able to measure a tunneling current, the two metals must be spaced no more than 10 nm apart. In an STM a sharp metal tip (one electrode of the tunnel junction) is brought close enough (0.3–1 nm) to the surface to be investigated (the second electrode) that, at a convenient operating voltage (10 mV–1 V), the tunneling current varies from 0.2 to 10 nA which is measurable. The tip is scanned over a surface at a distance of 0.3–1 nm, while the tunneling current between it and the surface is measured. The lateral scanning allows one to image surfaces with exquisite resolution, lateral-less than 1 nm and vertical-less than 0.1 nm, sufficient to define the position of single atoms. The very high vertical resolution of the STM is obtained because the tunnel current varies exponentially with

## 2.2. Atomic Force Microscope

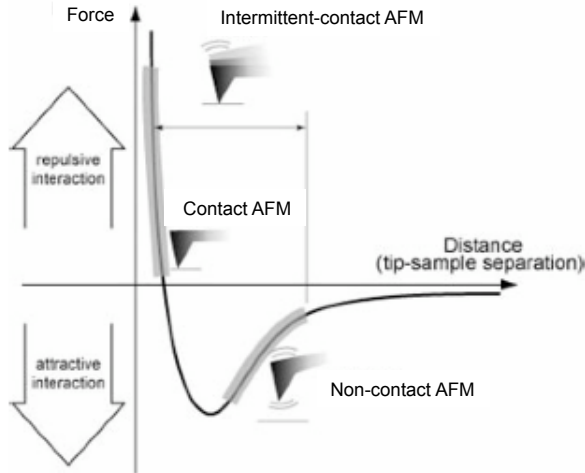


Figure 2.1: Interatomic force as a function of distance between tip and sample. Various modes of operation of AFM are also indicated.

the distance between the two electrodes, that is, the metal tip and the scanned surface. Typically, tunneling current decreases by a factor of 2 as the separation is increased by 0.2 nm.

Despite the phenomenal success of the STM, it has a serious limitation. It requires electrical conduction of the sample material, because it uses the tunneling current as a feedback. However, early STM experiments showed that whenever the tip-sample distance was small enough that a current could flow, significant forces would act collaterally with the tunneling current. Soon it was speculated that these forces could be put to good use in the AFM [2].

In an AFM, the force between the sample and tip is detected, rather than the tunneling current, to sense the proximity of the tip to the sample. The ultra-small forces (less than 1 nN) experienced by the AFM tip are measured by employing the motion of a very flexible cantilever beam (100 to 200  $\mu\text{m}$  long) having an ultra small mass. The AFM can be used either in a static or dynamic mode. In the static mode, also referred to as repulsive mode or contact mode [2], a sharp tip at the end of a cantilever is brought within a few angstroms from the sample surface. During initial contact, the atoms at the end of the tip experience a very weak repulsive force due to electronic orbital overlap with the atoms in the sample surface. The force acting on the tip causes a cantilever deflection,

which is measured by optical detectors. The deflection can be measured to within 0.02 nm, so for typical cantilever spring constant of 10 N/m a force as low as 0.2 nN can be detected. In the dynamic mode of operation for the AFM, also referred to as attractive force imaging or noncontact imaging mode, the tip is brought in close proximity (within a few nm) to, and not in contact with the sample. The cantilever is deliberately vibrated either in amplitude modulation (AM) mode [7] or frequency modulation (FM) mode [7, 23, 24, 25]. In the two modes, surface topography is measured by laterally scanning the sample under the tip while simultaneously measuring the separation-dependent force or force gradient (derivative) between the tip and the surface. In the contact (static) mode, the interaction force between tip and sample is measured by measuring the cantilever deflection. In the noncontact (or dynamic) mode, the force gradient is obtained by vibrating the cantilever and measuring the shift of resonant frequency of the cantilever. The attractive and repulsive force regimes are shown as a function of tip-sample separation in Figure 2.1.

### 2.2.1 Scanning capacitance microscopy and spectroscopy

Scanning Capacitance microscopy (SCM) is an important variant of AFM based techniques used for electrical characterization. In particular, it is used to achieve two-dimensional maps of majority carriers in semiconductor material. With inherent high spatial resolution of AFM, SCM thus is capable of measuring capacitance-voltage characteristics with nanometer scale resolution, by connecting a capacitance sensor to a conductive AFM tip. In this study, all capacitance measurements have been carried out using conductive tips made of heavily doped crystalline silicon ( $N_d=10^{19} \text{ cm}^{-3}$ ), on which Pt-Ir metallic film is deposited.

In SCM a metallic tip is scanned in contact mode onto the substrate. However, the lateral (shear) force associated with such scans would damage graphene flakes. Hence, in this study Scanning Capacitance Spectroscopy (SCapS) is employed. SCapS is an extension of standard SCM where a ‘step and measure’ approach is employed. In SCapS, the conductive AFM tip is placed on a discrete array of positions lifting the tip by 20 nm at every interval. Moreover, the vertical contact force of the tip on graphene can be suitably optimized to get good electrical contact. At each position of the tip a local capacitance is measured as a function of the applied bias voltage. A typical SCS measurement setup is shown in Figure 2.2. The sample is placed on a conducting chuck. A modulating bias  $\Delta V = V_g/2 + V_g \sin(\omega t)$ , with amplitude  $V_g$  and frequency  $\omega=100 \text{ kHz}$ , is applied to the chuck. The ultra-high-sensitive ( $10^{-21} \text{ F/Hz}^{1/2}$ ) capacitor sensor measures through a lock-in system the capacitance variations

## 2.2. Atomic Force Microscope

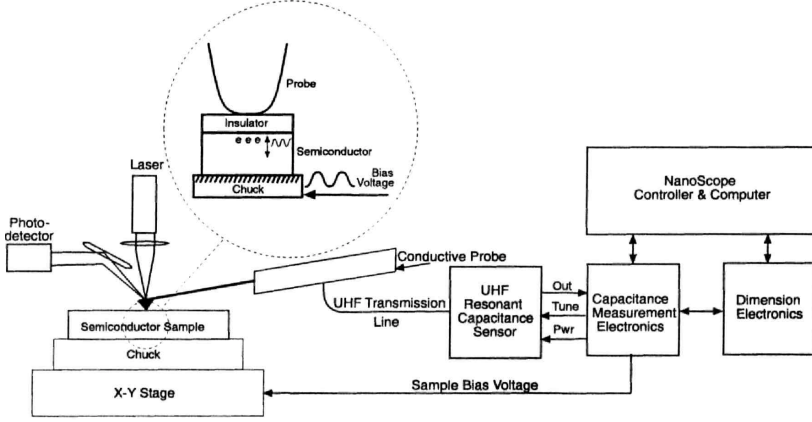


Figure 2.2: Experimental set-up for Scanning Capacitance Microscopy

$\Delta C(V_g)$  induced by the modulating bias.

### 2.2.1.1 The measuring principle

To understand the working principle of SCM let us consider the high frequency capacitance-voltage characteristics of a stack containing silicon dioxide layer on top of a uniformly doped n type silicon. A conductive AFM tip on  $\text{SiO}_2/\text{n-Si}$  stack forms a microscopic metal-insulator-semiconductor (MIS) system because the metallic tip works as a parabolic shaped gate with a hemispherical termination.

When an ideal MIS capacitor is biased from negative through positive voltages, the systems goes through three characteristic cases at the semiconductor surface.

- When a negative voltage ( $V < 0$ ) is applied to the metal chuck, majority carriers (electrons) accumulate near the oxide-semiconductor interface. This is called the accumulation regime.
- If a zero voltage ( $V = 0$ ) is applied to the tip, the system is in the so-called flat-band condition.
- When a small positive voltage ( $V > 0$ ) is applied to an ideal MIS capacitor, the majority carriers (electrons) are repelled from the interface and a depletion region is formed. The amplitude of the depletion region strongly

depends on the carrier concentration in the semiconductor region under the tip and on the applied D.C. voltage. This is called the depletion regime. When the applied positive voltage becomes larger than a threshold voltage  $V_t$ , the depletion of the semiconductor reaches its maximum and the oxide-semiconductor interface goes through the so-called inversion where, the number of holes (minority carriers) becomes greater than the number of electrons (majority carriers). This is the inversion regime.

This transformation of oxide-semiconductor interface reflects itself in the C-V characteristic. The total capacitance of a MIS system is explained as a series combination of the insulator capacitance and the semiconductor depletion region capacitance. In the accumulation regime, the semiconductor depletion width is negligible; therefore the corresponding capacitance contribution is extremely higher than the insulator capacitance contribution. Hence, in the accumulation case, being the lower contribution, the total capacitance corresponds to the insulator capacitance. In the depletion regime, the semiconductor depletion width grows with increasing the positive voltage thereby decreasing the corresponding capacitance contribution. The net result is the decrease in the total capacitance with increasing the positive voltage. When the positive voltage is increased beyond the threshold to drive the system in inversion, the depletion region width does not grow any more and the total capacitance reaches a constant minimum value, depending on the substrate carrier concentration.

However, measuring with SCM the systems measures the capacitance variations induced by the variations in the applied bias. One of the modes of operation of SCM is the ‘constant  $\Delta V$  measurements’.

### 2.2.1.2 Constant $\Delta V$ measurements

When a DC bias  $V_{dc}$  is applied to the metal tip a working point is fixed on the C-V characteristics. This working point is generally fixed near the flat-band voltage condition. For positive  $V_{dc}$ , a depletion width  $W$  is generated in the semiconductor. The depletion region width depends on the local carrier concentration under the tip. Furthermore, by applying a high frequency AC bias with amplitude  $\Delta V$ , the depletion region width is modulated around the value  $W$ ; consequently a capacitance variation  $\Delta C$  is produced. Usually, in a SCM measurement  $V_{dc}$  and  $\Delta V$  are initially fixed and are not varied during the scan. Therefore, for fixed DC and AC biases, the capacitance variation  $\Delta C$  depends on the local carrier concentration under the tip. Precisely, for n-type doped samples, this capacitance variation is positive and is larger for lower concentration substrates.



## 2.2. Atomic Force Microscope

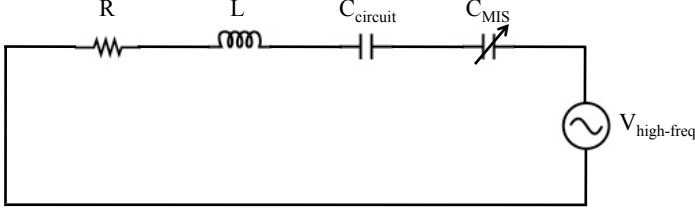


Figure 2.3: Schematic block diagram of resonating circuit used for ultra high frequency capacitor sensor

The capacitance variations corresponding to a variation of the applied bias are measured by an ultra-high-frequency (UHF) capacitor sensor, which is able to detect capacitance variations as small as  $10^{-21}$  Farad. The sensor works essentially as an RLC series resonating circuit (see the schematic in Figure 2.3), where the capacitance  $C_{circuit}$  represents the capacitance of the circuit and  $C_{MIS}$  represents the capacitance of MIS system under consideration, which changes during a scan with changing the local carrier concentration under the tip, for fixed  $V_{dc}$  and  $\Delta V$ . The measuring circuit is supplied by an ultrahigh frequency (990 MHz) voltage with an amplitude of about 200 mV.

The resonating frequency of the circuit, without the  $C_{MIS}$  contribution, is

$$f_0 = \frac{1}{\sqrt{LC_{circuit}}} \quad (2.1)$$

When the tip is in contact with the sample surface and the local MIS structure is formed, the capacitance  $C_{MIS}$  is added in series with  $C_{circuit}$ ; therefore, the resonating frequency shifts with respect to the frequency  $f_0$  by an amount depending on the capacitance variation  $\Delta C$  induced in the MIS system by the variation  $\Delta V$  in the sample polarizing frequency. To rid the measurements of the stray capacitances the UHF sensor is coupled to a lock-in amplifier, which amplifies the capacitance signal at the same frequency of the modulating voltage  $\Delta V$ . The SCM equipment used in the experiments presented in the following contains a quadratic lock-in amplifier, whose output is an arbitrary units signal, which is proportional to the absolute value of the  $dC/dV$ . This means that this equipment allows to obtain information only on the relative concentration levels in the different points of a semiconductor, but does not allow to have information on the kind of majority carriers (which is related to the sign of the  $dC/dV$ ).

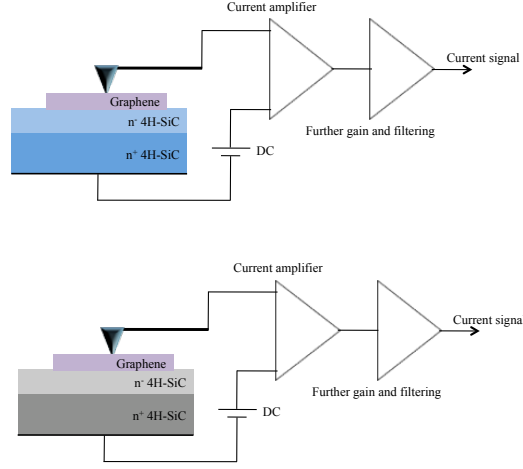


Figure 2.4: Schematic representation of (a) Conductive Atomic Force Microscopy, and (b) Torsion Resonance Conductive Atomic Force Microscopy applied to graphene.

### 2.2.2 Scanning Current Spectroscopy

Scanning Current Spectroscopy (SCurS) is derived from the conventional Conductive Atomic Force Microscopy (C-AFM). In SCurS a conductive AFM tip is scanned over the sample surface on a discrete array of positions, lifting the tip by 20 nm at each interval. At each position on the array a current-voltage characteristic is measured through a current sensor. One can distinguish two variants by considering the linear current amplifier used for the measurements. Usually, C-AFM employs a linear current amplifier, with a range 2 pA – 1  $\mu$ A. In the other variant, referred to as Tunneling AFM (TUNA), a more sensitive linear current amplifier with a range from 50 fA – 120 pA is employed. However, in this study we will not differentiate between the two and the two terms are used interchangeably. A typical measurement setup of SCurS is shown in Figure 2.4(a) as a simplified block diagram.

## 2.3. Sample preparation

---

### 2.2.3 Torsion Resonance - Conductive Atomic Force Microscopy

Torsion Resonance-Conductive Atomic Force Microscopy (TR-CAFM) is another variant of C-AFM. Torsion resonance mode overcomes limitations posed by contact mode and intermittent contact mode of imaging when used on soft and delicate samples. For example, in contact mode, the feedback maintains a constant force between the tip and the surface in the vertical direction. As a result, when the tip scans across the surface, the high lateral (shear) force can easily damage both the tip and the sample. On the other hand non-contact mode though allows low force imaging, thus reducing tip/sample wear, allows very little near-field interaction of the tip. For traditional oscillating tip modes, the AFM tip may spend up to 99% of its oscillation cycle in a regime with essentially no near-field interaction with the surface. This is problematic for the measurement of properties that demand near-field interactions e.g. measurement of tunneling current between tip and sample.

In TRmode the conductive tip is oscillated in a torsional or twisting mode (Figure 2.4(b)) and is maintained in the near-field regime (0.3 – 3 nm from the sample surface), at the boundary between direct contact and the long-range force regime. In this transition regime, the tip apex has a substantial near-field interaction with the sample, but can provide minimum damage to the sample itself. During the scans over the sample, the feedback loop keeps a constant torsion resonance amplitude and the conductive or tunneling current can be measured at each point simultaneously with the topographic image of the sample.

## 2.3 Sample preparation

Graphene has been adopted as a material of interest quite widely. This had led to many motivations for material synthesis. For this study graphene samples were obtained by mechanical exfoliation of HOPG and epitaxial growth on hexagonal SiC substrate. Sample preparation and graphene identification is discussed briefly in the following.

### 2.3.1 Mechanical exfoliation

Mechanical exfoliation, developed by Novoselov and Geim [26], involves a top-down approach to get graphene from highly oriented pyrolytic graphite (HOPG).

Mechanical exfoliation is by far the most popular method to get graphene owing to the fact that it does not require any sophisticated laboratory equipments and the flakes such obtained are enough for proof-of-concept studies in the laboratories. Using a common adhesive tape a thin graphite layer is peeled off from HOPG. With an inter-layer van der Waals interaction energy of about  $2 \text{ eV/nm}^2$ , the force required to exfoliate graphite is extremely weak, about  $300 \text{ nN}/\mu\text{m}^2$  [27]. After repeated thinning the flakes are transferred by gently pressing the tape onto suitable substrate.

However, the important aspect of sample preparation by exfoliation is the identification of grapheme layers by optical contrast microscopy [28, 29, 30] on suitably chosen thickness of silicon dioxide (typically 90 nm and 300 nm). On these substrates, the relative contrast of monolayer graphene is maximized at about 12% at 550 nm, where the sensitivity of human eye is optimal. This phenomenon has been explained by considering a Fabry-Perot multilayer cavity in which the optical path is added by graphene to the interference of the  $\text{SiO}_2/\text{Si}$  system is maximized at specific oxide thicknesses. Typically, sub-10 nm graphene flakes show darker to lighter shades of purple. We used extensive characterization by Optical contrast microscopy imaging (OM), TappingMode AFM, and microRaman ( $\mu\text{R}$ ) spectroscopy to identify monolayer flakes.

### 2.3.1.1 Micro-Raman spectroscopy and atomic force microscopy

In Figure 2.5(a), an OM image of a FLG sample is reported. The variable contrast in the image is indicative of a variable number of layers in the different regions of the sample. In particular, a lower contrast is associated to thinner layers. After an appropriate calibration, optical contrast variations can be used for a quantitative determination of the number of layers. In Figure 2.5(b),  $\mu\text{R}$  spectra measured on some selected positions indicated by the red, green and blue dots in the OM of Figure 2.5(a) are shown. As a reference, the spectrum obtained from HOPG is also reported. Raman spectroscopy is a very powerful method for the characterization of HOPG and FLG. In particular, it allows an unambiguous distinction between single layer, bilayer and multilayers in the case of graphene obtained by exfoliation of HOPG [31]. This is possible through a comparison of the relative intensity of the characteristic G peak (appearing at  $\sim 1580 \text{ cm}^{-1}$ ) and 2D peak (appearing at  $\sim 2680 \text{ cm}^{-1}$ ); and from the symmetry of the 2D peak in the Raman spectra. As it is evident from Figure 2.5(b), the spectrum measured in the flake region with the lowest optical contrast (position indicated by a red point in Figure 2.5(a)), exhibits a symmetric 2D peak with very high intensity compared with the G peak. These characteristic spectro-

### 2.3. Sample preparation

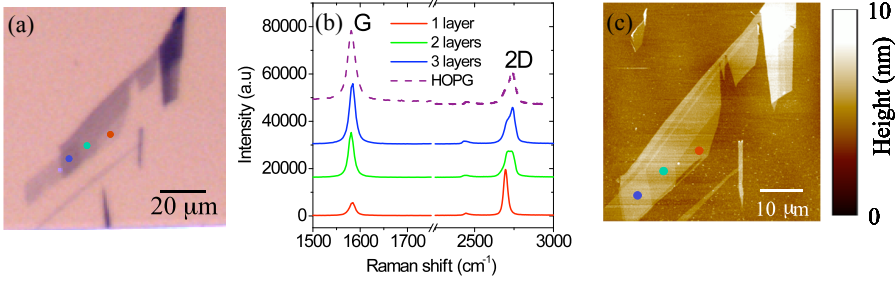


Figure 2.5: (a) Optical microscopy of a few layers graphene sample, (b) Micro-Raman spectra measured on some selected positions indicated by the red, green and blue dots in the optical image, and (c) Atomic force microscopy image of the flake.

scopic features have been associated uniquely to a graphene single layer. As it is evident, the relative intensity of the two peaks is very different in the case of a graphene bilayer, for which the 2D peak is not symmetric. For a number of layers larger than three the Raman spectrum becomes qualitatively similar to that of HOPG.

In Figure 2.5(c), an AFM morphological image on the same sample region as in Figure 2.5(b) is reported. In order to obtain quantitative information on the number of graphene layers from these morphological image, a height profile along the dashed line indicated in Figure 2.6(a) is reported in Figure 2.6(b). The zero height value is represented by the  $\text{SiO}_2$  surface level. Hence, from the profile in Figure 2.6(b) it is possible to deduce the height associated to the single layer, bilayer and trilayer of graphene previously identified by Raman spectroscopy. Interestingly, the measured height of a single layer with respect to the  $\text{SiO}_2$  is  $\sim 0.7$  nm, while the relative heights of the second layer with respect to the first one and that of the third layer with respect to the second are both  $\sim 0.35$  nm. The latter thickness value is very close to the interlayer spacing between graphene planes within HOPG. Hence, it seems that the measured step-height for a single layer of graphene is affected by an ‘offset’. This means that, in order to use AFM to determine the number of graphene layer in a sheet, it is necessary to have an accurate estimate of this value. To do this, the step height with respect to  $\text{SiO}_2$  was measured on a large number of flakes with variable number of layers, and with a ‘staircase’ structure similar to that illustrated in

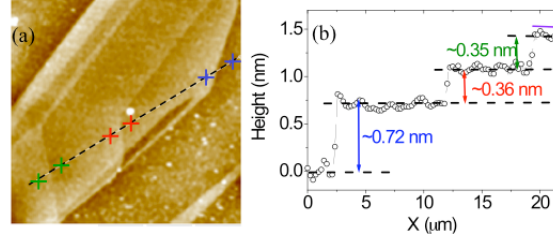


Figure 2.6: (a) AFM height map of the few layers graphene sample and (b) height profile along the indicated line.

Figure 2.6. For each flake, the single layer region was unambiguously determined by  $\mu$ R measurements. The number of layers for thicker regions could be obtained by counting the number of subsequent steps with  $\sim 0.35$  nm height.

In Figure 2.7(a), the average height  $h$  is reported as a function of the estimated number of layers  $n$ . These data have been fitted with the linear relation,  $h = t_{gr}n + t_0$ , where the interlayer spacing  $t_{gr}$  and the offset  $t_0$  are the fitting parameters. The best fit with the experimental data has been obtained for the values of  $t_{gr} = 0.36 \pm 0.01$  nm and  $t_0 = 0.28 \pm 0.06$  nm. Based on such calibration curve (determined height versus number of layers), it is possible to determine in an accurate and straightforward way the number of layer in a multiplayer sheet deposited on thermal  $\text{SiO}_2$  by an AFM analysis. However, this calibration procedure has to be repeated if the substrate material is changed, since the offset  $t_0$  depends on the specific substrate.

The value of this offset is partially related to the roughness of the substrate on which graphene is deposited, and also on the working principle of the AFM measurement itself. In TappingMode AFM, when the tip is close to the sample surface, the oscillation amplitude of the cantilever is strongly dependent on the local force gradient felt by the tip. During a scan the tip-sample force gradient is kept constant by a feedback loop, which changes the  $z$  piezo extension (i.e. the tip-sample distance) to maintain the oscillation amplitude fixed. The AFM image is a 2D map of the  $z$  piezo elongation for each tip position. This map corresponds to the ‘actual’ surface morphology only if the scanned surface has a uniform coating by the same material, otherwise it can be influenced by the different force gradient between the Si tip and different materials on the surface. In particular, when the AFM tip is scanned across the step between a single layer graphene and  $\text{SiO}_2$ , if the force gradient is larger on graphene than on

### 2.3. Sample preparation

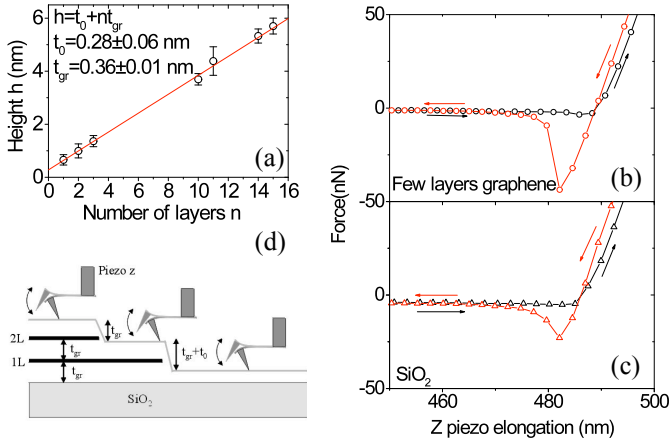


Figure 2.7: (a) Height of a few layers of graphene sheet versus the estimated number of layers in the sheet. (b) Force-distance curves measured on FLG and (c) on SiO<sub>2</sub>. The black curves are collected with the tip approaching to the surface, while the red ones with the curves retracting from the surface. (d) Schematic explanation of the offset affecting the Step-height between single layers of graphene and SiO<sub>2</sub>.

SiO<sub>2</sub>, the tip will move closer to SiO<sub>2</sub> than to graphene to maintain the oscillation amplitude constant. This picture is illustrated in Figure 2.7(b), (c) and (d). In order to verify this hypothesis, local force-spectroscopy measurements were carried out with the tip on SiO<sub>2</sub> and on FLG. The tip-sample force  $F$  as a function of tip-sample distance  $d$ , was measured in static conditions, i.e. no oscillation was imposed on the cantilever. The distance  $d$  was varied by changing the z-piezo elongation, while the force  $F$  was measured by measuring the cantilever deflection for each value of  $d$ . Cantilevers with elastic constant  $k = 20 \text{ N/m}$  were used for these measurements. The force-distance curves measured on FLG and on SiO<sub>2</sub> are reported in Figure 2.7(b) and (c), respectively. The black curves are collected during the tip approach to the surface, while the red ones during retraction from the surface. The different shape between the red and black curve is due to the adhesion force contribution, which tends to keep the tip attached to the sample surface during the z-piezo retraction. As it is evident the adhesion force between the tip and graphene is higher than between the tip and SiO<sub>2</sub>. Hence, during tapping mode measurements, the oscillating tip feels a higher force gradient during an oscillation cycle when on graphene than when on SiO<sub>2</sub>. This confirms the picture in Figure 2.7(b).

### 2.3.1.2 Optical contrast microscopy

Quantitative information on number of graphene layers can also be obtained from optical image, if an accurate analysis of the contrast is carried out. The optical contrast  $C$  can be quantitatively defined as,

$$C = \frac{(R_{sub} - R_{gr})}{R_{sub}} \quad (2.2)$$

where  $R_{gr}$  is the reflected light intensity by FLG and  $R_{sub}$  the reflected intensity by the substrate [32]. Typically a SiO<sub>2</sub>/Si substrate with 100 or 300 nm thick SiO<sub>2</sub> is chosen, since for these thicknesses optical contrast is maximized for light wavelengths in the visible range (400-700 nm), due to a constructive interference effect. Figure 2.8(c) and (d), illustrates the procedure to extract the optical contrast from an OM on a flake deposited on 100 nm thick SiO<sub>2</sub> and illuminated with light of 600 nm wavelength. In the considered case, the flake is a single layer of graphene, as confirmed by the AFM analysis in Figure 2.8(a) and (b). Based on this procedure, the optical contrast can be determined for flakes of different thickness. The number of layers in the flakes can be independently determined by AFM according to the calibration curve in Figure 2.7(a).



### 2.3. Sample preparation

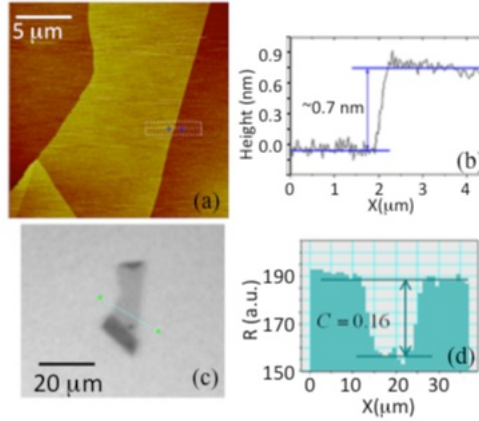


Figure 2.8: (a) AFM image and (b) height linescan for a single layer graphene flake deposited on 100 nm thick SiO<sub>2</sub>. (c) Optical microscopy on the same sample illuminated with light of 600 nm wavelength. (d) Illustration of the procedure to extract the optical contrast profile from the reflected light intensity.

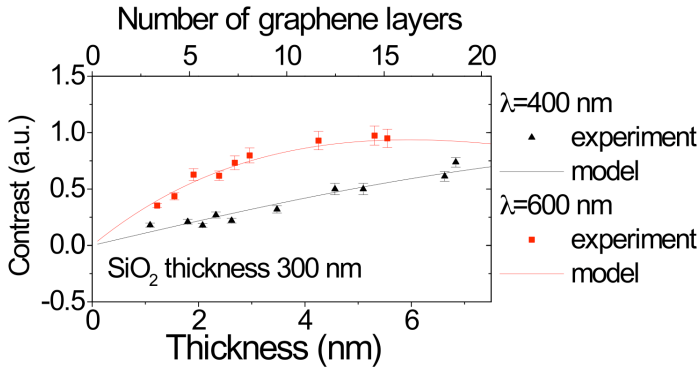


Figure 2.9: Optical contrast as a function of the flake thickness (and the number of graphene layers) for samples deposited on 300 nm SiO<sub>2</sub> and illuminated with light of 400 nm (black triangles) and 600 nm (red squares) wavelengths. The lines represent the calculated contrast as a function of the number of layers.

In Figure 2.9, the symbols represent the contrast as a function of the flake thickness (and the number of graphene layers) for samples deposited on 300 nm SiO<sub>2</sub> and illuminated with light of 400 nm (black triangles) and 600 nm (red squares) wavelengths. The lines represent the calculated contrast as a function of the number of layers. The reflected light intensities  $R_{sub}$  and  $R_{gr}$  are calculated using the Fresnel equations. The literature values of the complex refraction index of Si and SiO<sub>2</sub> as a function of the wavelength were used. For graphene, the real and imaginary part of the refraction index  $n_{gr}$  were calculated starting from its noticeable absorption properties in the wavelength range of visible light. In fact, recently, it has been shown that a single layer of graphene absorbs a fixed percentage ( $\sim \pi\alpha = 2.3\%$ , where  $\alpha$  is the fine structure constant) of the intensity of incident visible light [32]. Moreover, for few layers of graphene, the absorbance increases linearly with the number of layers. Based on these properties, refraction index values of graphene for the two considered wavelengths were calculated to be:

$$n_{gr}(\lambda_{400\text{ nm}}) = 2.57 - i0.81 \quad (2.3)$$

$$n_{gr}(\lambda_{600\text{ nm}}) = 2.53 - i1.21 \quad (2.4)$$

### 2.3.2 Epitaxial growth

Ultrathin graphitic films grow on hexagonal silicon carbide crystal when put through solid state graphitization process [33, 34]. Graphitic layers such produced are referred to as epitaxial graphene (EG), primarily because they share many of the same physical properties as exfoliated graphene. Epitaxial graphene, holds the potential, with recent development in the processing techniques [36, 35], in getting wafer-sized graphene needed for industrial application.

For our experiments epitaxial graphene growth was carried out on Si face of SiC in an inductively heated reactor, operating at a minimal pressure of  $5 \times 10^{-6}$  mbar. The growth temperature was 2000 °C and, to lower the Si outdiffusion process, a confining Ar pressure of 1 atm was used.

To confirm the presence of graphene and evaluate the number of layers we employed microRaman spectroscopy. Figure 2.10 shows the spectra collected at different spot positions on the sample surface along with a reference spectrum acquired on the 4H-SiC surface of the untreated sample. All Raman spectra collected on the graphitized sample surface show the characteristic 2D and G peaks, which confirm the presence of graphene, with the latter superimposed to

### 2.3. Sample preparation

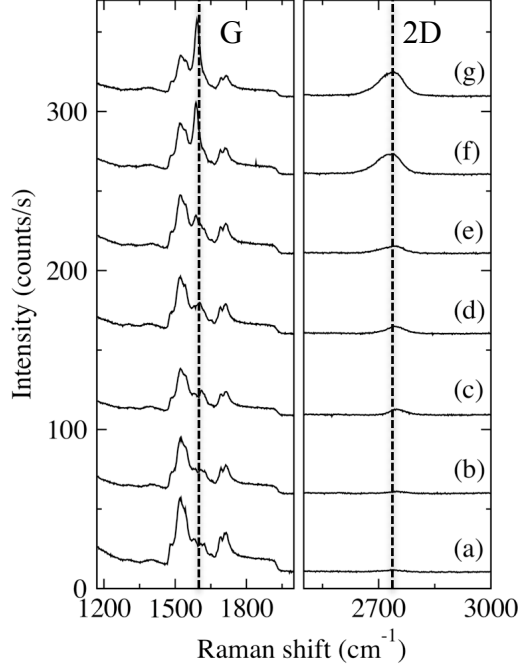


Figure 2.10: MicroRaman spectra collected on several positions on the epitaxial graphene grown on 4H-SiC(0001) substrate. The spectrum collected on starting substrate (bare SiC) is also shown for comparison.

the background signal associated with the substrate. Notice that the graphene fingerprint varies from spot to spot position. However the number of local graphene monolayers can be estimated after the correction for the background signal.

#### 2.3.2.1 Atomic force microscopy and transmission electron microscopy

An estimate on the number of graphene layers can also be achieved by selectively etching trenches in graphitized SiC substrate. This method is explained below on two representative samples - Sample 1 (annealed at 1600 °C) and Sample 2 (annealed at 1700 °C).

To start with, lithographically patterned stripes were etched out using O<sub>2</sub>

plasma. This plasma treatment is known to remove efficiently carbonaceous species through a chemical reaction leading to the formation of  $\text{CO}_2$ . Measuring the height of the etched regions in lithographically defined trenches at different positions on a graphitized SiC sample can be a straightforward method to estimate the thickness of epitaxial graphene layers at those positions. Considering that the noise level in the experimental height measurements by TappingMode AFM is typically  $<0.1$  nm and the interlayer height separation in a multilayer graphene sample is  $\sim 0.35$  nm, the method allows a very high accuracy in the determination of the number layers on few layer graphene samples. To obtain an accurate estimation, we checked if the underlying SiC substrate is slightly etched by the plasma processing used. To this aim, a lithographically patterned pristine SiC substrate was simultaneously etched together with the graphitized SiC samples. Figure 2.11 (a1), (b1) and (c1) show the Phase images on etched stripes in pristine and annealed samples. In PhaseMode imaging, the phase shift of the oscillating cantilever relative to the driving signal is measured. It is clear from the height profile taken on the stripes on pristine SiC that we etch  $\sim 2$  nm of SiC substrate (Figure 2.11 (a2)) and hence this depth must be subtracted while evaluating the number of layers on graphitized SiC [37].

We observed progressively deeper trenches for essentially same etching conditions on graphitized SiC (Figure 2.11 (b2) and (c2)). After subtracting the etched SiC depth (2 nm) and considering the interlayer distance in graphene (0.35nm) we found  $\sim 3.42$  and  $\sim 9.14$  layers for Sample 1 and sample 2 respectively.

To independently examine the annealed samples, we acquired cross-sectional TEM images (reported in Figure 2.12). We found that the number of graphene layers were 3 and 9, in quite good agreement with TappingMode AFM findings.

This method can easily be extended to estimate the coverage homogeneity of epitaxial graphene on the wafer-sized samples. Furthermore, considering the sensitivity of TappingMode AFM to sub-nanometer height variations, the method could be sensitive even to evaluate monolayer graphene coverage, provided that the SiC substrate over-etching during plasma processing is very accurately estimated.

### 2.3.2.2 Torsion Resonance Conductive Atomic Force Microscopy

To date, EG has been grown both on the Si or C-faces of 6H and 4H-SiC by high temperature treatments under partial pressure varying from ultra-high vacuum [33] (UHV) to atmospheric pressure in Ar ambient [35, 36]. During thermal annealing both Si sublimation and a reconstruction of the SiC surface

### 2.3. Sample preparation

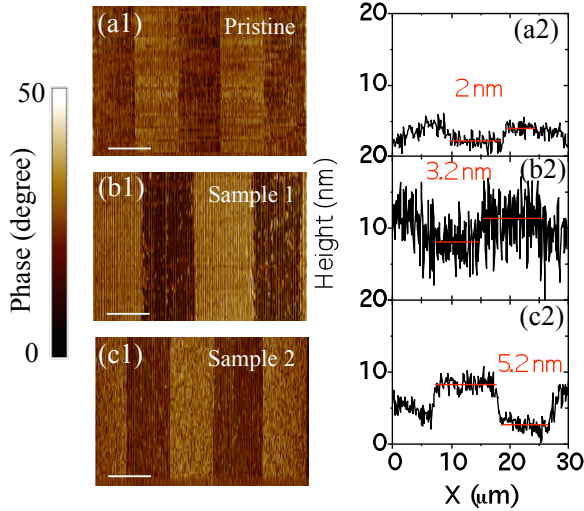


Figure 2.11: Estimation of number of graphene layers by etching graphitized SiC surface. The trenches are clearly seen in the phase images (a1), (b1) and (c1) (the scale bars are  $5\mu\text{m}$ ). The height profile taken over the etched regions on pristine 4H-SiC sample gives an estimation of overetched SiC. Progressively deeper trenches in (b) and (c) give an estimated 3, and 9 layers of graphene.

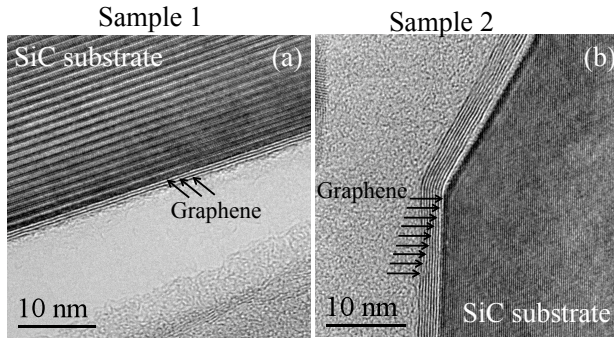


Figure 2.12: Fig. 3 High-resolution Transmission Electron Micrographs of graphitized 4H-SiC(0001) (a) Sample 1, and (b) Sample 2. Graphene layers appear evident on SiC substrate.

from initial atomic steps into large terraces (step bunching) occur. The large terraces represent preferential nucleation sites for graphene and the key factors to obtain homogeneous and thin EG sheets are (i) a low enough Si evaporation rate from the substrate and (ii) the formation of large homogeneous terraces on the reconstructed SiC surface. In comparison to UHV, annealing under Ar atmospheric pressure leads to a reduced Si evaporation rate (so that growth temperatures can be raised above  $>1600$  °C) and to larger surface terraces, giving rise to larger EG domains.

Since the width of the initial terraces is smaller on off-axis wafers (due to the miscut angle), cheap 6H on-axis SiC substrates are preferred for EG growth. On the other hand, the active area of SiC devices is commonly fabricated on low-doped epilayers grown on 4H off-axis (typically 4° or 8°-off) SiC substrates. Hence, investigating the EG growth on off-axis 4H-SiC wafers is mandatory to integrate graphene electronics with SiC devices for future RF applications.

We investigated the growth of EG on the (0001) face of 8°-off 4H-SiC epilayers grown on 4H-SiC substrates and compare with EG grown on on-axis SiC substrates under identical temperature and Ar overpressure conditions. Micro-Raman spectroscopy was done to get information at the micrometer scale on the average thickness uniformity of EG. TR-CAFM allowed then to determine the SiC areas covered by EG with nanoscale resolution [38].

TR-CAFM combines the non-invasive character of dynamic SPM in morphological mapping and the ability of nanoscale resolution current mapping of C-AFM. TR-CAFM is useful in identifying graphene and few layer graphene (FLG) deposited on top of SiC substrates [39]. This ability is due to the large difference in the Schottky barrier height (SBH) formed by the Pt tip with bare SiC ( $\sim 1.6 \div 1.7$  eV) and by the Pt tip with 4H-SiC coated with graphene. In the case of graphene exfoliated from HOPG and deposited (DG) on SiC, the Pt/DG/SiC SBH is  $\sim 0.8$  eV, whereas the Pt/EG/SiC SBH is lower ( $\sim 0.3$  eV). As a consequence, if Pt is positively biased with respect to the sample backside, graphene coated regions in the current maps appear highly conductive as compared to regions devoid of graphene. This high resolution mapping method is especially useful to study the initial stages of EG formation.

In the following, we focus on two representative samples: i) graphene grown on an 8°-off axis (0001) 4H-SiC epitaxial layer (designated as EG1) and ii) graphene grown directly on an on-axis (0001) 6H-SiC substrate (designated as EG2). On both samples, after optical inspection, Raman spectra were acquired at selected positions to probe the thickness homogeneity. Results are shown in Figure 2.10 for sample EG1 in order of increasing FLG thickness. The spectrum for untreated SiC is also shown for reference. The presence of characteristic G

### 2.3. Sample preparation

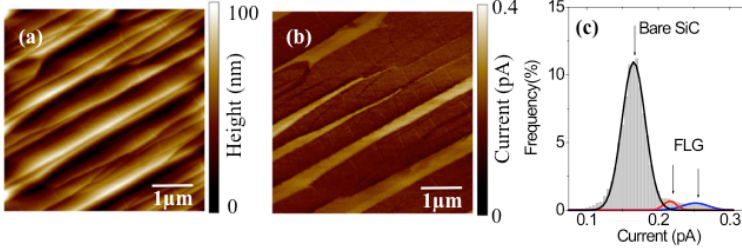


Figure 2.13: Torsion Resonance Atomic Force Microscopy map in (a) and the corresponding Torsion Resonance Conductive Atomic Force Microscopy map in (b). In (c) are shown histograms extracted from the current map in (b). Evaluated three regions (region with graphene coverage (curves (ii) and (iii)) and region devoid of graphene (curve (i)) are indicated distinctly.

and 2D bands, indicating the formation of EG, is evident. After correction for the background signal, we could estimate the number of graphene monolayers from the G band intensity [40].

The evaluated EG thickness varied from lower than 1 to 8 monolayers, which are obviously average values, within the area probed by the laser spot. To get higher resolution information on the coverage uniformity, especially in the areas with lower average thickness (about 1 and 2 monolayers) we carried out TR-CAFM mapping.

A typical example is shown in Figure 2.13(b) along with the morphological map (a). The surface morphology is characterized by large terraces (0.5 to 1 μm width) running parallel to the original steps of the off-axis wafer. The RMS roughness is 16 nm. The darker background in the current map corresponds to bare SiC, whereas the bright regions (higher current) are for SiC regions coated by FLG. Interestingly, changes in the current level can be noted within the brighter regions, probably associated to different numbers of monolayers. The images in Figure 2.13 describe the initial stages of EG formation on off-axis SiC, showing that the growth starts from the edge and follows the surface of terraces. To quantify the graphene coverage in this area, the current values measured in the map are plotted as histograms in Figure 2.13(c). The total distribution has been fitted with three Gaussian components: the curve numbered (i) corresponds to region devoid of graphene, the curves numbered (ii) and (iii) correspond to regions covered with EG of different thickness. The total number of counts under the last two components (curves (ii) and (iii) combined) gives

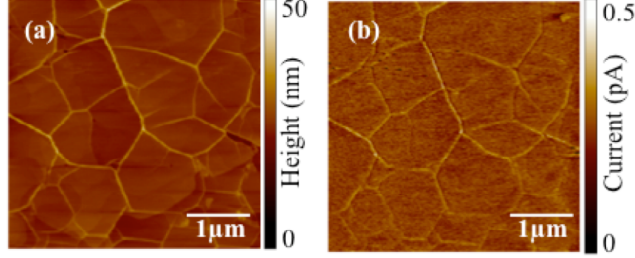


Figure 2.14: TR morphology (a) and current map (b) collected on EG2 sample.

the fraction of area covered by EG. We found  $\sim 15\%$ .

We then performed a similar investigation on sample EG2. Micro-Raman spectra indicated a much more uniform coverage with average thickness  $\sim 3$  monolayers. The corresponding TR-CAFM current map and torsional morphology are shown in Figure 2.14. It is interesting to compare the morphological maps in Figure 2.13 (a) and Figure 2.14(a). While on the off-axis sample a significant step bunching was observed after the high temperature thermal annealing, a flatter surface (RMS=2.4 nm) is obtained on the on-axis sample. The current maps are also distinctly different. A comparison of Figure 2.13(b) and Figure 2.14(b) shows that EG2 carries a uniform current all over the scanned area, implying nanoscale uniformity. This observation is in good agreement with most results already published on (0001) on-axis 6H-SiC substrates.

As a last point, the bright lines in the morphological map are the commonly observed ridges on epitaxial graphene [42, 41]. They arise during the sample cooling, due to the thermal expansion mismatch between graphene and SiC, to relieve the resulting stress [42]. But, more interesting, it can be also observed that they carry a higher current density. This phenomenon is not yet understood and deserves further investigations.

## 2.4 Summary

Owing to nanoscale lateral resolution Atomic Force Microscopy based characterization methods are obvious and important tools to probe local properties in graphene. Scanning Capacitance Spectroscopy (SCapS), Scanning Current Spectroscopy (SCurS) and Torsion Resonance Conductive Atomic Force Mi-



## 2.4. Summary

---

croscopy (TR-CAFM) provide various opportunities for non destructive electrical characterization of graphene.

Graphene samples for the study were obtained by mechanical exfoliation and thermal graphitization methods. In case of the exfoliated graphene samples extensive characterization of the flakes was carried out with Optical Microscopy (OM), MicroRaman Spectroscopy ( $\mu$ R) and TappingMode Atomic Force Microscopy.  $\mu$ R, which allows an unambiguous distinction between monolayers and bilayers, was used to perform a calibration of tapping mode AFM. In fact, height measurements by AFM are affected by an offset. After this calibration, a curve relating the height of a flake measured by AFM with the number of graphene layer was obtained. Finally, the optical contrast (OC) variations with FLG thickness measured for different wavelengths in the visible range and for different oxide thicknesses (from 100 to 300 nm). OC was correlated with the number of layers (independently measured by AFM). The complex refraction index of graphene was calculated starting from its absorption properties and used within the Fresnel equations to calculate the OC as a function of the number of layers.

For epitaxial graphene the identification and coverage homogeneity was checked with  $\mu$ R and TR-CAFM. TR-CAFM allows high-resolution current mapping which is especially useful in studying the initial stages of graphene formation on SiC substrate by thermal graphitization. To evaluate the number of layers on epitaxial graphene, in addition to  $\mu$ R, we demonstrated a method based on height measurements on selectively etched out trenches in graphitized SiC. This method is easily extendable to evaluate graphene layer homogeneity on a wafer scale.



# References

- [1] G. Binnig, H. Rohrer, Ch. Gerber, E. Weibel, Phys. Rev. Lett. 49, 57 (1982)
- [2] G. Binnig, C. F. Quate, Ch. Gerber, Phys. Rev. Lett. 56, 930 (1986)
- [3] G. Binnig, Ch. Gerber, E. Stoll, T. R. Albrecht, C. F. Quate, Europhys. Lett. 3, 1281 (1987)
- [4] B. Bhushan, Handbook of Micro/Nanotribology, 2nd edn. (CRC, Boca Raton 1999)
- [5] C. M. Mate, G. M. McClelland, R. Erlandsson, S. Chiang, Phys. Rev. Lett. 59, 1942 (1987)
- [6] R. Erlandsson, G. M. McClelland, C. M. Mate, S. Chiang, J. Vac. Sci. Technol. A 6 266 (1988)
- [7] Y. Martin, C. C. Williams, H. K. Wickramasinghe, J. Appl. Phys. 61, 4723 (1987)
- [8] J. E. Stern, B. D. Terris, H. J. Mamin, D. Rugar, Appl. Phys. Lett. 53, 2717 (1988)
- [9] V. Scherer, B. Bhushan, U. Rabe, W. Arnold, IEEE Trans. Mag. 33, 4077 (1997)
- [10] V. Scherer, W. Arnold, B. Bhushan, Surf. Interface Anal. 27, 578 (1999)
- [11] Y. Martin, H. K. Wickramasinghe, Appl. Phys. Lett. 50, 1455 (1987)
- [12] D. Rugar, H. J. Mamin, P. Guethner, S. E. Lambert, J. E. Stern, I. McFadyen, T. Yogi, J. Appl. Phys. 63, 1169 (1990)

- [13] D. W. Pohl, W. Denk, M. Lanz, Appl. Phys. Lett. 44, 651 (1984)
- [14] E. Betzig, J. K. Troutman, T. D. Harris, J. S. Weiner, R. L. Kostelak, Science 251, 1468 (1991)
- [15] Y. Martin, D. W. Abraham, H. K. Wickramasinghe, Appl. Phys. Lett. 52, 1103 (1988)
- [16] M. Nonnenmacher, M. P. O'Boyle, H. K. Wickramasinghe, Appl. Phys. Lett. 58, 2921 (1991)
- [17] F. Giannazzo, F. Priolo, V. Raineri, V. Privitera, A. Picariello, A. Battaglia, and S. Moffat, J. Vac. Sci. Technol. B 20, 414 (2002)
- [18] F. Giannazzo, D. Goghero, V. Raineri, S. Mirabella, and F. Priolo, Appl. Phys. Lett. 83, 2659 (2003)
- [19] L. Ciampolini, F. Giannazzo, M. Ciappa, W. Fichtner, and V. Raineri, Mater. Sci. Semicond. Process. 4, 85 (2001)
- [20] F. Giannazzo, V. Raineri, S. Mirabella, G. Impellizzeri, and F. Priolo, Appl. Phys. Lett. 88, 043117 (2006)
- [21] E. Delawski, B. A. Parkinson, J. Am. Chem. Soc. 114, 1661 (1992)
- [22] I. Giaever, Phys. Rev. Lett. 5, 147 (1960)
- [23] D. Sarid, V. Elings, J. Vac. Sci. Technol. B 9, 431 (1991)
- [24] F. J. Giessibl, Science 267, 68 (1995)
- [25] B. Anczykowski, D. Krueger, K. L. Babcock, H. Fuchs, Ultramicroscopy 66, 251 (1996)
- [26] K. S. Novoselov, A. K. Geim, S. V. Morozov, D. Jiang, Y. Zhang, S. V. Dubonos, I. V. Grigorieva, and A. A. Firsov, Science 306, 666 (2004)
- [27] Y. B. Zhang, J. P. Small, W. V. Pontius, P. Kim, Appl Phys Lett 86, 073104 (2005)
- [28] P. Blake, E. W. Hill, A. H. C. Neto, K. S. Novoselov, D. Jiang, R. Yang, et al., Appl Phys Lett 91, 063124 (2007)
- [29] L. Gao, W. Ren, F. Li, H-M. Cheng, ACS Nano 2, 1625 (2008)

## REFERENCES

---

- [30] I. Jung, M. Pelton, R. Piner, D. A. Dikin, S. Stankovich, S. Watcharotone, et al., *Nano Letters* 7, 3569 (2007)
- [31] A. C. Ferrari, J. C. Meyer, V. Scardaci, C. Casiraghi, M. Lazzeri, F. Mauri et al., *Phys. Rev. Lett.* 97, 187401 (2006)
- [32] R. R. Nair, P. Blake, A. N. Grigorenko, K. S. Novoselov, T. J. Booth, T. Stauber, et al., *Science* 320, 1380 (2008)
- [33] C. Berger, Z. Song, Z. Li, W. Wu, N. Brown, C. Naud, et al., *Science*, 312, 1191 (2006)
- [34] W. A. de Heer, C. Berger, X. Wu, P. N. First, E. H. Conrad, X. Li, T. Li, M. Sprinkle, J. Hass, M. L. Sadowski, M. Potemski, and G. Martinez, *Solid State Commun.* 143, 92 (2007)
- [35] C. Virojanadara, M. Syväjärvi, R. Yakimova, and L. I. Johansson, *Phys. Rev. B* 78, 245403 (2008)
- [36] K. V. Emtsev, A. Bostwick, K. Horn, J. Jobst, G. L. Kellogg, L. Ley, J. L. McChesney, T. Ohta, S. A. Reshanov, J. Röhrl, E. Rotenberg, A. K. Schmid, D. Waldmann, H. B. Weber, and Th. Seyller, *Nature Mater.* 8, 203 (2009)
- [37] S. Sonde, C. Vecchio, F. Giannazzo, C. Bongiorno, S. Di Franco, M. Rambach, E. Rimini, and V. Raineri, submitted to *Mater. Sci. forum* (2011)
- [38] S. Sonde, F. Giannazzo, J.-R. Huntzinger, A. Tiberj, M. Syväjärvi, R. Yakimova, V. Raineri and J. Camassel, *Mater. Sci. forum* 645-648, 607 (2010)
- [39] S. Sonde, F. Giannazzo, V. Raineri, and E. Rimini, *Phys. Status Solidi B*, 247, 912 (2010)
- [40] N. Camara, J.-R. Huntzinger, G. Rius, A. Tiberj, N. Mestres, F. Perez-Murano, P. Godignon and J. Camassel, *Phys. Rev. B* 80, 125410 (2009)
- [41] Luxmi, S. Nie, P. J. Fisher, R. M. Feenstra, G. Gu et al. *J. Electron. Mater.* 38,718 (2009)
- [42] G. F. Sun, J. F. Jia, Q. K. Xue, L. Li, *Nanotechnology* 20, 355701 (2009)



## Chapter 3

# Local electrostatic and transport properties in graphene

### 3.1 Introduction

The electronic capacitance is important in understanding fundamental electronic properties of a material. Classically, the capacitance is defined by the capability of a material to store electrical charges. In such cases the capacitance depends on the material geometry and the dielectric permittivity of the medium. However, the scenario changes if the device or material geometry is reduced to nanometer scale. In particular, low dimensional systems have finite density of states (DOS). As a consequence, the low dimensional systems are not able to accumulate enough charges to completely screen the external electric field. Particularly, under the effect of applied bias the changes in the screening charge of a two dimensional electron gas (2DEG) are finite. Under these circumstances the 2DEG manifests itself as a capacitor, a concept introduced by Luryi, commonly called the quantum capacitance ( $C_q$ ) [1].

To date, particular attention has been devoted to the study of the electrostatic behavior of graphene. The demonstration of conductance tunability by field effect through a biased gate [2] opened the way to the fabrication of field effect transistors in graphene. This property, along with the high measured mo-

bility ( $\sim 15000 \text{ cm}^2\text{V}^{-1} \text{ s}^{-1}$  at room temperature [3] which is almost independent of the 2DEG concentration, will be of interest for near-ballistic transport and ultrafast switching devices. Although the response of the graphene 2DEG to an electrostatic field has been widely investigated, its behavior under an AC gate bias is largely unexplored. However, this knowledge will be crucial both to understand the operation of graphene field effect devices as switches and to get a deeper insight into the physics of the 2DEG.

The carrier density in the FLG sheet is tuned by applying a DC bias to the backgate (highly doped Si or SiC substrate) with respect to a front contact. An excess of electrons (holes) is injected through this contact when a positive (negative) backgate bias is applied. Under stationary conditions, the Fermi level is constant in the whole layer (i.e., the graphene surface is equipotential) and it is shifted in the conduction (valence) band depending on the positive (negative) bias polarity. As a consequence, a uniform increase in the electron (hole) concentration is induced in the layer. In a typical transport experiment [4, 5] the carrier density and the mobility of the 2DEG are determined by Hall effect measurements on the graphene sheet for different values of the backgate DC bias. We, however, explored the behavior of the graphene 2DEG under the influence of an AC bias. Such investigation helped us evaluate the electrostatic as well as transport properties in graphene supported by insulating and semiinsulating substrate.

In the succeeding sections, methods to evaluate the electrostatic properties (quantum capacitance and density of states) and transport properties (electron mean free path) locally, based on SCapS are presented.

### 3.2 Screening length and quantum capacitance in graphene by scanning capacitance spectroscopy

In this study, we carried out a nanoscale investigation on the capacitive behavior of graphene deposited on a  $\text{SiO}_2/\text{n}^+\text{Si}$  substrate, with different  $\text{SiO}_2$  thickness (300 and 100 nm). The ‘graphene/insulator/semiconductor backgate’ could be described as a metal-insulator-semiconductor (MIS) system. A bias composed of a slowly varying DC voltage and a rapidly varying AC signal was applied to the macroscopic  $\text{n}^+\text{Si}$  backgate, while a nanoscale contact was obtained on graphene by the tip of an AFM. The probe was connected to a capacitance detector coupled to a lock-in amplifier to measure the capacitance variations



### 3.2. Screening length and quantum capacitance

---

induced by the AC bias component, as explained in Section 2.2.1 (refer to Figure 3.1). Whereas a DC bias ramp is expected to cause an increase in the carrier density, which is uniformly spread over the whole flake, the local capacitance measurements revealed that the capacitor effective area ( $A_{eff}$ ) responding to the AC bias is much smaller than the geometrical area of the graphene sheet.  $A_{eff}$  increases linearly with the bias in a symmetric way for bias inversion. Moreover it approaches to the tip contact area for very small biases. As discussed in the following, this linear behavior indicates that  $A_{eff}$  grows proportionally to the density of the nonstationary charges (electrons/holes) induced by the AC bias. Interestingly, decreasing the  $\text{SiO}_2$  thickness (from 300 to 100 nm) the slope of the  $A_{eff}$  versus  $V_g$  curve strongly increases (by a factor of  $\sim 50$ ). Finally, significant lateral variations in this area have been observed by placing the tip over an array of different positions on the graphene sheet.

The capacitive behavior of graphene can be described by its quantum capacitance  $C_q$ , which is defined as  $C_q = dQ/d\mu$ , with  $dQ$  and  $d\mu$  being the variations of the charge and of the chemical potential in graphene, respectively. The quantum capacitance per unit area  $C'_q$  is related to the density of states at the Fermi level  $D(E_F)$ , that is,  $C'_q \approx qD(E_F)$  [6]. In a graphene/insulator/semiconductor capacitor, this contribution adds in series to the classical MIS capacitance. Since graphene is typically deposited on thick insulating layers (300 or 100 nm  $\text{SiO}_2$ ), the series quantum capacitance contribution, which is much larger than the MIS capacitance contribution [6], cannot be appreciated in electrostatic field effect experiments. However, it is expected that for graphene field effect transistors fabricated on a few nanometer thick dielectrics and/or high- $\kappa$  dielectrics, quantum capacitance will be the major contribution to the device performances. Hence, the determination of graphene quantum capacitance is of crucial interest both from a basic physics point of view, since it gets access to the density of states, and from the applications point of view. The local quantum capacitance  $C_q$  in the contacted graphene region was here determined from the locally measured effective area by SCapS. The distribution of the values of  $C_q$  for different tip positions was obtained from the lateral variation in  $A_{eff}$ . Finally, the lateral variation of the density of states was also evaluated.

#### 3.2.1 Nanoscale capacitance measurements on graphene

After morphological characterization, SCapS was applied to locally investigate the capacitive behavior of graphene monolayers. As previously described in Section 2.2.1, this technique is derived from conventional SCM in which 2D maps of capacitance variation are obtained scanning the AFM tip in contact mode on

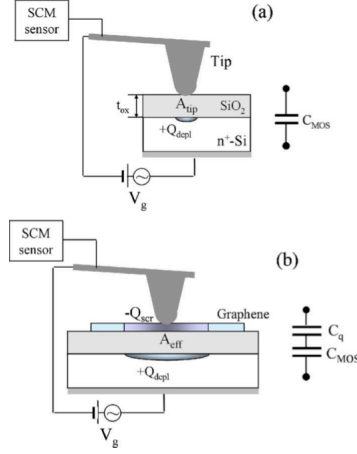


Figure 3.1: Schematic illustration of the experimental system, when the AFM tip is on SiO<sub>2</sub> (a) and on graphene (b)

the sample surface. In SCapS, the tip is placed in contact on a discrete array of different positions on the sample surface, and for each of those positions the capacitance variation versus bias characteristics are measured. A larger amount of information is collected than in the simple imaging mode, and obviously images can be reconstructed from arrays of spectroscopic data. SCapS allowed a high resolution and ‘nondestructive’ study of the capacitive behavior of graphene monolayers, which is not possible by conventional SCM imaging. The details on measurement set-up can be found in Section 2.2.1.

A large set of measurements was performed on different samples. More than 20 samples were probed on a given substrate, and several substrates, also considering different oxide thickness, were characterized. Moreover, several Pt-coated Si tips were used. First and foremost, the reproducibility of the measurement was checked, by repeating the measurements upon retracting the tip and contacting at the same spot. The same was also verified by acquiring a large number of curves with the tip fixed on the same position. As an example, a set of 25  $|\Delta C|$ - $V_g$  characteristics (with  $|\Delta C|$  the absolute value of the capacitance variation) measured with the tip on a fixed position on the 300 nm thick SiO<sub>2</sub> film is reported in Figure 3.2(a), while in Figure 3.2(b) the same number of  $|\Delta C|$ - $V_g$  curves measured with the tip fixed on a graphene monolayer deposited on the

### 3.2. Screening length and quantum capacitance

---

same substrate is shown. By measurements performed on many samples, similar data with the same spread were always reproduced.

The red and green curves are the calculated average characteristics of the two sets. The  $|\Delta C|$ - $V_g$  curves measured on  $\text{SiO}_2$  (Figure 3.2(a)) exhibit the typical high frequency behavior of a MIS capacitor on n-type Si, namely:  $\Delta C=0$  for  $V_g=0$  (flatband voltage) (refer to Section 2.2.1 for details);  $\Delta C < 0$  and  $|\Delta C|$  increasing with increasing  $V_g > 0$  (depletion regime);  $\Delta C > 0$  and  $|\Delta C|$  rapidly saturating at a constant value (equal to the oxide capacitance) for  $V_g < 0$  (accumulation regime). On the contrary, in the  $|\Delta C|$ - $V_g$  curves measured on graphene (Figure 3.2(b))  $|\Delta C|$  grows with  $V_g$  both for  $V_g > 0$  and for  $V_g < 0$ , although in an asymmetric way. Moreover, the  $|\Delta C|$ - $V_g$  curves measured on  $\text{SiO}_2$  (Figure 3.2(a)) exhibit in all the considered voltage range ( $-10 \div 10$  V) and for all the considered samples lower  $\Delta C$  values than those measured with the tip in contact with graphene (Figure 3.2(b)). Anyway, each set of curves measured at the fixed tip position (black lines in Figure 3.2(a, b)) exhibits a spread. This spread was assumed as the experimental error, since the same spread has been observed when measured on different samples, but with the tip on a fixed position.

To better visualize this spread, the histograms of the  $|\Delta C|$  values obtained for 25 measurements at  $V_g=-8$  V with the tip fixed on  $\text{SiO}_2$  and graphene are reported in the inserts of Figure 3.2(a,b), respectively. Finally, in Figure 3.2(c) a set of 25  $|\Delta C|$ - $V_g$  characteristics measured on an array of  $5 \times 5$  different tip positions (separated by  $1 \mu\text{m}$  step) in a region across the graphene monolayer and  $\text{SiO}_2$  is reported. As expected, in Figure 3.2(c), in this case both kinds of curves are present depending on the position of the tip. In the insert of Figure 3.2(c), the histogram of the  $|\Delta C|$  values at the fixed gate bias ( $V_g=-8$  V) is also reported. It is clearly bimodal, with the first peak (green Gaussian fit) associated to the different tip positions on  $\text{SiO}_2$  and the second one (red Gaussian fit) associated to the different tip positions on graphene. It is worth noting that the full-width at half-maximum (fwhm) of the  $\Delta C$  distribution obtained with the tip fixed on  $\text{SiO}_2$  (Figure 3.2(b)) is the same as the fwhm of the first peak in Figure 3.2(c) (tip at different positions on  $\text{SiO}_2$ ). This indicates that no lateral variations in the tip/oxide/semiconductor capacitance are detected within the experimental error, that is, the oxide thickness and the  $\text{n}^+\text{Si}$  doping are laterally uniform in the investigated length scale. On the contrary, the fwhm of the second peak in the bimodal distribution of Figure 3.2(c) (tip at different positions on graphene) is more than two times the fwhm of the distribution in Figure 3.2(b) (tip at a fixed position on graphene), indicating that the lateral variations in the  $|\Delta C|$  values measured for different tip positions

in graphene is larger than the experimental error. Since no appreciable lateral variations in the oxide/semiconductor capacitance was detected, the observed spread between the  $|\Delta C|$ - $V_g$  at different tip positions can be ascribed to lateral variations in graphene capacitance.

A comparison between such characteristics measured with the same tip on nearby areas of the same sample coated and uncoated with graphene offered a unique possibility to get information on the local capacitive behavior of this monolayer. In the following the ratio between the  $|\Delta C|$ - $V_g$  curves measured on graphene and on  $\text{SiO}_2$  will be considered. One of the advantages of this approach is to allow a measurement of graphene capacitance per unit area  $C'_g$  which is independent of the specific tip geometry. In fact, during the run on one sample, the  $|\Delta C|$ - $V_g$  curves are acquired both on graphene and  $\text{SiO}_2$  with an identical tip. If the measurement on the same sample is repeated with a different tip, the slight change in the tip geometry (i.e., in the contact radius) will cause a change both in the  $|\Delta C|$  values measured on graphene and  $\text{SiO}_2$ , but the ratio between those values will remain unchanged.

### 3.2.2 The effectively biased area in graphene

In Figure 3.3(a, b), left axis, the ratio  $N = |\Delta C_{tot}|/|\Delta C_{MOS}|$  between the average capacitance variations measured with the tip on graphene and with the tip on  $\text{SiO}_2$  is reported (symbols) versus  $V_g$ , for graphene on 300 and 100 nm  $\text{SiO}_2$  layers, respectively. In Figure 3.3(b), only data in the bias range from -2 to 2 V have been reported because larger biases yield too large capacitance variations (out of the sensitivity range of the capacitance sensor) when the tip is placed on graphene. It is evident that  $N \sim 1$  for  $V_g \sim 0$  and increases with increasing  $|V_g|$  both for  $V_g < 0$  and  $V_g > 0$ . For graphene on 300 nm (Figure 3.3(a), left axis),  $N$  increases linearly (the red line is the linear fit) with  $V_g$  for  $V_g < 0$ . Instead, for  $V_g > 0$ , after a linear growth region,  $N$  saturates for  $V_g > 2.5$  V. However, if the linear fit (red line) is considered up to  $V_g = 2.5$  V, a symmetric behavior is evident for bias sign inversion. For graphene on 100 nm (Figure 3.3(b), right axis),  $N$  grows linearly and symmetrically with respect to  $V_g$  in all the considered bias range. Interestingly, decreasing the  $\text{SiO}_2$  thickness (from 300 to 100 nm) the slope of the  $N$  versus  $V_g$  curve strongly increases (by a factor of  $\sim 50$ ).

In the following the physical meaning of  $N$  is discussed. When the tip is in contact with  $\text{SiO}_2$ , the Pt tip/ $\text{SiO}_2$ /n<sup>+</sup>Si system can be described as a nanometric MOS capacitor with capacitance  $C_{MOS} = A_{tip} \times C'_{MOS}$ , being  $C'_{MOS}$  capacitance per unit area and  $A_{tip} = \pi r_{tip}^2$  the tip contact area ( $r_{tip}$  is the tip

### 3.2. Screening length and quantum capacitance

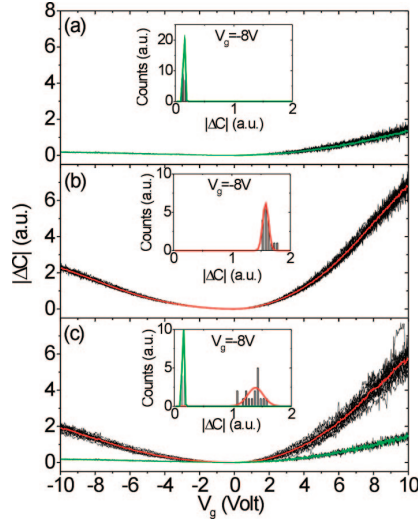


Figure 3.2: Typical set of 25  $|\Delta C|$ - $V_g$  characteristics measured with the tip at a fixed position on  $\text{SiO}_2$  (a) and at a fixed position on the graphene monolayer (b). In (c), set of 25  $|\Delta C|$ - $V_g$  characteristics measured on an array of  $5 \times 5$  different tip positions in the region across the graphene monolayer and  $\text{SiO}_2$ . The red and green curves are the calculated average values, respectively. In the inserts, the histograms of  $|\Delta C|$  at fixed bias ( $V_g = -8$  V) is reported.

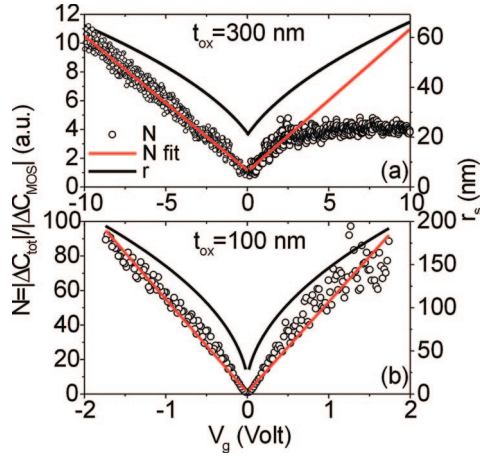


Figure 3.3: On the left axis, the average ratio  $N = |\Delta C_{tot}| / |\Delta C_{MOS}|$  between the capacitance variations measured with the tip on graphene and with the tip on  $\text{SiO}_2$ , for samples with 300 nm oxide thickness (a) and 100 nm oxide thickness (b). On the right axis, the average screening radius  $r_s$  calculated from  $N(V_g)$  for the sample with 300 nm oxide thickness (a) and 100 nm oxide thickness (b).

### 3.2. Screening length and quantum capacitance

---

contact radius, which is  $\sim 20$  nm, as measured by scanning electron microscopy). When the grounded tip is in contact with graphene, a positive backgate bias  $V_g$  causes the formation of a depletion region (with a positive charge  $Q=+Q_{depl}$ ) at the interface between  $\text{SiO}_2$  and Si, whereas a negative bias causes the accumulation of a negative charge  $Q=-Q_{acc}$  at the same interface. Since the electric field lines exhibit the highest density under the tip, also the charge at  $\text{SiO}_2/\text{Si}$  interface is localized in the area underneath the tip. That depletion (accumulation) charge induces in graphene an excess of electrons (holes) from the tip. When a DC bias only is applied to the backgate, those carriers spread uniformly in the graphene layer. When a modulating AC signal is added to the DC bias, the additional carriers following the modulating bias will add to the uniform background induced by the DC signal. The experimental data indicate that these carriers will distribute over an effective area  $A_{eff}$  around the nanoscale contact. In fact, the Pt tip/graphene/ $\text{SiO}_2/\text{n}^+\text{Si}$  system responds to the AC signal as a capacitor with capacitance  $C_{tot}=A_{eff} \times C'_{tot}$ , where  $C'_{tot}$  is the series combination of  $C'_{MOS}$  and  $C'_q$  capacitances per unit area, that is  $C'_{tot} = C'_{MOS}C'_q / (C'_{MOS} + C'_q)$ . As has been pointed out [6], for the considered  $\text{SiO}_2$  substrate thickness (100 or 300 nm),  $C'_{MOS}$ ,  $C'_q$ ; hence,  $C'_{tot} \approx C'_{MOS}$ . As a result, the ratio  $\Delta C_{tot}/\Delta C_{MOS}$  corresponds to the ratio between the effectively biased graphene area and the tip contact area, i.e.  $N(V_g) \approx A_{eff}/A_{tip}$ . The effectively biased area  $A_{eff}$  is directly related to the screening length  $r_s$  of the 2DEG in graphene by the simple relation  $A_{eff}=\pi r_s^2$ . Here we define  $r_s$  as the radius of the disk on which the nonstationary electron/hole charge is distributed. The average  $r_s$  has been calculated from  $N(V_g)$  and its behavior versus the applied backgate bias  $V_g$  is reported in Figure 3.3(a,b) (right axis) for the samples on 300 and 100 nm  $\text{SiO}_2$ , respectively.

#### 3.2.3 The quantum capacitance and local density of states in graphene

The charge per unit area ( $Q'$ ) at  $\text{SiO}_2/\text{Si}$  interface and the induced charge per unit area ( $Q'_{ind}$ ) in graphene are related to the oxide capacitance per unit area ( $C'_{ox}=\epsilon_0\epsilon_{ox}/t_{ox}$ , where  $\epsilon_0$  and  $\epsilon_{ox}$  are the vacuum dielectric constant and the relative dielectric constant, respectively, and  $t_{ox}$  the  $\text{SiO}_2$  layer thickness) and to  $C'_q$ , respectively. In fact  $|Q'|=C'_{ox}\Delta V_{ox}$  and  $|Q'_{ind}|=C'_q\Delta V_{gr}$ , where  $\Delta V_{ox}$  and  $\Delta V_{gr}$  are the potential falls across the  $\text{SiO}_2$  layer and the graphene sheet, respectively. The backgate bias is  $V_g = \Delta V_{ox} + \Delta V_{gr}$ . According to ref [6], for 100 or 300 nm thick  $\text{SiO}_2$  layer  $C'_q \gg C'_{ox}$ . Since  $|Q'|=|Q'_{ind}|$ , the potential

fall across the oxide layer can be approximated to the gate bias ( $\Delta V_{ox} \approx V_g$ ). As a result

$$|Q'_{ind}| \approx C'_{ox} V_g \quad (3.1)$$

and the quantum capacitance per unit area

$$C'_q \approx \frac{C'_{ox} V_g}{\Delta V_{gr}} \quad (3.2)$$

The experimentally observed linear dependence of  $N$  on  $V_g$  clearly indicates that the effective area  $A_{eff}$  grows proportionally to the induced charge density  $Q'_{ind}$  in graphene (see Equation 3.1). The saturation of the  $N$  value for  $V_g > 2.5$  V observed in the sample on 300 nm  $\text{SiO}_2$  can be explained considering that for positive biases higher than a threshold voltage, a positive charge (holes) inversion layer forms at  $\text{Si}/\text{SiO}_2$  interface. In high frequency measurements, the positive interface charge partially screens the backgate bias, and does not allow a further increase in the electron density in graphene. A similar saturation was not observed in the sample with 100 nm  $\text{SiO}_2$  because the inversion was not yet formed for the applied positive bias.

According to Equation 3.2, the dependence of the local quantum capacitance ( $C_q = A_{eff} C'_q$ ) on the applied bias  $V_g$  can be determined if the potential fall  $\Delta V_{gr}$  in graphene within the effective area is obtained. To obtain  $\Delta V_{gr}$ , the distributions of the local potential  $V_{gr}$  and of the screening charge density  $n_s$  ( $\text{cm}^{-2}$ ) were first calculated. The following charge density distribution well describes the electron (holes) density around the contact:

For  $0 < r < r_{tip}$

$$n_s(V_g) = \frac{C'_{ox} V_g r_s^2}{4q \left[ \frac{r_{tip}^2}{2} + \sigma^2 \exp\left(-\frac{r_{tip}^2}{2\sigma^2}\right) \right]} + C'_{ox} \frac{V_g}{2q} \quad (3.3)$$

and for  $r > r_{tip}$

$$n_s(V_g) = \frac{C'_{ox} V_g r_s^2}{4q \left[ \frac{r_{tip}^2}{2} + \sigma^2 \exp\left(-\frac{r_{tip}^2}{2\sigma^2}\right) \right]} \exp\left(\frac{-r^2}{2\sigma^2}\right) + C'_{ox} \frac{V_g}{2q} \quad (3.4)$$

In the Equations 3.3 and 3.4,  $r$  is the radial coordinate from the center of the tip-graphene contact,  $r_{tip}$  is the tip radius, and  $q$  is the electron charge. The parameter  $\sigma$  accounts for the spread of the induced charge around the contact. We assume that the screening length is  $r_s(V_g) = 3\sigma + r_{tip}$ . In Figure 3.4(a,c),



### 3.2. Screening length and quantum capacitance

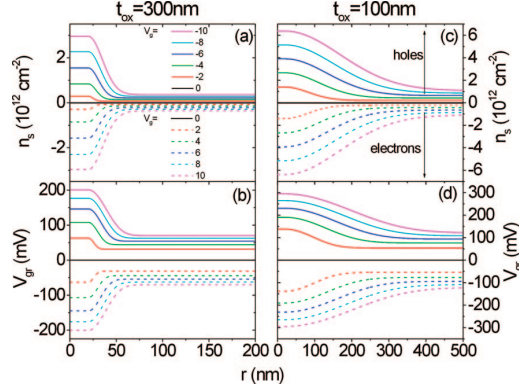


Figure 3.4: Screening charge density distribution for different values of the applied bias  $V_g$ , for the sample with 300 nm oxide thickness (a) and 100 nm oxide thickness (c). Local potential on graphene  $V_{gr}(r)$  for different values of  $V_g$ , for the sample with 300 nm oxide thickness (b) and 100 nm oxide thickness (d).

the screening charge density distribution is reported for different values of the applied bias  $V_g$ , in the cases of graphene on 300 and 100 nm  $\text{SiO}_2$  substrates, respectively. For a fixed gate bias, a uniform background density is induced by the DC voltage, whereas the peak value in the AC bias induces an excess of carriers, which redistributes within the effective area. The distribution is flat under the contact area and decays outside that area with tails, whose extension increases with increasing the bias. For graphene on 100 nm  $\text{SiO}_2$  those tails are much longer than in graphene on 300 nm  $\text{SiO}_2$ .

The local potential  $V_{gr}(r)$  in graphene at the coordinate  $r$  corresponds to the chemical potential  $\mu$  [7, 8]. Because of the linear density of states versus  $\mu$  in graphene, the carrier density varies with the square of the chemical potential  $\mu$ ; hence, the following relation can be used to describe the dependence of  $V_{gr}(r)$  on  $n_s(r)$

$$V_{gr}(r) = \frac{\sqrt{\pi} \hbar \nu_F}{q} \sqrt{|n_s(r)|} \quad (3.5)$$

where  $\hbar$  is the reduced Planck's constant and  $\nu_F \approx c/300$  )  $10^6$  m/s is the Fermi velocity of the Dirac electrons in graphene 2DEG. The behavior of  $V_{gr}$  versus  $r$  for different values of the applied back-gate bias is reported in Figure 3.4(b,d)

in the cases of graphene on 300 and 100 nm SiO<sub>2</sub> substrates, respectively.

Finally the potential drop  $\Delta V_{gr}$  in the effective area will be calculated as the average of  $V_{gr}(r)$  on that area, that is

$$\Delta V_{gr}(V_g) = \frac{\int_0^{r_s} V_{gr}(r) 2\pi r dr}{\int_0^{r_s} 2\pi r dr} \quad (3.6)$$

The behavior of  $\Delta V_{gr}$  versus the applied bias  $V_g$  is reported in Figure 3.5(a) for the two oxide thickness. Figure 3.5(b) shows the dependence on  $V_g$  of the quantum capacitance  $C_q = A_{eff} C'_q$ , with  $C'_q$  obtained according to Equation 3.2. Finally, the density of states (DOS) of graphene, which is related to the quantum capacitance per unit area, that is,  $DOS = C'_q/q$ , is reported in Figure 3.5(c). According to the quantum capacitance definition, the excess charge  $Q_{ind}$  induced in graphene by the bias  $V_g$  can be obtained by integrating the curve in Figure 3.5(b) from 0 to  $V_g$ . From the integration of the DOS curve in Figure 3.5(c) within the same limits, the number of states per unit area that can be occupied by the induced charge is obtained. Since a limited number of states per unit area is available for a fixed bias, the minimum area  $A_{DOS}$  that is necessary to accommodate the charge  $Q_{ind}$  can be obtained as

$$A_{DOS} = \frac{\int_0^{V_g} C_q(V'_g) dV'_g}{q \int_0^{V_g} DOS(V'_g) dV'_g} \quad (3.7)$$

In Figure 3.5(d) the comparison between the  $A_{DOS}$  (right scale), obtained according to Equation 3.7, and the effective area  $A_{eff}$  (left scale), obtained from the data Figure 3.3, is reported for both oxide thicknesses. It is worth observing for both samples the very good agreement between  $A_{eff}$  and  $A_{DOS}$  (which differ only for a geometrical factor  $\pi^{1/2}$ ). This indicates that the area on which the induced charge spreads is determined by the available density of states in graphene.

All of the data reported from Figure 3.3 to Figure 3.5 rely on the average curves of Figure 3.2(c). However, performing the same calculations for all the single characteristics measured at different tip positions in graphene, information on the lateral uniformity of the screening length, of the quantum capacitance and of the density of states can be obtained. In Figure 3.6(a) the  $r_s$  versus  $V_g$  curves are reported for all the tip positions on graphene (on 300 nm SiO<sub>2</sub>) and in the insert of the same figure, the histogram representing the distribution of the  $r_s$  values for fixed  $V_g = -5$  V is reported. Similarly, Figure 3.6(b) shows the  $C_q$  versus  $V_g$  curves for all the tip positions and (in the insert)

### 3.2. Screening length and quantum capacitance

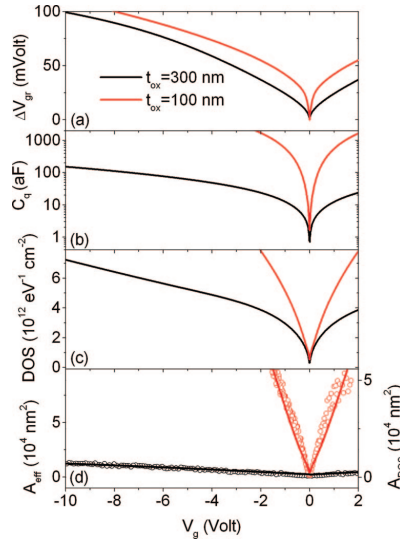


Figure 3.5: Potential drop in graphene  $\Delta V_{gr}$  (a), quantum capacitance  $C_q$  (b), density of states DOS (c) versus  $V_g$  for the sample with 300 nm oxide thickness (black line) and 100 nm oxide thickness (red line). In (d) the minimum area ADOS necessary to accommodate the charge induced by the bias  $V_g$ , according to the density of states in graphene, is reported on the right scale, whereas the effective area determined from the data in Figure 3.3 is reported on the right scale.

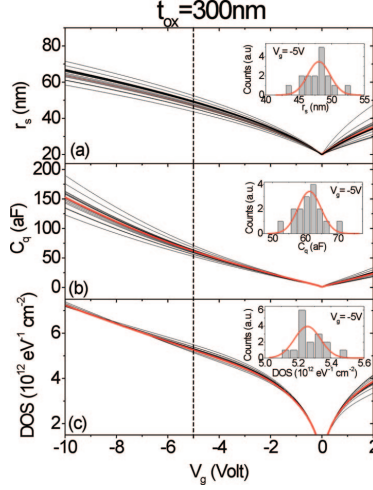


Figure 3.6: The  $r_s$  vs  $V_g$  curves for all the tip positions on graphene (a) and, in the inset, the histogram of the  $r_s$  values distribution for fixed  $V_g = -5$  V. Similarly, in (b), the  $C_q$  vs  $V_g$  curves for all the tip positions and, in the inset, the histogram of the  $C_q$  values distribution for fixed  $V_g = -5$  V are shown. Finally, in (c), the DOS vs  $V_g$  curves for all the tip positions and, in the inset, the histogram of the DOS values distribution for fixed  $V_g = -5$  V are shown.

the histogram representing the distribution of the  $C_q$  values for a fixed  $V_g = -5$  V. Finally, it was interesting to understand the lateral variations in the density of states. To this aim, in Figure 3.6(c) the DOS is reported versus  $V_g$  for all the tip positions on graphene in Figure 3.2(c). The histogram of the DOS at  $V_g = -5$  V is reported in the inset.

### 3.2.4 Discussion

Very recently, a different technique, the scanning single electron transistor (SET) probe microscopy (allowing ultra-high sensitive surface potential measurements) was used to determine the lateral variation of the local compressibility ( $\partial\mu/\partial n_s$ ), i.e. the reciprocal of the local density of states, in graphene flakes on a  $\text{SiO}_2/\text{n}^+\text{Si}$  substrate, for different values of the backgate bias [9]. Those lateral fluctuations were related to submicrometer lateral variations of the carrier density in graphene, which, in turn, were ascribed to ‘disorder’, due both to structural

### 3.2. Screening length and quantum capacitance

---

defects in the crystal and to chemical doping by adsorbates on its surface. SET microscopy is an extremely powerful method, but its spatial resolution is quite poor ( $\sim 100$  nm) compared to other SPM based methods, like scanning capacitance microscopy/spectroscopy. Because of this spatial resolution limitation, only an upper bound to the length scale of the disorder in graphene ( $\sim 30$  nm) was estimated in ref [9]. In the present work, we show the lateral fluctuations in the quantum capacitance and in the density of states by a completely different approach, that is, by nanoscale capacitance measurements. In particular, we observed that, for a fixed modulating bias amplitude, the effective area on which the induced screening charge is distributed changes with the lateral position; these lateral variations in the screening length (defined as the radius of the circular effective area) produce lateral variations in the  $C_q$  and DOS (see Figure 3.6(b,c)). The lateral fluctuations in the screening length could be related to disorder also. It is worth to note how the full-width at half-maximum of the  $r_s$  distribution (see insert of Figure 3.6(a)), which is  $\sim 5$  nm, gives a measure of the disorder length scale.

In the next subsection, as a continuation of this discussion, the effect of the substrate dielectric permittivity on screening length and quantum capacitance and of graphene is discussed.

#### 3.2.5 Influence of dielectric environment

Contrary to other two-dimensional systems, graphene has unique Dirac-type band structure of low-energy quasi-particles [2]. One of the consequences of that is  $C_q$  is proportional to the Fermi level measured from the Dirac point ( $E_F$ ) as opposed to other two dimensional systems where  $C_q$  contribution is constant and comparatively small [10]. Hence being a fundamental property of 2DEG in graphene,  $C_q$  as a function of  $E_F$  is expected to remain constant on different substrates in the absence of any interaction with the substrate. However, since the electrons in graphene are confined to one layer of atomic thickness, the electronic transport properties are affected enormously by the surrounding environment [11]. Engineering the dielectric environment of graphene is one of the methods applied to tailor the electronic transport properties. In this section we discuss a comparative investigation of the quantum capacitance in graphene deposited on substrates with different dielectric permittivity, viz.  $\text{SiO}_2$  and high- $\kappa$  dielectric, Strontium Titanate ( $\text{SrTiO}_3$  – STO).

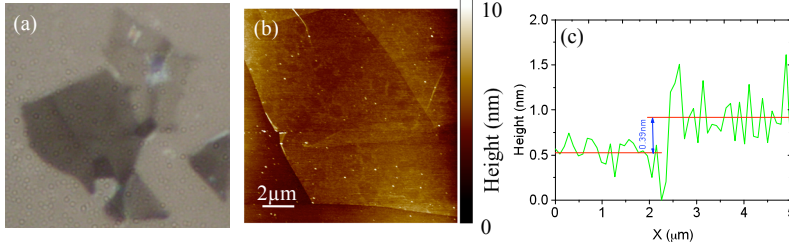


Figure 3.7: (a) Optical micrograph showing graphene deposited on STO. Mono-layer region can be seen with lighter contrast in a multilayer stack. (b) Tapping mode AFM micrograph of a representative DG-STO flake and (c) corresponding height profile in a linescan on monolayer-SrTiO<sub>3</sub> region.

### 3.2.5.1 Graphene on high- $\kappa$

Graphene flakes were obtained by standard mechanical exfoliation of HOPG and deposited (i) on 100 nm SiO<sub>2</sub> thermally grown on degenerately doped n<sup>+</sup>Si (referred to as DG-SiO<sub>2</sub> in the following) and (ii) on 60 μm single crystal Strontium Titanate (SrTiO<sub>3</sub>) (referred to as DG-STO in the following). Pure STO crystal is an insulator at room temperature with a band gap of 3.15 eV [12]. At room temperature the relative permittivity of [001] oriented STO has been determined to be 330±10 [13]. Graphene flakes were identified by optical contrast microscopy [14] and the flakes showing lowest contrast were further analyzed by TappingMode Atomic Force Microscopy. Figure 3.7 shows a representative graphene flake on STO along with the corresponding linescan on a monolayer region.

### 3.2.5.2 Enhanced $A_{eff}$

Figure 3.8 shows typical SCapS characteristics obtained on DG-SiO<sub>2</sub> and DG-STO. For comparison the SCapS characteristics obtained on bare substrates are also reported. Two distinct families of curves, corresponding to the tip positions ‘on graphene’ and ‘on substrate’, can be clearly identified. Clearly, the characteristics ‘on graphene’ are much higher than the corresponding characteristics ‘on substrate’ in both the cases.

The evaluated  $A_{eff}$  is reported in Figure 3.9(a) as a function of Fermi level shift from the Dirac point. It is evident that the  $A_{eff}$  observed on DG-STO is significantly higher than on DG-SiO<sub>2</sub>. Higher  $A_{eff}$  has further ramifications

### 3.2. Screening length and quantum capacitance

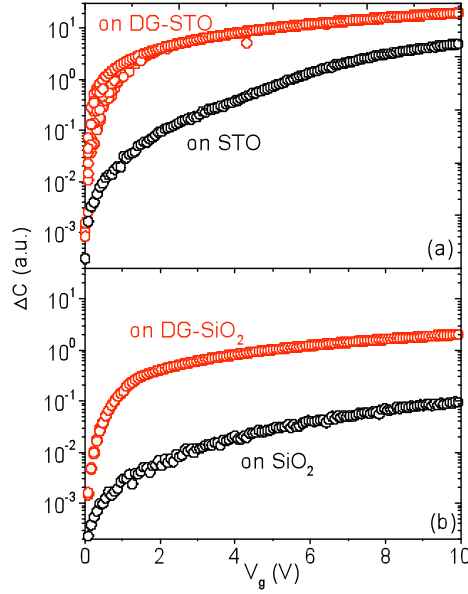


Figure 3.8: Representative characteristics obtained by Scanning Capacitance Spectroscopy (SCapS) on (a) graphene deposited on  $\text{SrTiO}_3$  (DG-STO) and (b) graphene deposited on  $\text{SiO}_2$  (DG-SiO<sub>2</sub>). Two distinct families of curves correspond to tip position ‘on graphene’ and ‘on substrate’ as indicated. A typical scan comprises of an array of  $5 \times 5$  positions with an inter-step distance of  $1 \mu\text{m} \times 1 \mu\text{m}$ .

since  $A_{eff}$  allows evaluating  $C_q$  (as a function of Fermi level ( $E_F$ )) by the relation,

$$C_q(E_F) = \frac{A_{eff}q^2}{\sqrt{2\pi}\hbar^2\nu_F^2 f(N)} E_F \quad (3.8)$$

where,  $f(N)$  is a function of the ratio  $A_{eff}/A_{tip}$  as defined in the previous section. The  $E_F$  in graphene is deduced by the relation

$$E_F = \hbar\nu_F\sqrt{\pi n} \quad (3.9)$$

where  $n$  is the carrier density obtained at a given gate voltage ( $V_g$ ) with  $n=C'_{ox}V_g/q$ . The calculated  $C_q$  is reported in Figure 3.9(b). We observed  $\sim 10\times$  higher  $C_q$  on STO as compared to on  $\text{SiO}_2$  (Figure 3.9(c)). The observed increase in the  $C_q$  is due prominently to the enhanced  $A_{eff}$  for DG-STO. It should be noted that  $A_{eff}$  is influenced by the structural quality of the graphene sheet [15, 16] as well as on the dielectric environment [17]. A better dielectric screening of charged impurities on graphene and/or at the interface between graphene/substrate by the STO for DG-STO could very well be one of the factors showing enhanced  $A_{eff}$ . Since  $C_q$  also enters the formalism for conductivity of graphene [18], transport properties are also expected to improve with enhanced  $C_q$ . Indeed, improved electron mean-free path has been observed in graphene if supporting substrate has high dielectric permittivity [17].

### 3.3 Local electron mean free path by scanning capacitance spectroscopy

One of the main research issue in the electron transport studies in graphene is to understand how the various scattering sources (charged impurities, lattice defects, and lattice disorder, including local strain and irradiation damage) limit the electron mobility [19]. The random distribution of these scattering sources is expected to cause local inhomogeneities in the transport properties, which can adversely influence the reproducible operation of graphene nanodevices. Under this point of view, nanoscale resolution methods are urgently required to probe the lateral homogeneity of the transport properties in graphene sheets. As a matter of fact, electron mobility is commonly measured on test patterns fabricated on micrometer sized graphene samples and is, therefore, an average value on that area. Local measurements of the electron mobility thus remains unexplored. In this section, we demonstrate a method based on SCapS on



### 3.3. Local electron mean free path by scanning capacitance spectroscopy

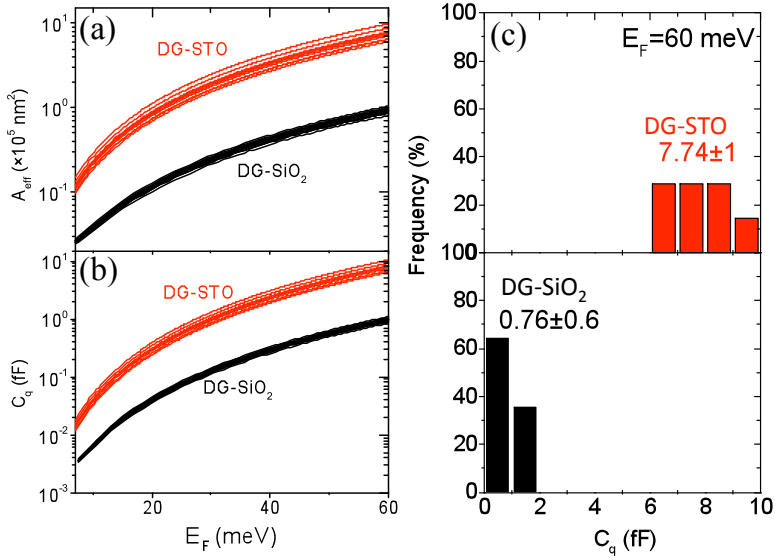


Figure 3.9:  $A_{eff}$  as evaluated from the local capacitive measurements on DG-STO and DG-SiO<sub>2</sub> as a function of  $E_F$  is showed in (a). The corresponding  $C_q$  is depicted in (b). A relative increase in  $C_q$  of  $\sim 10\times$  can be seen from the histograms in (c).

graphene which can be used to determine the ‘local’ electron mean free path  $l$  (defined as the average of the distances traveled by electrons between ‘few’ subsequent scattering events) and mobility.

Since electrons diffuse from the tip contact on graphene over a length  $r_s$  traveling at velocity  $\nu_F=1.1 \times 10^6$  m/s (the graphene electron Fermi velocity) [19], the diffusivity of the electrons can be expressed as,

$$D = \frac{\nu_F r_s^2}{2} \quad (3.10)$$

On the other hand, the diffusivity  $D$  can be related to electron mobility,  $\mu$  by the generalized Einstein relation

$$\frac{D}{\mu} = \frac{n}{\left(q \frac{\partial n}{\partial E_F}\right)} \quad (3.11)$$

all the symbols have their usual meaning. The Fermi energy in graphene corresponds to the chemical potential. Theoretical works have demonstrated that ‘disorder’ causes strong modifications of the density of states in graphene at the Dirac point, whereas far from the Dirac point density of states remains linearly dependent on the energy [20]. For the considered gate bias  $V_g=1$  V, the Fermi level is far enough from the Dirac point ( $E_F \tau / \hbar > 1$ , with  $\tau$  the electrons relaxation time) to assume a linear density of states. Hence, the carrier density is given by,

$$n = \frac{E_F^2}{\pi \hbar^2 \nu_F^2} \quad (3.12)$$

Putting Equation 3.10 and 3.12 into 3.11,

$$\mu = \frac{q \nu_F r_s}{E_F} \quad (3.13)$$

Furthermore, far enough from the Dirac point, Boltzmann transport theory has been used to describe the electronic transport in SLG [21, 22] and  $\mu$  has been expressed in terms of electron mean free path  $l$  as follows:

$$\mu = \frac{q l}{\hbar \sqrt{\pi n}} \quad (3.14)$$

From this discussion, it is clear that the measured  $r_s$  by SCapS corresponds to  $l$ . Figure 3.10 depicts representative graph of local  $l$  evaluated for graphene

### 3.4. Summary

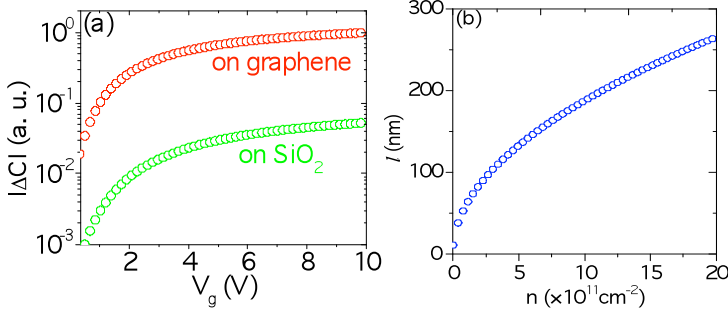


Figure 3.10: Local capacitance measurements (a) can be used to evaluate the electron mean free path in graphene (b) supported by insulating and/or semi-insulating substrates.

exfoliated-and-deposited on 100 nm SiO<sub>2</sub>. The  $l$  is plotted as a function of carrier density  $n$ , obtained by  $n = \frac{C'_{ox} V_g}{q}$ .

This continuum treatment, using the concepts of diffusivity and mobility and the Einstein relation, results to be justified on the ‘mesoscopic’ length scale investigated by SCapS from (10 to 100 nm). A quantum mechanical treatment of electron scattering phenomena, based on the interference of incident and reflected electron wave functions by a single scattering center, is required on a length scale of  $\sim 1$  nm, as recently demonstrated in some investigations by scanning tunneling microscopy [23].

### 3.4 Summary

In conclusion, Scanning Capacitance Spectroscopy (SCapS) is used to investigate nanoscale capacitive behavior of graphene deposited on insulating substrates. In particular, we started with analysis of graphene layers deposited on 300 and 100 nm SiO<sub>2</sub> layers grown on  $n^+$  Si. This study revealed that the capacitor effective area ( $A_{eff}$ ) responding to the AC bias applied to the back-gate is much smaller than the geometrical area of the graphene sheet.  $A_{eff}$  increases linearly with the bias (i.e., proportionally to the induced charge density in graphene) and symmetrically for bias inversion. For each bias  $V_g$ , the value of  $A_{eff}$  is related to the minimum area necessary to accommodate the non stationary charges (electrons/holes) induced by the AC bias, according to

the graphene density of states (DOS) at  $V_g$ . Interestingly, decreasing the  $\text{SiO}_2$  thickness from 300 to 100 nm, the slope of the  $A_{eff}$  versus bias curve strongly increases (by a factor of  $\sim 50$ ). The local quantum capacitance  $C_q$  in the contacted graphene region was calculated starting from the screening length (i.e., the radius of the disk with area  $A_{eff}$ ), and the distribution of the values of  $C_q$  for different tip positions was obtained. Finally this method also allowed to determine the lateral variations of the DOS in graphene.

The developed theory was then successfully applied to other graphene / insulator system to understand the effect of dielectric environment on the capacitive behavior in graphene. Particularly, the electrostatic behavior of graphene pertinent to influence of dielectric permittivity of the substrate was investigated by a comparative study of graphene deposited on  $\text{SiO}_2$  - DG- $\text{SiO}_2$  and graphene deposited on Strontium Titanate ( $\text{SrTiO}_3$ )-DG-STO. The  $C_q$  related to the 2DEG in graphene is substantially higher for DG-STO as compared to DG- $\text{SiO}_2$ . The increase in  $C_q$  is due predominantly to the increased effectively biased area in DG-STO. We suggest that this effect is a consequence of better dielectric screening of commonly observed charged impurities, on graphene and/or at the graphene/substrate interface, by the use of high permittivity substrate.

Furthermore, the screening length (defined as the radius of the  $A_{eff}$ ), evaluated by SCapS was shown to be equivalent to the local electron mean free path in graphene. This is a powerful technique, giving access to the local transport properties in graphene with nanometer scale lateral resolution.

The following chapters describe local electrostatic behavior and transport properties in graphene modified by ion irradiation and in graphene epitaxially grown on 4H-SiC(0001).

# References

- [1] S. Luryi, Appl. Phys. Lett., 52, 501 (1988).
- [2] K. S. Novoselov, A. K. Geim, S. V. Morozov, D. Jiang, Y. Zhang, S. V. Dubonos, I. V. Grigorieva, and A. A. Firsov, Science 306, 666 (2004)
- [3] A. K. Geim, K. S. Novoselov, Nat. Mater. 6, 183 (2007)
- [4] K. S. Novoselov, A. K. Geim, S. V. Morozov, D. Jiang, M. I. Katsnelson, I. V. Grigorieva, S. V. Dubonos, A. A. Firsov, Nature 438, 197 (2005)
- [5] Y. Zhang, Y.-W. Tan, H. L. Stormer, P. Kim, P. Nature 438, 201 (2005)
- [6] T. Fang, A. Konar, H. Xing, D. Jena, Appl. Phys. Lett. 91, 092101 (2007)
- [7] M. I. Katsnelson, Phys. Rev. B 74, 201401 (2006)
- [8] J. Fernández-Rossier, J. J. Palacios, L. Brey, Phys. Rev. B 75, 205441 (2007)
- [9] J. Martin, N. Akerman, G. Ulbricht, T. Lohmann, J. H. Smet, K. Von Klitzing, A. Yacobi, Nat. Phys. 4, 144 (2008)
- [10] J. P. Eisenstein, L. N. Pfeiffer, K. W. West, Phys. Rev. B 50, 1760 (1994)
- [11] C. Jang, S. Adam, E. D. Williams, S. Das Sarma and M. Fuhrer, Phys. Rev. Lett. 101, 146805 (2008)
- [12] H. W. Gandy, Phys. Rev. 113, 795, (1959)
- [13] R. C. Neville, B. Hoeneisen and C. A. Mead, J. Appl. Phys. 43, 2124, 1972
- [14] F. Giannazzo, S. Sonde, V. Raineri, G. Patanè, G. Compagnini, F. Aliotta, R. Ponterio, and E. Rimini, Phys. Status Solidi C 7, 1251 (2010)

- [15] S. Sonde, F. Giannazzo, V. Raineri, and E. Rimini, *Phys. Status Solidi B*, 247, 907 (2010)
- [16] F. Giannazzo, S. Sonde, V. Raineri, and E. Rimini, *Appl. Phys. Lett.*, 95, 263109 (2009)
- [17] S. Sonde, F. Giannazzo, C. Vecchio, R. Yakimova, E. Rimini and V. Raineri, *Appl. Phys. Lett.* 97, 132101 (2010)
- [18] S. Das Sarma, S. Adam, E. H. Hwang, and E. Rossi, *arXiv:1003.4731v1* (2010)
- [19] J.H. Chen, C. Jang, S. Xiao, M. Ishigami, M. S. Fuhrer, *Nat. Nanotechnol.* 3, 206 (2008)
- [20] V. M. Pereira, J. M. B. Lopes dos Santos, and A. H. Castro Neto, *Phys. Rev. B* 77, 115109 (2008)
- [21] T. Stauber, N. M. R. Peres, and F. Guinea, *Phys. Rev. B* 76, 205423 (2007)
- [22] E. H. Hwang, S. Adam, and S. DasSarma, *Phys. Rev. Lett.* 98, 186806 (2007)
- [23] G. M. Rutter, J. N. Crain, N. P. Guisinger, T. Li, P. N. First, and J. A. Stroscio, *Science* 317, 219 (2007)

## Chapter 4

# Ion irradiation and defect formation in graphene

### 4.1 Introduction

The study of defects and impurities in single layer and few layers graphene is of crucial importance to understand and predict the behavior of such material. In fact, the intentional/unintentional presence of those defects strongly affects the electronic transport properties of graphene devices [1]. Above and beyond, the controlled introduction of defects in graphene can be used to tailor physical, chemical and mechanical properties [2].

Recently, the effects of electron beam irradiation [3] and plasma treatments [4] on the crystalline order and on the electronic properties of graphene sheets have been investigated. Only few works have been reported on energetic ion irradiation in graphene [5]. However, no explanation on the defect formation on so thin layer (monolayer) by keV ion irradiation has been given. The deposited energy is very low (mainly electronic loss) and the number of vacancies created by direct collisions negligible. Nevertheless, a relevant number of introduced defects is reported. Furthermore, ion irradiation by ion implanters represents the best and widely used way to introduce controlled amount of defects in solids and can be used to locally (by focused ion beams or masking) induce modifications in graphene, such as the transition from  $sp^2$  to  $sp^3$  hybridization controlling locally the graphene/graphane [6] transition and approaching 2D band gap engineering. Ion irradiation of graphene is particularly interesting also because it allows to

understand how the energy released by the single ion at the beginning of the collision cascade is planar distributed on such a single atomic carpet.

For all these reasons we started a series of microscopic and spectroscopic observations of ion irradiated graphene layers by changing both the number of piled-up layers involved in the irradiation and the density of the defects released by the ion beam through a strict control of the radiation fluence. In this work, single layer and few layers of graphene deposited on 100 nm SiO<sub>2</sub> grown on Si were irradiated with 500 keV C<sup>+</sup> ions at fluences ranging from 10<sup>13</sup> to 10<sup>14</sup> cm<sup>-2</sup>. In the works reported to date in literature, low energy (few keV) ions have been used to irradiate graphene deposited on SiO<sub>2</sub>. In that energy regime, the projected range of implanted ions is within few nanometers in the SiO<sub>2</sub>. Hence, structural changes can happen in the SiO<sub>2</sub> surface region and influence the defect release in graphene. In our study, high energy C ions were used, since the projected range is very deep in the substrate below the SiO<sub>2</sub> layer, while the SiO<sub>2</sub> remains almost unaffected by the implantation. Raman spectroscopy and atomic force microscopy (AFM) were jointly applied to study the mechanisms of defect release on single and few layers of graphene and Scanning Capacitance Spectroscopy (SCapS) is used to study the local capacitive and transport properties in defected graphene.

## 4.2 Sample preparation

Few layers of graphene were obtained by micromechanical exfoliation of HOPG and deposited on a Si substrate coated with 100 nm thick oxide. As-prepared samples were implanted with 500 keV C<sup>+</sup> ions at four different fluences: 1×10<sup>13</sup>, 2×10<sup>13</sup>, 5×10<sup>13</sup> and 1×10<sup>14</sup> cm<sup>-2</sup>. Implants were carried out under high vacuum conditions (10<sup>-6</sup> Torr) in order to minimize surface contaminations.

The incident ion beam releases energy to the graphene layer by direct collisions with lattice C atoms and by interaction with electrons in the sheets. For 500 keV C<sup>+</sup> ions incident on a single layer of graphene, the cross section of direct C<sup>+</sup>-C collisions can be estimated as  $\sigma \approx 1 \times 10^{-17}$  cm<sup>2</sup>. This simple estimation is based on the Kinchin-Pease theory of the displacement of atoms in solids by radiation [7] and on recent works on graphite irradiation [8]. Since the density of C atoms in graphene is  $N \approx 4 \times 10^{15}$  cm<sup>-2</sup>, the probability that a direct collision occurs, with the formation of a vacancy, is  $N\sigma \sim 4 \times 10^{-2}$ . Hence, the expected density of vacancies for ion fluences from 1×10<sup>13</sup> to 1×10<sup>14</sup> cm<sup>-2</sup> is ranging from 4×10<sup>11</sup> to 4×10<sup>12</sup> cm<sup>-2</sup>.

Both as prepared and implanted samples were preliminarily inspected by



### 4.3. Raman spectroscopic investigation

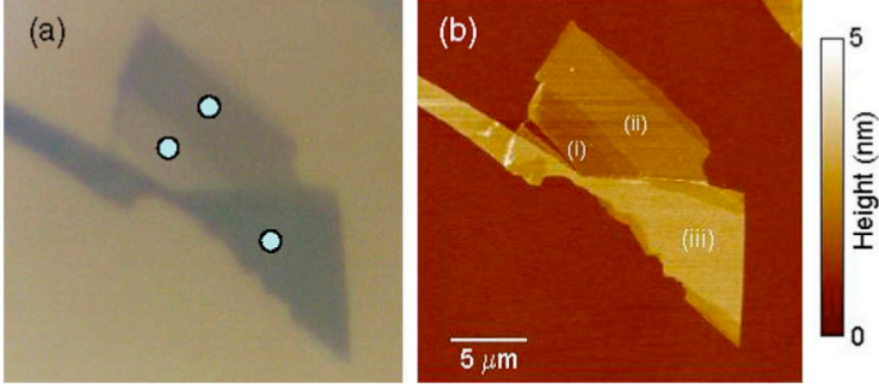


Figure 4.1: Typical optical (a) and AFM (b) images on a sample containing both monolayer (i) bilayer (ii) and multi-layer (iii) regions. The spots on the optical image indicate the spatial resolution of the Raman measurements.

optical microscopy, in order to identify the few layer graphene flakes, and, later, by TappingMode atomic force microscopy. In Figure 4.1, typical AFM and optical images on a graphene sample containing both monolayer (i) bilayer (ii) and multi-layer (iii) regions are reported.

### 4.3 Raman spectroscopic investigation

Raman spectra were measured both on as-prepared and irradiated samples preliminarily identified by AFM. The measurements were performed at room temperature with a Jobin Yvon spectrometer using a 633 nm exciting radiation and a  $3\text{ cm}^{-1}$  resolution. A  $100\times$  objective ensures a lateral resolution close to  $1\text{ }\mu\text{m}$  (see spots on Figure 4.1). Extreme care is taken to avoid sample damage or laser induced heating. Measurements were performed at 1 mW incident power. No significant spectral change was observed in such a configuration. We also measured the reference bulk graphite used to produce the layers.

For a long time Raman spectroscopy has been considered the most powerful spectroscopic technique to study carbon based materials due to the specific response to any change in carbon hybridization state [9, 10] as well as the introduction of defects [11] or foreign species [12]. In the specific case, the effects of ion irradiation on highly oriented graphite samples has been extensively stud-

ied by Dresselhaus et al. more than 20 years ago by Raman spectroscopy [13]. They observed that three regimes of behaviour can be achieved by evaluating the energy deposited into the collision cascade during the ions' slowing down inside the sample. At low fluences the disorder D line located at  $1360\text{ cm}^{-1}$  starts to appear and its intensity grows quite linearly with the ion fluence. In this regime the D peak is sharp and is related with the appearance of pockets of disorder within ordered HOPG. At intermediate fluences the first order Raman peaks start to broaden because of the percolation of single disordered domains (sometimes called microcrystalline regime). At these first two stages, generally, annealing at moderate temperatures is able to restore the primitive order. A final stage can be obtained by further increasing the damage, thus leading to an amorphous carbon sample.

A similar scenario can be assumed to occur also during ion irradiation of single and few layers of graphene deposited on  $\text{SiO}_2$ , even if the threshold fluences between the mentioned three regimes are not exactly known in this case. Of course those threshold values depend on the mass and energy of the irradiating ions. Since for  $\text{C}^+$  ion irradiation at 500 keV, the coalescence of disorder pockets in HOPG (i.e. the transition from the first to the second regime) should occur at fluences higher than  $5 \times 10^{14}\text{ ions/cm}^2$ , we have properly chosen a maximum fluence of  $1 \times 10^{14}\text{ ions/cm}^2$  in our experiment, in order to stay in the first regime. This is obviously the most intriguing one, because the long range integrity of the graphene layer is still maintained, but the introduced defects modify the electronic and mechanical properties of the sheet.

In Figure 4.2 we report the Raman spectra obtained for different ion fluences in a single layer graphene. Beside the already mentioned D line, other three main features are to be considered. Two of them are observed even in the case of defects free graphite (HOPG). They are the G line at  $1580\text{ cm}^{-1}$ , due to the doubly degenerate zone centre  $\text{E}_{2g}$  mode and the  $\text{G}'$  (or 2D) line, appearing in the range  $2600\text{--}2800\text{ cm}^{-1}$  and corresponding to the overtone of the D band. The third signal is considered another defects induced Raman feature, it is frequently termed  $\text{D}'$  line and is located at  $1620\text{ cm}^{-1}$ . The nature and the dispersive behaviour of D,  $\text{D}'$  and  $\text{G}'$  bands have been nicely correlated invoking the so called double resonance Raman process [14], recently applied also to the features observed in single and few layers graphene [15].

The introduction of controlled amount of defects through ion irradiation has notable consequences on most of the above mentioned Raman features for what concerns either the position and the relative intensities. As a first observation, the D line (see the inset of Figure 4.2(a)) rises asymmetric at the lowest fluence and seems to red-shift and increase in width. These effects are specific for

### 4.3. Raman spectroscopic investigation

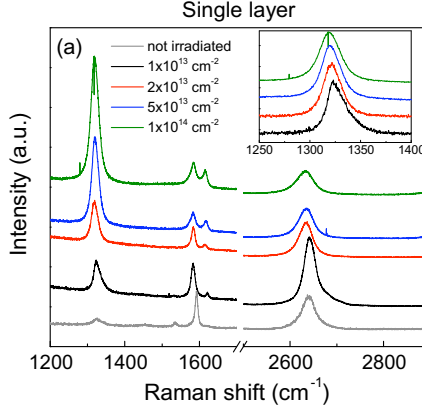


Figure 4.2: Raman spectra on a single layer graphene not irradiated and irradiated with 500 keV C ions at  $1 \times 10^{13}$ ,  $2 \times 10^{13}$ ,  $5 \times 10^{13}$  and  $1 \times 10^{14} \text{ cm}^{-2}$  fluences. In the insert, the D peak for the four fluences is reported (here intensities are normalized).

single layer graphene and have not been reported for three dimensional graphite structures. If one would invoke the double resonance theory the observation of a red-shift could be correlated with a change in the electronic structure of the layer due to the presence of defects or to an increasing strain in the graphene sheet.

Regarding the  $G'$  line we observe two apparently conflicting trends. On one side the intensity of  $G'$  decreases by increasing the ion irradiation fluence with respect to the G line, suggesting an approach to the ‘infinite layers’ condition. On the other hand the second order structure continues to show a quite symmetrical line-shape like that always found in single layer graphene (Figure 4.2(b)), while a redshift consistently scales with the D line behaviour. A proper quantification of the amount of defects in graphite-like materials using Raman spectroscopy has been historically given through the evaluation of the size ( $L_a$ ) of in-plane crystallites formed by a certain number of carbon rings [16] and this has been related to the  $I_D/I_G$  intensity ratio. It is now well established that there is a direct correlation between these two quantities as [11]:

$$L_a = (2.4 \times 10^{-10}) \lambda_{laser}^4 \left( \frac{I_D}{I_G} \right)^{-1} \quad (4.1)$$

here,  $\lambda_{\text{laser}}$  is the laser excitation wavelength expressed in nm as well as  $L_a$ . The original idea behind this was to link the D peak intensity to phonon confinement. Thus, since the G peak is the allowed phonon, the intensity of the not allowed phonon would be ruled by the ‘amount of breaking’ of the selection rule. If this relation, generally observed for nanographites, is considered valid also for a single graphene layers, an irradiation at  $10^{14}$  ions/cm<sup>2</sup> would lead to the formation of graphitic domains of the order of 5 nm, that is few hundreds of fused carbon rings.

It is important to observe that ion irradiation of three dimensional ordered graphite (HOPG) in similar conditions [13] never leads to  $I_D/I_G$  values as high as those given in the spectra reported in Figure 4.2 (up to 7) with such sharp D and G bands. This opens the question whether or not the above mentioned relation could be applied to a single graphene sheet or something peculiar is happening in such a 2D structure. In any case the sharpness of the disorder induced bands shown in Figure 4.2, even for samples with very small crystallite sizes, reveals well-defined boundaries for the crystallites and their narrow size distribution.

The persistence of sharp D and G features can be correlated to the absence of percolation between single disorder domains in such a way to induce a picture in which the presence of different layers is essential for such a percolation behaviour or that there is a direct effect of the underlying SiO<sub>2</sub> substrate.

In order to clarify the role of graphene interaction with the SiO<sub>2</sub> substrate during ion irradiation, TappingMode AFM was used. The possibility to introduce a controlled density of defects in supported graphene sheets without destroying the long range crystalline order allowed also to study how the morphology of the 2D crystal changes to maintain stability in the presence of those defects. It has been demonstrated that the thermodynamic stability of exfoliated graphene from HOPG depends on its peculiar nanoscale corrugation [17]. The rippled shape of the 2D sheets has been proved experimentally both on freestanding graphene and on graphene supported by a substrate [18]. In the latter case it has been shown that, on nanoscale, graphene is only partially conformal to the substrate morphology and exhibits intrinsic ripples. Hence, it is worth investigating how graphene morphology changes with increasing the defect density in the sheet. To this aim, a systematic comparison was carried out between the surface morphologies of single layer graphene and bare SiO<sub>2</sub> both in the not irradiated samples and in the irradiated ones at different fluences. The results are summarized in Figure 4.3, where the AFM images acquired on  $1 \times 1$   $\mu\text{m}$  scan areas on SiO<sub>2</sub> and supported graphene are reported for not irradiated samples and for irradiated ones with ion fluences of  $1 \times 10^{13}$ ,  $5 \times 10^{13}$  and  $1 \times 10^{14}$

### 4.3. Raman spectroscopic investigation

---

$\text{cm}^{-2}$ . While the  $\text{SiO}_2$  surface is unaffected by the high energy (500 keV)  $\text{C}^+$  irradiation, changes in the surface corrugation of graphene are clearly evident, depending on the ion fluence.

To perform a quantitative comparison of this data, the power spectra of the AFM maps were calculated for all the samples and reported in Figure 4.3(a-d). They are obtained performing the Fast Fourier transform (FFT) of each map and plotting the square of the amplitude versus the spatial frequency. The root mean square roughness (RMS) of the surface is defined as the square root of the integral of the power over the considered frequency range. The power spectral analysis allows to distinguish how features of different lateral size on the surface (i.e. different spatial frequency in the power spectra) contribute to the RMS roughness. In Figure 4.3 the power spectra on graphene surface are compared with those on the bare  $\text{SiO}_2$  surface in order to disentangle the graphene corrugation from that of the underlying  $\text{SiO}_2$  substrate. As-deposited graphene weakly adheres on  $\text{SiO}_2$  (with a van der Waals interaction) and its morphology follows only partially that of the substrate, as confirmed by the power spectra in Figure 4.3(a). Power values on graphene are a factor of 2 higher than on  $\text{SiO}_2$  for spatial frequencies between  $0.01$  and  $0.03 \text{ nm}^{-1}$  (i.e. features on graphene with lateral dimensions between 30 and 100 nm are about 1.4 times higher than on  $\text{SiO}_2$ ) and a factor of 4 higher for spatial frequencies lower than  $0.04 \text{ nm}^{-1}$  (i.e. features on graphene with lateral dimensions lower than 25 nm are about 2 times higher than on  $\text{SiO}_2$ ). It is worth noting that, after irradiation with a fluence of  $1 \times 10^{13} \text{ cm}^{-2}$ , the power on graphene is almost a factor of 10 higher than on  $\text{SiO}_2$  in the entire frequency range (see Figure 4.3(b)). It is reasonable that, during irradiation, part of the weak bonds between graphene and the substrate are broken and a larger fraction of graphene surface becomes free-standing with respect to  $\text{SiO}_2$  one. Such an effect has been observed in the literature for high energy proton irradiation of graphene on  $\text{SiO}_2$ , even using very low fluences ( $10^{11} \text{ cm}^{-2}$ ) not causing defects formations (no D peak in the Raman spectra) [19]. The most interesting and new effect observed in this experiment is the decrease in graphene power spectra at fluences higher than  $5 \times 10^{13} \text{ cm}^{-2}$  (see Figure 4.3(c) and (d)). In particular, after irradiation at the highest fluence ( $1 \times 10^{14} \text{ cm}^{-2}$ ), graphene and  $\text{SiO}_2$  power spectra are almost superimposed. This indicates that, increasing the defect density in graphene above a certain threshold, graphene ripples are strongly suppressed and the defected crystal maintains its thermodynamic stability by adapting its shape to that of the substrate.

Figure 4.4 reports differences in the Raman spectra taken after  $10^{14} \text{ ions/cm}^2$  irradiation in a single-, double- and multi-layer graphene. It clearly shows that

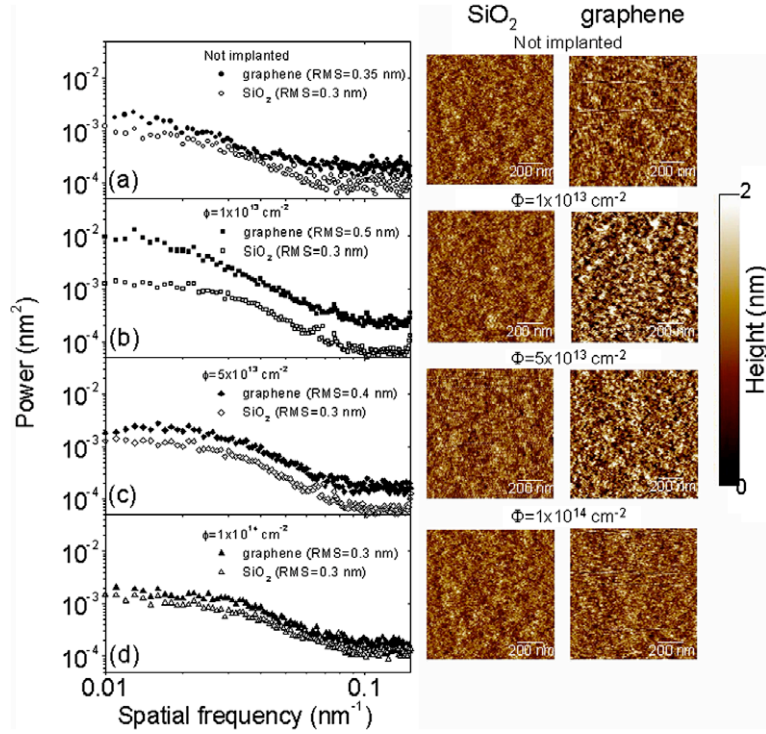


Figure 4.3: AFM images acquired on  $1 \times 1 \mu\text{m}$  scan areas on SiO<sub>2</sub> and supported graphene for not irradiated samples and for irradiated (fluences of  $1 \times 10^{13}$ ,  $5 \times 10^{13}$  and  $1 \times 10^{14} \text{ cm}^{-2}$ ). Power spectra of the AFM maps were calculated for all the samples and reported in a–d.

### 4.3. Raman spectroscopic investigation

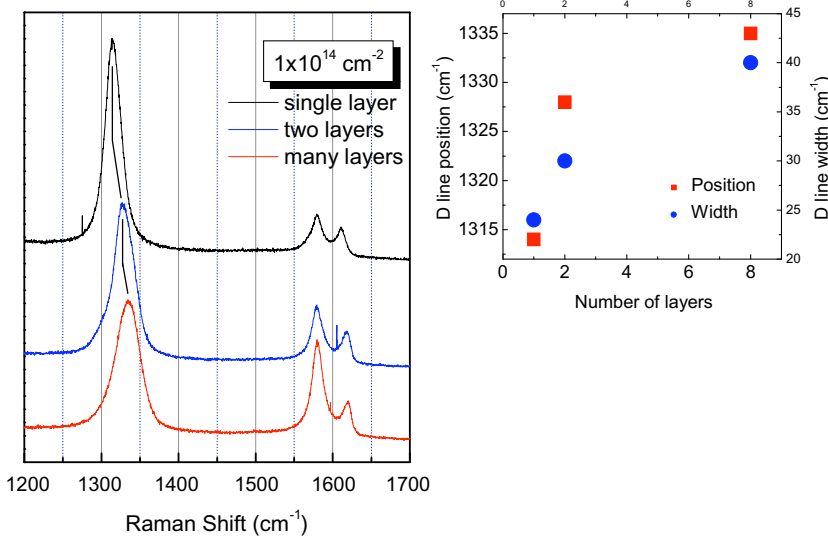


Figure 4.4: Raman spectra taken after  $10^{14} \text{ ion/cm}^2$  irradiation in a single-, double- and multi-layer graphene pieces together with the spectrum of an as prepared single layer graphene

the  $I_D/I_G$  intensity ratio depends on the number of irradiated layers, i.e. it is higher by decreasing the number of layers. This means that the production of defects into a single graphene layer due to ion irradiation is strongly influenced by the presence of one or more underlying planes. This is plausible since in the case of a multi-layer system the same ion, in its collision cascade, induces defects in a very large number of planes around the same spatial region. These defects are free to evolve and interact with each other during the cascade quenching [20]. The same Figure 4.4 reports changes in the D line position and width by changing the number of layers involved, while in Figure 4.5 a correlation between the  $I_D/I_G$  intensity ratio and the ion fluence is given for different layered systems.

In this respect, it is generally agreed that during an ion irradiation process the surface damage occurs on a random basis. Hence, the  $I_D/I_G$  ratio as a function of the ion fluence which can be fitted with functions like:

$$\frac{I_D}{I_G} = \left( \frac{I_D}{I_G} \right)_{sat} (1 - e^{-\eta\varphi}) \quad (4.2)$$

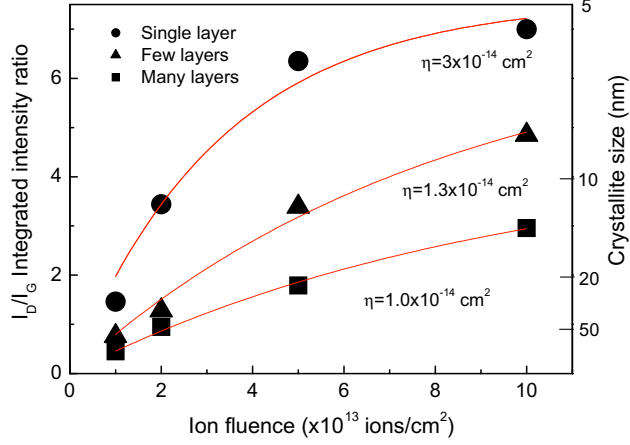


Figure 4.5: Ratio of the D peak and G peak intensities ( $I_D/I_G$ ) as a function of the ion fluence for a single layer, a double layer and a multi-layer of graphene.

where  $(I_D/I_G)_{sat}$  is the ratio at its saturation value and  $\varphi$  is the ion fluence. The parameter  $\eta$  is defined as the disorder release efficiency in the layer, which in single layer graphene ion irradiation is  $\sim 3$  times more efficient in the production of disorder than in multi-layer. A way to interpret these results, in the frame of an interaction between the created defects, is to imagine that for bi- and multi-layer systems a knocked out carbon atom cannot be entirely ejected from the system. Particularly for partial/oblique collisions the atoms could be captured between the layers, allowing them to migrate and heal vacant sites [2].

As a final comment, the obtained results allow also to shade light onto a relevant question regarding the nature of the  $G'$  structure in Raman spectra of graphite related materials. As previously mentioned, there is a general agreement in considering that the evolution of the  $G'$  lineshape by changing the number of layers involved in the probed scattering experiment can be explained with the so called ‘double resonance’ theory which links the phonon wavevectors to the electronic band structure. We have here the possibility to directly compare the D and  $G'$  lines in single as well as double layer graphene possessing controlled amount of defects. For this reason we report in Figure 4.6 the  $G'$  structure for the irradiated ( $10^{13}$  ions/cm<sup>2</sup>) single and double layers together with the signals obtained in the D line region, duplicated in frequency to compare them with the second order signal.



#### 4.4. Nanoscale capacitive behaviour

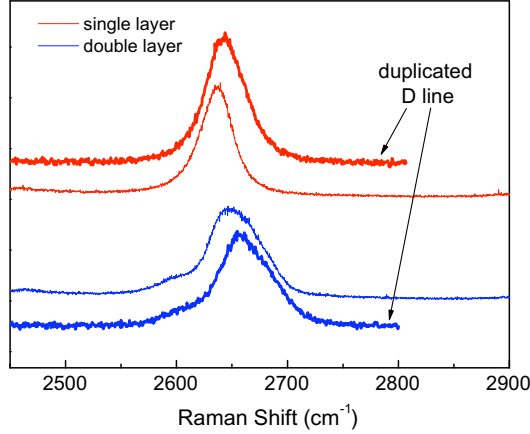


Figure 4.6: G' peak for the irradiated ( $10^{13}$  ions/cm<sup>2</sup>) single and double layers together with the signals obtained in the D line region, duplicated in frequency to compare them with the second order signal.

As a first consideration, we observe a shift between the second order signal and the duplicated one of about  $5\text{ cm}^{-1}$  due to anharmonicity both in the case of single and double graphene layers. This is indeed the first experimental observation of anharmonicity in single and double layer graphenes ever reported. Regarding the single layer, the duplicated D line ( $36\text{ cm}^{-1}$ ) has a width comparable with the respective G' structure ( $40\text{ cm}^{-1}$ ) and can be deconvolved in the same four components as those needed for G'.

After confirming the defect formation in graphene by extensive study with Raman spectroscopy, it would be interesting to employ SPM based methods to examine locally the evolution of electronic properties in graphene after ion irradiation. This is done in the next two sections.

#### 4.4 Nanoscale capacitive behaviour

One of the main consequences of the linear dispersion relation in graphene is the vanishing density of states at small energies around the Dirac point in undoped graphene. This peculiar property makes the 2DEG in graphene very sensitive to impurities and defects [21], as demonstrated in many theoretical [22] as well

as experimental studies. For example, disorder in graphene has been shown to give rise to the unexpected appearance of ferromagnetism in proton irradiated graphene [23, 24, 25, 26, 27, 28]. Recent experiments, carried out on graphene irradiated with  $\text{Ar}^+$  [5], suggest that defects induce changes in the hopping amplitude, which can substantially alter the Fermi velocity. Similarly, key technological parameters like the conductance, transconductance and carrier mobility have been shown to be affected adversely by the increase of defect density in graphene devices [4].

#### 4.4.1 Local Capacitance

In the succeeding discussion we will investigate how capacitance behavior of the graphene samples modifies after irradiation with high energy  $\text{C}^+$  ion beam. This high energy was chosen, to have the projected range of ions is very deep inside the  $\text{n}^+\text{Si}$  substrate. This ensures minimum damage both in the 100 nm  $\text{SiO}_2$  layer and at the interface between  $\text{SiO}_2$  and  $\text{n}^+\text{Si}$ . Samples irradiated with doses of  $1 \times 10^{13}$  and  $1 \times 10^{14} \text{ cm}^{-2}$  were chosen for this study. The capacitive response is then compared with capacitive response of pristine graphene samples (not irradiated graphene samples deposited on  $\text{SiO}_2$ ).

The energy released to graphene by incident  $\text{C}^+$  ions is shared between two different contributions: (i) collisions with the C atoms of graphene lattice (elastic energy loss) and (ii) interaction with electrons (inelastic energy loss). For 500 keV  $\text{C}^+$  ions, only a small fraction of the ion energy is lost by direct  $\text{C}^+\text{-C}$  collisions ( $\sim 0.6 \text{ eV}$ ), whereas most of the energy is lost by the inelastic collisions with electrons in graphene ( $\sim 270 \text{ eV}$ ). This energy is in turn converted into lattice vibrations, i.e. a ‘local heating’ of graphene occurs.

Figure 4.7 shows a set of 25 SCapS curves obtained on a matrix of  $5 \times 5$  different tip positions (with a separation of  $1 \mu\text{m} \times 1 \mu\text{m}$ ) on a pristine graphene sample. The noise affecting each of the curves acquired at different tip positions on non-irradiated  $\text{SiO}_2$  corresponds to the instrumental noise as explained earlier (Section 3.2.1). It is worth noting that it remains the same for the  $\text{SiO}_2$  signal even after irradiation. In Figure 4.7(b) and (c) are shown the SCapS curves obtained on irradiated graphene for the lowest and highest doses. By comparison with the SCapS curves obtained on pristine graphene (see Figure 4.7(a)) a couple of differences can be observed. Capacitance curves obtained on  $\text{SiO}_2$  (dashed lines) are essentially similar in all cases (hence only averaged curves are shown for comparison). This is a confirmation of the fact that the high-energy  $\text{C}^+$  ions go deep inside the substrate, i.e. beyond  $\text{SiO}_2$  and  $\text{SiO}_2/\text{n}^+\text{Si}$  interface, and do not affect the  $\text{SiO}_2/\text{n}^+\text{Si}$  capacitive behaviour. Also the morphological maps

#### 4.4. Nanoscale capacitive behaviour

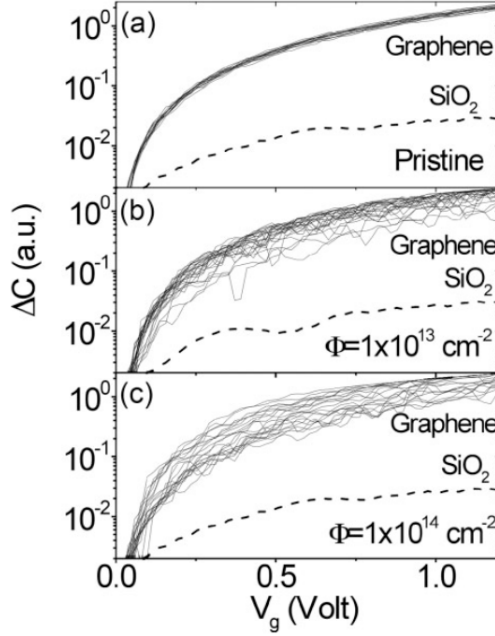


Figure 4.7: SCapS curves obtained on (a) pristine graphene, (b) graphene irradiated with a fluence of  $1 \times 10^{13}$  ions/cm<sup>2</sup>, and (c)  $1 \times 10^{14}$  ions/cm<sup>2</sup>.

on SiO<sub>2</sub> surface before and after irradiation (see Figure 4.3) show negligible changes due to ion bombardment.

The SCapS curves on irradiated graphene exhibit noticeably different behaviour with respect to pristine graphene, showing widely varying signal at different points on the sheet. Since irradiation has only a minor effect on the SiO<sub>2</sub>/n<sup>+</sup>Si MOS capacitance, all the observed changes in the graphene/SiO<sub>2</sub>/n<sup>+</sup>Si capacitive behaviour are due to changes in graphene electronic properties. This widely varying capacitive behaviour is an early indication of the variations in the local electrical properties in graphene due to the irradiation-induced local damage.

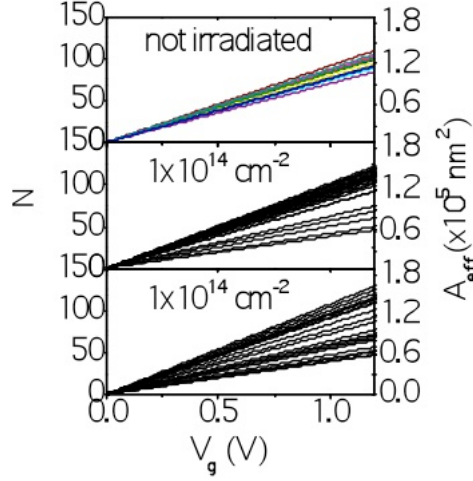


Figure 4.8:  $N$  (left axis) and  $A_{eff}$  (right axis) obtained on (a) pristine graphene, and graphene irradiated with a fluence of (b)  $1 \times 10^{13}$  ions/cm<sup>2</sup> and (c)  $1 \times 10^{14}$  ions/cm<sup>2</sup>.

#### 4.4.2 $A_{eff}$ and Fermi velocity

Following the theory developed in Section 3.2 the ratio  $N = |\Delta C_{gr}| / |\Delta C_{ox}|$  is evaluated and for irradiated and non irradiated cases (Figure 4.8 (left axis)). Similarly, the evolution of  $A_{eff}$  before and after irradiation can also be seen in Figure 4.8 (right axis). Substantially wider variations (beyond experimental error) can be seen for irradiated graphene cases. In order to get more quantitative information on the distributions of the  $N$  values on the graphene sheet for different fluences, in Figure 4.9 the histograms of  $N$  at fixed bias ( $V_g = 1$  V) are reported. Interestingly, in the case of pristine graphene (Figure 4.9(a)), the distribution contains only one peak, which is fitted with a Gaussian distribution (red line). In the case of irradiated graphene, together with that peak, a broad distribution at lower  $N$  values appears. Moreover, the number of counts under the first peak decreases with increasing the fluence, while the number of counts under the broader distribution increases. All of these results indicate that the first peak is associated with not damaged graphene regions contacted by the tip, while the remaining part of the distribution is associated to damaged graphene.

This is an interesting result considering that  $N$  (and in turn  $A_{eff}$ ) gives a

#### 4.4. Nanoscale capacitive behaviour

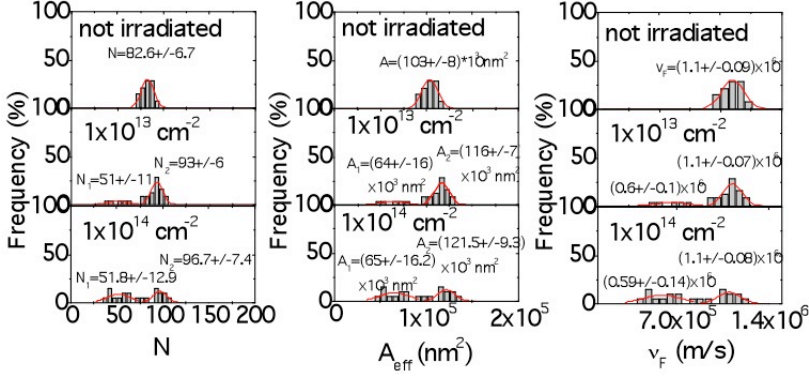


Figure 4.9: Histograms showing quantitative variations for (a)  $N$ , (b)  $A_{eff}$  and (c)  $\nu_F$ . The cases for pristine graphene are depicted in (1), while (2) and (3) indicate the cases for graphene irradiated with a fluence of  $1 \times 10^{13} \text{ cm}^{-2}$  and  $1 \times 10^{14} \text{ cm}^{-2}$  respectively. The two distributions observed distinctly indicate probed sites that are defected and non-defected, especially, the broader distribution at lower values are associated with defected sites.

direct access to the local density of states, which can further be related to the transport parameters like the local Fermi velocity and the carrier mobility. This is discussed in the following:

The density of states (DOS) is inversely proportional to the evaluated  $A_{eff}$  by the relation  $\text{DOS} = C_q / (qA_{eff})$ . Interestingly,  $\text{DOS}(V_g) \sim \frac{1}{\nu_F}$  as follows: The DOS in graphene is given as (refer to the discussion in Section 1.5.2),

$$D(E) = \frac{2A_c}{\pi} \frac{|E|}{\nu_F^2} \quad (4.3)$$

Considering the Fermi wavevector  $k = \sqrt{\pi n}$  ( $n$  is the carrier density), the linear dispersion relation in graphene can be written as,

$$E = \hbar \nu_F \sqrt{\pi n} \quad (4.4)$$

However, taking into account the capacitive coupling between graphene and the underlying Si gate,  $n = \frac{C'_{ox} V_g}{q}$ . So,

$$D(V_g) = \frac{2A_c\hbar}{\nu_F} \sqrt{\pi \frac{C'_{ox} V_g}{q}} \quad (4.5)$$

This implies that the quantitative variations seen in the  $A_{eff}$  can be related to the variations in  $\nu_F$ . This is done in Figure 4.9(c), where for the pristine graphene case, the  $\nu_F$  on average is  $1.1 \times 10^6$  m/s. Accordingly, the  $A_{eff}$  variations observed around the defected sites in graphene are due to lower evaluated  $\nu_F$ . In this particular case, we evaluated  $\nu_F$  to be 60% of the one in pristine graphene, around the defected sites in irradiated graphene.

Finally, using the raw data in Figure 4.7, evaluated DOS and  $C'_q$  are reported in Figure 4.10. A broader distribution observed in Figure 4.10 (e,f) is associated to the probed defected sites. As a last comment, the two distinct distributions observed, are a testimony to the capability of SPM based method to locally probe the random defects created by ion irradiation and would be an essential tool in evaluating local the transport properties in graphene. This is addressed in the next section.

## 4.5 Local electron mean free path and mobility

In this section the method explained in Section 3.3 is applied to probe the lateral inhomogeneity in local transport properties both on pristine graphene samples obtained by mechanical exfoliation of HOPG and on samples subjected to ion irradiation at fluences mentioned in the previous sections. Recently, ion irradiation has been used as a mean to tailor graphene transport properties by artificially modifying the defects density [29, 30]. Only Raman measurements (as discussed in the previous section) [29] and electrical measurements on macroscopic test structures [30] have been reported to date but no information on the ‘local’ changes of mobility after irradiation is available.

In our experiment the projected range of the implanted ions is  $1 \mu\text{m}$  from the surface, i. e. quite deep into the Si substrate. This minimizes the damage both in the  $\text{SiO}_2$  layer and at its interface with Si. Ion fluences ranging from  $1 \times 10^{13}$  to  $1 \times 10^{14} \text{ cm}^{-2}$  were adopted. SCapS allowed to study locally the effects of the irradiated fluence on  $l$  and  $\mu$ .

In Figure 4.11(a), typical capacitance characteristics measured on an array of positions with interstep interval of  $1 \times 1 \mu\text{m}^2$  on a pristine graphene exfoliated and deposited on  $\text{SiO}_2$  is reported. Figures 4.11(b) and 4.11(c) illustrate the characteristics on irradiated graphene with fluences of  $1 \times 10^{13}$  and  $1 \times 10^{14} \text{ cm}^{-2}$ ,

#### 4.5. Local electron mean free path and mobility

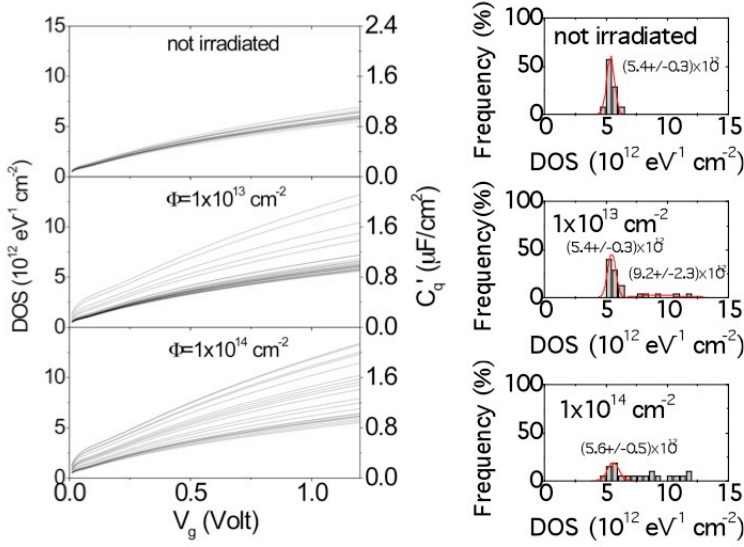


Figure 4.10: Density of states (left axis) and quantum capacitance per unit area (right axis) obtained on (a) pristine graphene, (b) graphene irradiated with a fluence of  $1 \times 10^{13}$  ions/cm<sup>2</sup> and (c) a fluence of  $1 \times 10^{14}$  ions/cm<sup>2</sup>. Distributions of DOS at fixed backgate bias ( $V_g=1$  V) for (d) pristine graphene and graphene irradiated with fluences of (e)  $1 \times 10^{13}$  ions/cm<sup>2</sup> and (f)  $1 \times 10^{14}$  ions/cm<sup>2</sup>.

respectively.

The local  $|\Delta C|$  versus  $V_g$  curves on non irradiated graphene samples show different characteristics. This has been discussed extensively in Section 4.4. To represent quantitatively the observed spread in capacitance characteristics, the histograms of the local C values measured at fixed gate bias  $V_g = 1$  V are reported in Figure 4.11(d) for the not irradiated graphene and in Figures 4.11(e) and 4.11(f) for irradiated graphene with the lowest and highest fluence, respectively. The  $|\Delta C|$  distribution for not irradiated graphene in Figure 4.11(d) can be fitted by a single Gaussian. The distributions in irradiated graphene exhibit two distinct peaks, a first one  $|\Delta C_1|$  at a similar  $|\Delta C|$  value and with similar FWHM as in the not irradiated graphene, and a second one at lower  $|\Delta C|$  values,  $|\Delta C_2|$  and with larger FWHM. In Figure 4.11(g), the percentage of counts under the peak 1 and under the peak 2 are reported versus fluence. The area under the peak 2 increases linearly with the fluence, whereas that under the peak 1 decreases. All of these observations indicate that the peak 1 in Figures 4.11(e) and 4.11(f) is associated to graphene regions not locally affected by irradiation, whereas the peak 2 is associated to regions with modified properties. In particular, the possibility to observe the peak 1 in irradiated graphene indicates that the defects responsible of this effect are discretely and randomly distributed on the sheet and their density is low enough to allow the sampling of defect-free areas by an AFM tip with 5 nm contact radius.

In Figure 4.12(a) we report the local  $l$  versus  $\sqrt{V_g}$  curves extracted from the  $|\Delta C_{gr}| - V_g$  characteristics on not irradiated graphene, whereas in Figures 4.12(b) and 4.12(c),  $l$  for irradiated graphene with the lowest and highest fluences are reported.  $l$  is reported also versus  $\sqrt{n}$  (upper scale).

The dependence of the electron mean free path on the carrier density in graphene has been discussed in details [31, 32] considering the main scattering mechanisms, i.e., coulomb scattering by charged impurities, scattering by phonons and scattering by point defects, e.g., vacancies. While the electron mean free path limited by charged impurities and vacancies scattering is expected to increase as  $\sqrt{n}$ , the mean free path limited by scattering with phonons is expected to decrease as  $1/n$  [31]. The obtained results clearly show the increase of  $l$  with  $\sqrt{n}$ , indicating that the main scattering sources are charged impurities and/or vacancies. In not irradiated graphene, the vacancy contribution can be neglected and the main mechanism limiting  $l$  is represented by the charged impurities scattering. These impurities are either adsorbed on graphene surface or located at the interface with the  $\text{SiO}_2$  substrate. Their random spatial distribution is responsible for the observed spread in the local values of  $l$



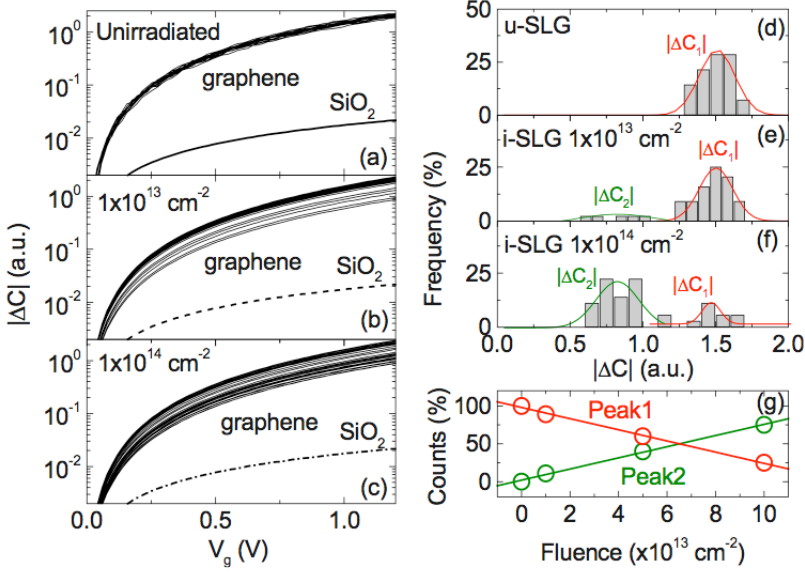


Figure 4.11:  $|\Delta C|$  vs  $V_g$  measurements on arrays of several tip positions on (a) not irradiated graphene, and on irradiated graphene at fluences (b)  $1 \times 10^{13}$ , and (c)  $1 \times 10^{14} \text{ cm}^{-2}$ , respectively. Curves measured with the tip on  $\text{SiO}_2$  reported for comparison. Histograms of the capacitance values at  $V_g = 1 \text{ V}$  for (d) not irradiated graphene, and irradiated graphene at (e)  $1 \times 10^{13}$ , and (f)  $1 \times 10^{14} \text{ cm}^{-2}$ . (g) Percentage of counts under peaks 1 and 2 in the distributions vs the irradiated fluence.

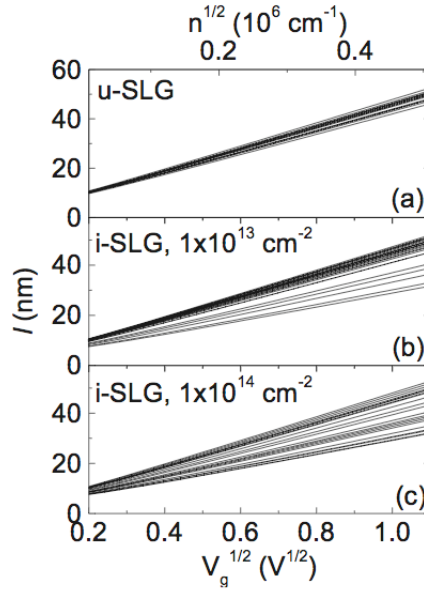


Figure 4.12: Local electron mean free path vs  $V_g^{1/2}$  and  $n^{1/2}$  for several tip positions on (a) not irradiated graphene and on irradiated graphene at fluences (b)  $1 \times 10^{13}$ , and (c)  $1 \times 10^{14} \text{ cm}^{-2}$ .

## 4.6. Summary

---

on not irradiated graphene. On irradiated graphene, the scattering with point defects plays a significant role and it is responsible for reduction of  $l$  for some probed positions. It is worth noting that the number of probed SLG positions with reduced  $l$  increases with the fluence. Finally, from Equation 3.14, the local mobility can be obtained from the local mean free path.

$\mu$  is reported versus  $V_g$  and  $n$  both for not irradiated graphene (Figure 4.13(a) and irradiated graphene (Figure 4.13(b) and 4.13(c)). It is worth noting that, except for very low carrier densities, results almost independent on  $n$ . To better quantify its lateral spread on the graphene sheet, the histograms at  $V_g = 1$  V on not irradiated and irradiated graphene are also reported in Figure 4.13. The corresponding  $l$  values are also indicated (upper scale). For not irradiated graphene the distribution exhibits a single peak at  $\mu=8200$   $\text{cm}^2\text{V}^{-1}\text{s}^{-1}$  with FWHM  $180$   $\text{cm}^2$   $\text{V}^{-1}\text{s}^{-1}$ . The spread is associated to the distribution of charged impurities on not irradiated graphene. This value of  $\mu$  is comparable to the typically reported mobility values at room temperature,  $\sim 10^4$   $\text{cm}^2$   $\text{V}^{-1}$   $\text{s}^{-1}$ , determined by sheet resistance and/or Hall effect measurements on graphene exfoliated from HOPG and deposited on  $\text{SiO}_2$  [1] or on other substrates [34]. A Hall mobility  $\sim 0.6 \times 10^4$   $\text{cm}^2$   $\text{V}^{-1}$   $\text{s}^{-1}$  has been reported for epitaxial graphene grown on the Si face of SiC [35]. In irradiated graphene, in addition to a narrow peak at  $\mu=8200$   $\text{cm}^2\text{V}^{-1}$   $\text{s}^{-1}$  associated to the defect-free sample regions, a broader distribution extending from  $\sim 5000$  to  $7500$  and centered around  $\mu=6200$   $\text{cm}^2\text{V}^{-1}$   $\text{s}^{-1}$  is obtained. It is worth noting that the distribution of the number of counts under this part increases with the fluence.

## 4.6 Summary

In summary, we performed ion irradiation by 500 keV  $\text{C}^+$  ions to introduce defects into graphene sheets deposited on  $\text{SiO}_2$  in a controlled way. The combined use of Raman spectroscopy and atomic force microscopy (AFM) allowed to clarify the mechanisms of disorder formation in single layers, bilayers and multi-layers of graphene. The ratio between the D and G peak intensities in single layers are higher than on bilayers and multi-layers, indicating a higher amount of disorder. This cannot be ascribed to point defects, originating from direct  $\text{C}^+-\text{C}$  collisions, but is due to the different interaction between single layers and few layers with the substrate, as demonstrated by AFM analyses. In particular, for irradiation at fluences higher than  $5 \times 10^{13}$   $\text{cm}^{-2}$ , graphene ripples are strongly suppressed and the defected crystal maintains its thermodynamic stability by adapting its shape to that of the substrate.

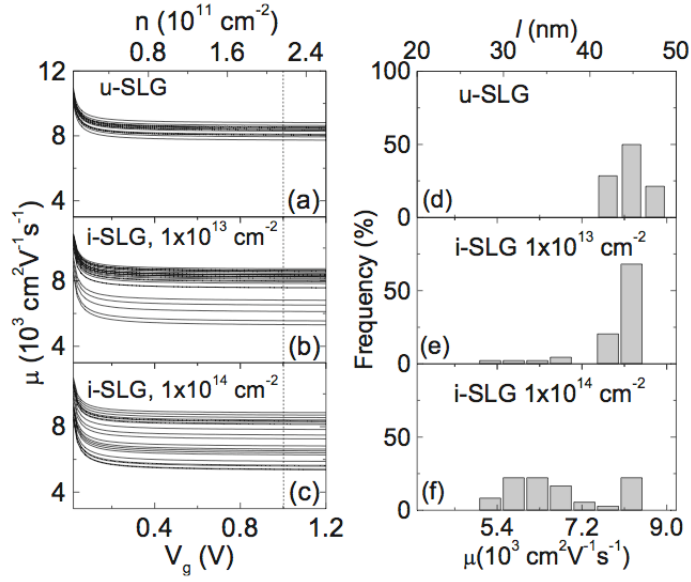


Figure 4.13: Local mobility vs  $V_g$  and  $n$  for several tip positions on (a) not irradiated graphene, and on irradiated graphene at fluences (b)  $1 \times 10^{13}$ , and (c)  $1 \times 10^{14} \text{ cm}^{-2}$ . Histograms of  $\mu$  and  $l$  at  $V_g = 1 \text{ V}$  on (d) not irradiated graphene and (e,f) on irradiated graphene with the two fluences.

#### 4.6. Summary

---

Furthermore, local capacitance measurements allowed getting information on the changes in the electronic properties of graphene due to defects. In particular, the quantitative variations in  $A_{eff}$  are correlated with the variations in quantum capacitance, Fermi velocity. In particular, an increase of the quantum capacitance per unit area, and lowering of Fermi velocity is associated to the damaged regions.

Finally, we probed the local values of the electron mean free path and mobility both on not irradiated and irradiated graphene. The small spread between the local values in not irradiated graphene is due to the inhomogeneous distribution of charged impurities on the surface of graphene and/or at the interface with  $\text{SiO}_2$ . For irradiated graphene a broader distribution of the values was obtained from 5000 to 8500  $\text{cm}^2 \text{V}^{-1} \text{s}^{-1}$  with the lower values corresponding to the locally damaged regions.



# References

- [1] J.H. Chen, C. Jang, S. Xiao, M. Ishigami, M. S. Fuhrer, Nat. Nanotechnol. 3, 206 (2008)
- [2] A. V. Krasheninnikov, F. Banhart, Nat. Mater. 6, 723 (2007)
- [3] D. Teweldebrhan, A. A. Balandin, Appl. Phys. Lett. 94, 013101 (2009)
- [4] K. Kim, H. J. Park, B. C. Woo, K. J. Kim, G. T. Kim, W. S. Yun, Nano Lett. 8, 3092 (2008)
- [5] L. Tapasztó, G. Dobrik, P. Nemes-Incze, G. Vertesy, P. Lambii, L. P. Biró, Phys. Rev. B 78, 233407 (2008)
- [6] D. C. Elias, R. R. Nair, T. M. G. Mohiuddin, S. V. Morozov, P. Blake, M. P. Halsall, et al., Science 323, 610 (2009)
- [7] G. H. Kinchin, R. S. Pease, Rep. Prog. Phys. 18, 1, (1955)
- [8] K. Nakamura, M. Kitajima, Phys. Rev. B 45, 78 (1992)
- [9] V. Scuderi, S. Scalese, S. Bagiante, G. Compagnini, L. D’Urso, V. Privitera, Carbon 47, 2134 (2009)
- [10] L. D’Urso, G. Compagnini, O. Puglisi, Carbon 44, 2093 (2006)
- [11] M. A. Pimenta, G. Dresselhaus, M. S. Dresselhaus, L. G. Cancado, A. Jorio, R. Saito, Phys. Chem. Chem. Phys. 9,1276 (2007)
- [12] L. Calcagno, G. Compagnini, G. Foti, M. G. Grimaldi, P. Musumeci, Nucl. Instrum. Methods B120, 121 (1996)

- [13] B. S. Elman, M. S. Dresselhaus, G. Dresselhaus, E. W. Mby, H. Mazurek, Phys. Rev. B 24, 1027 (1981)
- [14] R. Saito, A. Jorio, A. G. Souza Filho, G. Dresselhaus, M. S. Dresselhaus, M. A. Pimenta, Phys. Rev. Lett. 88, 027401, (2002)
- [15] A. C. Ferrari, J. C. Meyer, V. Scardaci, C. Casiraghi, M. Lazzeri, F. Mauri, et al., Phys. Rev. Lett. 97, 187401 (2006)
- [16] F. Tuinstra, J. L. Koenig, J. Phys. Chem. 53, 1126 (1970)
- [17] J. C. Meyer, A. K. Geim, M. I. Katsnelson, K. S. Novoselov, T. J. Booth, S. Roth, Nature 446, 60 (2007)
- [18] V. Geringer, M. Liebmann, T. Echtermeyer, S. Runte, M. Schmidt, R. Ruckamp, et al., Phys. Rev. Lett. 102, 076102 (2009)
- [19] E. Stolyarova, D. Stolyarov, K. Bolotin, S. Ryu, L. Liu, K. T. Rim, et al. Nano Lett. 9, 332 (2009)
- [20] C. P. Ewels, R. H. Telling, A. A. El-Barbary, M. I. Heggie, P. R. Briddon, Phys. Rev. Lett. 91, 025505 (2003)
- [21] V. M. Pereira, J. M. B. Lopes dos Santos, and A. H. Castro Neto, Phys. Rev. B 77, 115109 (2008)
- [22] N. M. R. Peres, F. Guinea, and A. H. Castro Neto, Phys. Rev. B 73, 125411 (2006)
- [23] Y. Kopelevich, P. Esquinazi, J. H. S. Torres, and S. Moehlecke, J. Low Temp. Phys. 119, 691 (2000)
- [24] P. Esquinazi, A. Setzer, R. Höhne, C. Semmelhack, Y. Kopelevich, D. Spemann, T. Butz, B. Kohlstrunk, and M. Lösche, Phys. Rev. B 66, 024429 (2002)
- [25] S. Moehlecke, P.-C. Ho, and M. B. Maple, Philos. Mag. Lett. 82, 1335 (2002)
- [26] H. Kempa, H. C. Semmelhack, P. Esquinazi, and Y. Kopelevich, Solid State Commun. 125, 1 (2003)
- [27] P. Esquinazi, D. Spemann, R. Höhne, A. Setzer, K.-H. Han, and T. Butz, Phys. Rev. Lett. 91, 227201 (2003)



## REFERENCES

---

- [28] T. Makarova and F. Palacio, Carbon-Based Magnetism: An Overview of Metal Free Carbon Based Compounds and Materials (Elsevier, Amsterdam, 2005)
- [29] G. Compagnini, F. Giannazzo, S. Sonde, V. Raineri, and E. Rimini, Carbon 47, 3201 (2009)
- [30] J.-H. Chen, W. Cullen, C. Jang, M. Fuhrer, and E. Williams, Phys. Rev. Lett. 102, 236805 (2009)
- [31] T. Stauber, N. M. R. Peres, and F. Guinea, Phys. Rev. B 76, 205423 (2007)
- [32] E. H. Hwang, S. Adam, and S. DasSarma, Phys. Rev. Lett. 98, 186806 (2007)
- [33] G. M. Rutter, J. N. Crain, N. P. Guisinger, T. Li, P. N. First, and J. A. Stroscio, Science 317, 219 (2007)
- [34] L. A. Ponomarenko, R. Yang, T. M. Mohiuddin, M. I. Katsnelson, K. S. Novoselov, S. V. Morozov, A. A. Zhukov, F. Schedin, E. W. Hill, and A. K. Geim, Phys. Rev. Lett. 102, 206603 (2009)
- [35] J. L. Tedesco, B. L. VanMil, R. L. Myers-Ward, J. M. McCrate, S. A. Kitt, P. M. Campbell, G. G. Jernigan, J. C. Culbertson, C. R. Eddy, Jr., and D. K. Gaskill, Appl. Phys. Lett. 95, 122102 (2009)



## Chapter 5

# Local electrical properties of graphene/SiC(0001)

### 5.1 Introduction

The prospects of ballistic nanometer-scale electronic devices in graphene have long been supported by mechanical exfoliation of HOPG, which is the easiest and quickest method to obtain graphene. However, since the early developments it was identified that for graphene to be incorporated into current semiconductor technology one of the challenges was to be able to produce uniform films of large area. Ultrathin graphitic layers, EG, obtained by thermal decomposition of surface layers of hexagonal silicon carbide (SiC) showed a lot of promise in this respect [1]. EG offers a favorable way to grow graphene for a practical and scalable approach towards graphene-based electronics, owing to the fact that graphene films can be grown on semi-insulating substrate without any need to transfer (as is the case with CVD graphene on metal substrates) [2]). In this regard parallel research efforts are being focused to grow and investigate graphene on Silicon and Carbon rich faces of SiC [3].

EG is obtained from high-temperature thermal treatments performed either in ultrahigh vacuum or in standard secondary vacuum or even at atmospheric pressure in an inert gas atmosphere. Both the (0001) Si and (000-1) C faces of hexagonal SiC polytypes (4H and 6H) have been experimented with. However, more importantly, large differences have been found in the structural and electronic properties of EG grown on the two faces. In particular, on the (0001) face

of SiC, both experimental and theoretical studies [4, 5, 6] have shown that EG synthesis occurs through a series of complex surface reconstructions. This starts with an initial (Si-rich)  $(\sqrt{3} \times \sqrt{3})R30^\circ$  phase which rapidly converts into a second (C-rich)  $(6\sqrt{3} \times 6\sqrt{3})R30^\circ$  reconstruction when the temperature increases. This is not yet a real graphene layer but, simply, an intermediate (buried) buffer layer (C rich) with a large percentage of  $sp^2$  hybridization (see Figure 5.1 (a)) [7]. This buffer layer, which may be more or less defective with more or less Si dangling bonds at the interface, has a strong influence on the electronic properties of EG on (0001) SiC. Nevertheless, the electron spectrum of epitaxial graphene does not seem to be affected by the interaction with the substrate. On the other hand, graphene exfoliated-and-deposited on substrates offers structurally and electrically clean interface between graphene and SiC with, essentially, only the van der Waals interaction holding the graphene films on the substrate. The interface of such deposited films is depicted in Figure 5.1(b) and (c).

Since the electrons are confined to a single atomic layer in graphene, it is imperative to investigate the effect of the surrounding environment, especially, graphene/substrate related issues on the charge dynamics in the 2DEG. In particular, since it strongly affects the mobility of carriers, the properties of the interface between EG and this buffer layer should be experimentally investigated and compared with the properties of mechanically exfoliated and deposited graphene (DG), where—in principle—the buffer layer does not play any role. This is done in this work.

In the succeeding sections, we will first investigate the electrical properties of graphene/SiC interface by nanoscale current transport through the interface. Then, the effect of interface related issues on the local electrostatic properties and various contributions to the charge scattering at the interface is investigated and evaluated to understand the role of interface for individual cases of EG, DG on SiC and DG on  $SiO_2$ .

## 5.2 Electrical properties of the graphene / 4H-SiC(0001) interface

This section describes the local investigations of the graphene/4H-SiC(0001) interface properties by measuring with a nanoscale lateral resolution the current flowing across the interface using SPM [8, 9]. The Schottky barrier height (SBH), defined as the energy separation between the Fermi level of graphene and the edge of the majority-carrier band of SiC, is locally determined and the

## 5.2. Electrical properties of the graphene / 4H-SiC(0001) interface

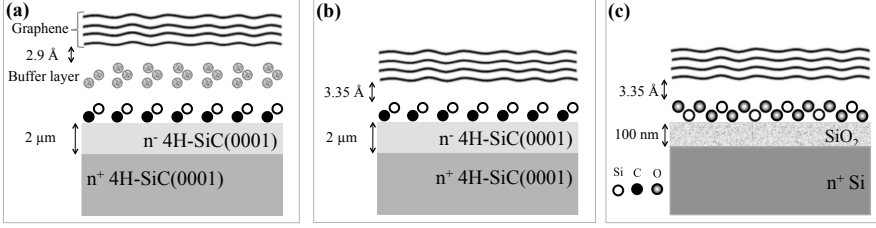


Figure 5.1: Schematic representation of graphene/substrate interface for (a) graphene grown epitaxially on 4H-SiC(0001) (EG), (b) graphene exfoliated and deposited on 4H-SiC(0001) (DG-SiC), and (c) graphene exfoliated and deposited on SiO<sub>2</sub> (DG-SiO<sub>2</sub>). Commonly observed buffer layer between the last SiC bilayer and first graphene layer at the interface in EG is depicted in (a). Such buffer layer is absent in DG-SiC and DG-SiO<sub>2</sub>.

SBH values measured on EG/4H-SiC are compared with those measured on DG on 4H-SiC (0001), in which no buffer layer is present.

The starting material (Figure 5.1(a)) was an n<sup>+</sup> doped (0001) 4H-SiC substrate, 8° off axis, with a 2-μm-thick weakly doped (n<sup>-</sup>) epitaxial layer on top. EG growth was carried out in an inductively heated reactor, as explained in Section 2.3.2. A piece of the same 4H-SiC wafer (not subjected to annealing) was used as the substrate for exfoliated graphene (Figure 5.1(b)). DG on SiC was first identified by optical microscopy. Then, TR-CAFM was used to measure, simultaneously, topographic and current maps on the sample surface.

### 5.2.1 Current transport across graphene/SiC interface

Figure 5.2(a) shows a TR-CAFM current map taken on DG-SiC. The tip bias was 1 V. A very good correlation with the morphological map (not reported) was found, with the brighter portions in the current map (region carrying a higher current corresponding to graphene in the morphological map). After identifying the SiC regions coated with DG, local I-V measurements were carried out by SCurS. The conductive tip is placed on a discrete array of positions on the sample surface noninvasively, lifting the tip by 20 nm at every interval. At every tip position, a current-voltage (I-V) characteristic is recorded. It must be noted that a swift transition between TR-CAFM and SCurS is possible without altering the sample position. The representative positions of the tip during the SCurS scan are depicted in Figure 5.1(a) and the recorded I-V curves are shown

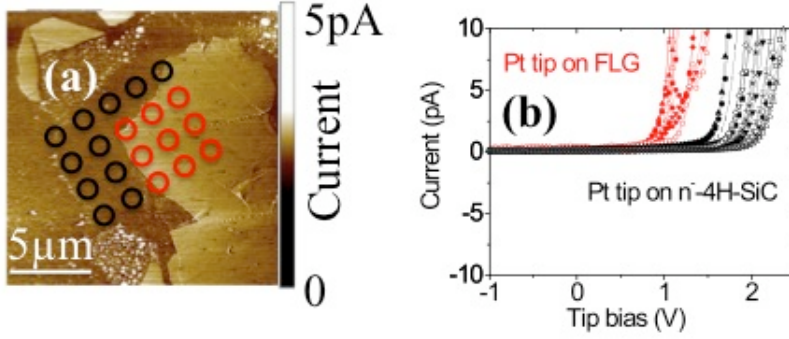


Figure 5.2: (a) Current map of DG on 4H-SiC(0001) at tip voltage of 1 V. The tip positions on graphene and on 4H-SiC are shown. (b) Typical set of SCurS I-V characteristics. Two distinct families of curves are associated with the tip positions on graphene and on 4H-SiC are indicated.

in Figure 5.1(b).

All I-V curves exhibit a rectifying behavior, with a low leakage current under reverse bias and a sudden increase in the current for positive bias beyond a certain threshold voltage. It is worth noting that the acquired curves can be divided in two groups, (i) corresponding to the tip positions on DG and (ii) corresponding to the tip positions on bare SiC substrate. It is clear that DG forms a Schottky contact on top of the 4H-SiC layer.

Before examining EG for vertical current transport, Raman measurements were done to estimate the number of graphene monolayers (MLs) at different spot positions. Spectra collected at different spot positions on the sample surface are shown in Figure 5.3 along with a reference spectrum acquired on the 4H-SiC surface of the untreated sample. All Raman spectra collected on the graphitized sample surface show the characteristic 2D and G peaks, which confirm the presence of graphene, with the latter superimposed to the background signal associated with the substrate. Notice that the graphene fingerprint varies from spot to spot position. This is because, on such off-axis samples, the growth is still far from being optimized and the Raman spectra evidence a nonuniform coverage, with EG thickness varying rapidly at the micrometer scale. After the correction for the background signal, the number of (local) graphene MLs was

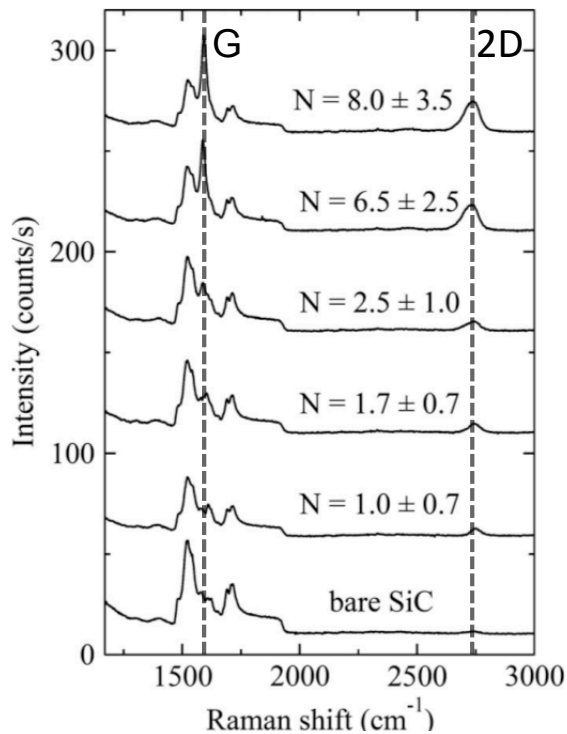


Figure 5.3: MicroRaman spectra collected on several positions on the epitaxial graphene grown on 4H-SiC(0001) substrate along with the spectrum collected on starting substrate (bare SiC) is also shown for comparison. The number of graphene layers was found to vary rapidly at micrometer scale. The estimated number of layers are depicted on each spectrum.

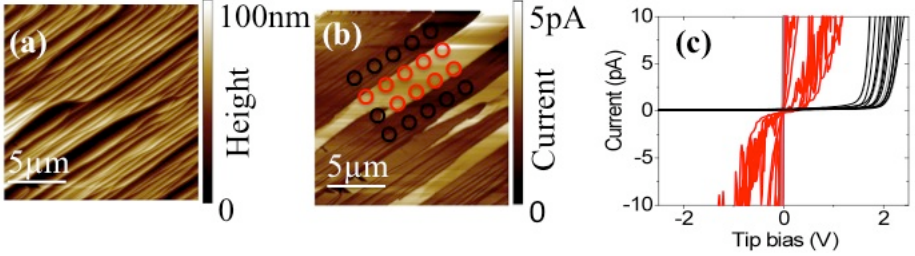


Figure 5.4: (a) Topography and (b) corresponding current map of EG on 4H-SiC(0001). The tip positions on regions covered by EG and on regions devoid of EG are indicated. The corresponding I-V curves are reported in (c).

estimated [10] with average values varying from 1 (or slightly less than 1) to 8 MLs. It must be noted that, at the micrometer scale, no region was found without any graphene sheet on top. Of course, since the Raman values are average coverage over the spot area, a ML thickness lower than 1 ML simply means incomplete graphene coverage.

To get more local information on the graphene coverage, with higher (sub-micrometer) resolution, TR-CAFM scans were performed at different tip positions on EG. Figure 5.4 shows a representative TR-CAFM current map (Figure 5.4(b)) along with the morphology collected on EG (Figure 5.5(a)). Evidently, the surface has large corrugations with a measured roughness of 16 nm, which is significantly higher than the 0.3 nm roughness of the pristine 4H-SiC substrate. This comes from the large step-bunching phenomenon commonly observed on off-axis SiC substrates after high-temperature annealing ( $T > 1400$  °C). ML graphene grows on the SiC surface following these steps. By comparing the morphology and current maps, bright regions carrying homogeneous current in the current map appear evident. A comparison with the results obtained on DG suggests that these high current carrying areas are covered by a few MLs of graphene.

To further analyze the interface current transport, we performed SCurS and collected I-V characteristics in the same sample region. The results are shown in Figure 5.4(c). Again, similar to the sample with DG, the I-V curves on the sample with EG can be divided into two distinct families: the curves acquired on an area covered with graphene and those acquired on an area free of graphene. The I-V characteristics on the graphene-free regions remained similar to those



## 5.2. Electrical properties of the graphene / 4H-SiC(0001) interface

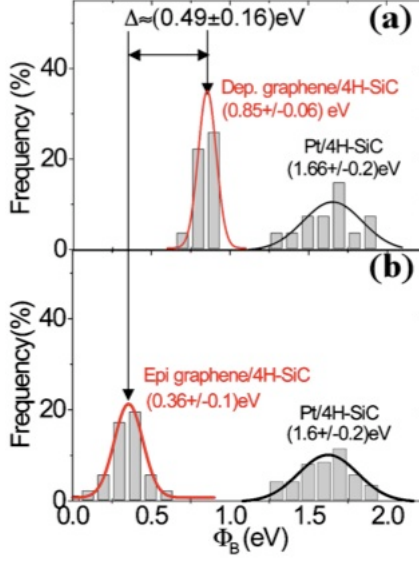


Figure 5.5: Histograms of SBHs evaluated for Pt/graphene/4H-SiC and Pt/4H-SiC in the cases of (a) DG and (b) EG.

measured on the bare 4H-SiC surface in the sample not subjected to thermal treatment (see Figure 5.2(b)). On the other hand, the curves obtained on the regions coated with EG show completely different I-V characteristics. The leakage current is now very large with, in some cases, a clear Ohmic behavior. This is a direct evidence that the SBH at the EG/4H-SiC interface has been reduced with respect to DG/4H-SiC with, in some cases, a possibility of direct tunnel injection. These modified SBH (mSBH) values (due to the presence of graphene on SiC) have been evaluated for each of the I-V curves in Figures 5.2(b) and 5.4(c), using the procedure of refs. [8, 9]. The histograms of the corresponding values have been reported in Figures 5.5(a) and 5.5(b), respectively.

### 5.2.2 Modified Schottky barrier height

While the SBHs for Pt-tip/4H-SiC remain similar for both samples, the average mSBH value for EG on 4H-SiC appears very much reduced ( $\Phi_{EG}=0.36\pm0.1$  eV) with respect to DG ( $\Phi_{DG}=0.85\pm0.06$  eV). This fact is especially interesting

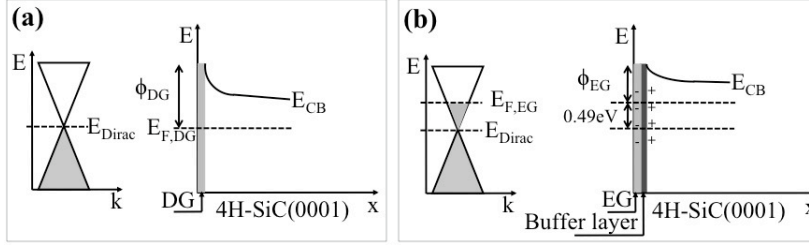


Figure 5.6: Band diagrams of graphene/4HSiC(0001) Schottky contact for (a) DG-SiC(0001) and (b) EG-SiC(0001). In contrast to DG, due to presence of positively charged buffer layer, the EG film is negatively doped.

considering that the SBHs on positions not covered with graphene remain similar. The SBH difference must then be explained in terms of the band diagrams schematically drawn in Figures 5.6(a) and 5.6(b). Here,  $E_c$  is the energy of the conduction band edge,  $E_F$  is the Fermi energy at the bulk 4H-SiC,  $E_{F,DG}$  is the Fermi energy of DG, and  $E_{F,EG}$  the Fermi energy of EG. Due to the weak (van der Waals-like) interaction with the substrate, DG can be considered neutral (or close to neutral) in the absence of external bias. In this case,  $E_{F,gr}$  should (more or less) coincide with the Dirac point energy ( $E_{Dirac}$ ). Hence, in the first approximation, the SBH between DG and the n-type 4H-SiC epilayer should be given by the difference between the neutral graphene work function ( $W_{gr} \approx 4.5$  eV) [11] and the 4H-SiC electron affinity ( $\chi_{4H-SiC} \approx 3.7$  eV) [12]. We found 0.85 eV, instead of 0.8 eV, predicted by the simple model, and this supports completely our assumptions.

The mSBH in the case of EG can now be explained in terms of a pinning of  $E_{F,EG}$  at an average value ( $\sim 0.49$  eV higher than  $E_{F,DG}$ , as shown in Figure 5.6(b)). As already said, for the sake of simplicity, we assumed neutral DG. This is only a first-order approximation but, in any case, the direct consequence is a reduction in  $W_{gr}$  by the Fermi energy difference  $\Delta = 0.49$  eV. This pinning is a direct evidence of the presence of positively charged states located at the interface between the Si face of 4H-SiC and C-rich ( $6\sqrt{3} \times 6\sqrt{3}$ )R30° reconstructed buffer layer.

This is consistent with recent theoretical results [13] showing, by electronic structure calculations of EG nanoribbons on (0001) SiC, a pinning of the Fermi level in the conduction band due to interface dangling bonds. This is also consistent with recent measurements of EG band structure by angle-resolved

### 5.3. Effect on electrostatic properties

---

photoelectron spectroscopy (ARPES), showing a  $\sim 0.4$  eV shift of the Fermi level with respect to the Dirac point, resulting in n-type doping of the graphene layers [14]. Macroscopic measurements of the SBH between thin graphite films and the Si face (on axis and  $8^\circ$  off axis) or C face of 4H- and 6H-SiC have been also reported, [15] for different dopant concentrations of the substrate (from  $10^{16}$  to  $10^{18}$   $\text{cm}^{-3}$ ). For lowest doping levels the SBH was determined by I-V and C-V measurements on test structures, whereas for highest concentrations, photoemission spectroscopy (PES) was applied. For graphite/4H-SiC (0001) the reported SBH by PES is  $0.6 \pm 0.1$  eV, in agreement with the value obtained by C-V measurements (0.59 eV), while the SBH obtained by I-V curves is 0.4 eV. However, ARPES, PES, macroscopic electrical measurements, and Raman spectroscopy give average values over the investigated area. Only scanning probe techniques can give nanoscale resolution information, like the evidence of a non-uniform energy distribution for the interface states.

We can evaluate the interfacial charge density from the obtained Fermi energy difference. The electron density in graphene is given by,

$$n = C_q \frac{(E_F - E_{Dirac})}{q} \quad (5.1)$$

The quantum capacitance of a graphene monolayer at  $E_F - E_{Dirac} = 0.49$  is approximately,  $C_q = 6 \times 10^{-6}$  F/ $\text{cm}^2$ . Then we find that the average graphene doping is  $\sim 1.8 \times 10^{13} \text{cm}^{-2}$ . A corresponding positive charge must be present at the interface. Following similar logic and focusing on the spread of mSBH values for EG/4H-SiC we find that the extreme (local) values vary from about  $\sim 1 \times 10^{12}$  to  $\sim 5 \times 10^{13} \text{cm}^{-2}$  at a few  $\mu\text{m}$  lateral distance that was probed by SCurS. Such significant local inhomogeneities are in part due to the peculiar growth mechanism of EG on the off-axis 4H-SiC epilayer. A better understanding of this mechanism is necessary, also in view of integrating EG electronics with SiC devices (commonly fabricated on low-doped off-axis epilayers) for future rf applications.

In the further discussion, the effect of this peculiar interface related issues on the local electrostatic and transport properties is investigated.

## 5.3 Effect on electrostatic properties

This section, focuses on a comparative investigation of quantum capacitance, local density of states of EG on 4H-SiC(0001) with graphene exfoliated-and-deposited on 4H-SiC(0001)-DG-SiC. In contrast to EG, one of the benefits of DG is that the crystal quality of parent HOPG (highly oriented pyrolytic graphite)

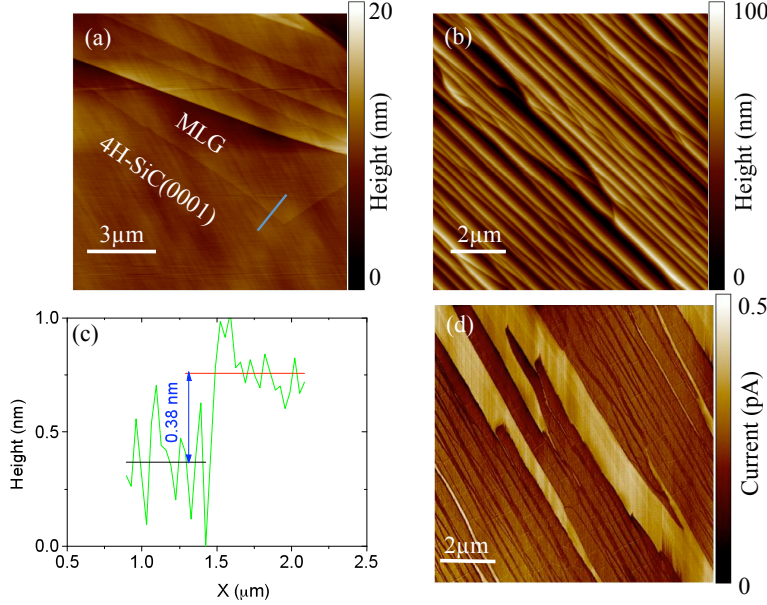


Figure 5.7: Tapping mode AFM micrograph of (a) a prototypical graphene flake deposited on 4H-SiC(0001) and (b) graphene epitaxially grown on 4H-SiC(0001). Corresponding linescan on a monolayer exfoliated graphene in (c) and TR-CAFM map on epitaxial graphene in (d).

crystal is maintained and graphene layers are produced with minimum artificial defects. Additionally, DG offers electrically clean interface between graphene and 4H-SiC(0001) with – in principle – only the van der Waals interaction holding the graphene films on the substrate. The two representative samples are depicted in Figure 5.7.

In this particular case, under the influence of backgate bias the low doped epilayer in  $n^-4\text{H-SiC}/n^{++}4\text{H-SiC}$  stack is fully depleted. Therefore, for both samples the total capacitance measured on graphene/4H-SiC has two distinct contributions. First, the depletion region capacitance ( $C_{depl}$ ) associated with the  $n^-4\text{H-SiC}/n^{++}4\text{H-SiC}$  stack, while the second is  $C_q$  associated with graphene. The total capacitance of this system is given by the series combination of the

### 5.3. Effect on electrostatic properties

two capacitances,

$$C_{tot} = \frac{C_q C_{depl}}{C_q + C_{depl}} = A_{eff} \frac{C'_q C'_{depl}}{C'_q + C'_{depl}} \quad (5.2)$$

where  $C'_{depl}$  denotes the per unit area depletion capacitance.  $A_{eff}$  (and in turn  $r_s$ ) can be evaluated by SCapS measurements on graphene/4H-SiC and on bare 4H-SiC substrate [16, 17]. Mathematically,

$$A_{eff} = \pi r_s^2 = \frac{|\Delta C_{tot}|}{|\Delta C_{SiC}|} A_{tip} \quad (5.3)$$

$|\Delta C_{tot}|$  is the absolute value of capacitance variations as measured on ‘Pt tip/graphene/4H-SiC’ stack, while  $|\Delta C_{SiC}|$  is the absolute value of capacitance variations as measured on ‘Pt tip/4H-SiC’ stack.

Figure 5.8 depicts typical SCapS characteristics obtained on DG (Figure 5.8(a)) and EG (Figure 5.8(b)). As expected, two distinct categories of curves can be distinguished in both the cases. Interestingly, capacitance characteristics obtained on 4H-SiC(0001) substrate are essentially similar for both DG and EG, however it is quite evident that the characteristics obtained on graphene for EG show prominent differences with DG.  $|\Delta C_{tot}|$  for EG is much lower and shows local variations in the spectroscopic signals obtained on an array of positions. According to theory presented above it translates into wider variations in the  $r_s$  for EG compared to DG and is depicted in Figure 5.9. On average we observed  $\sim 63\%$  decrease (in comparison with DG) along with wider ( $\pm 17\%$ ) variations in local  $r_{scr}$  for EG. This is indicative of significant variations in the local electrostatic properties in EG.

Furthermore,  $r_s$  allows us to evaluate  $C_q$  by the relation [16],

$$C_q(V_g) = \frac{\pi r^2}{\sqrt{2\pi\hbar^2\nu_F} f(N)} \sqrt{\frac{q^3\epsilon_0\epsilon_{SiC}V_g}{t_{depl}}} \quad (5.4)$$

where,  $\epsilon_{SiC}$  the relative dielectric constant of 4H-SiC,  $t_{depl}$  the depletion layer thickness and  $f(N)$  is a function of the ratio  $A_{eff}/A_{tip}$ .

Upon comparison we found on average an  $\sim 86\%$  lower values for  $C_q$  in case of EG compared to DG (Figure 5.10(a) and (b)). Such variations in  $C_q$  can either come from structural defects in graphene [18, 19] and/or electrical charges at the graphene/SiC interface as found in the previous section [20]. Finally, the local density of states (LDOS) are reported in Figure 5.10 (c). Significant variations in LDOS (Figure 5.10(d)) point towards variations in local transport

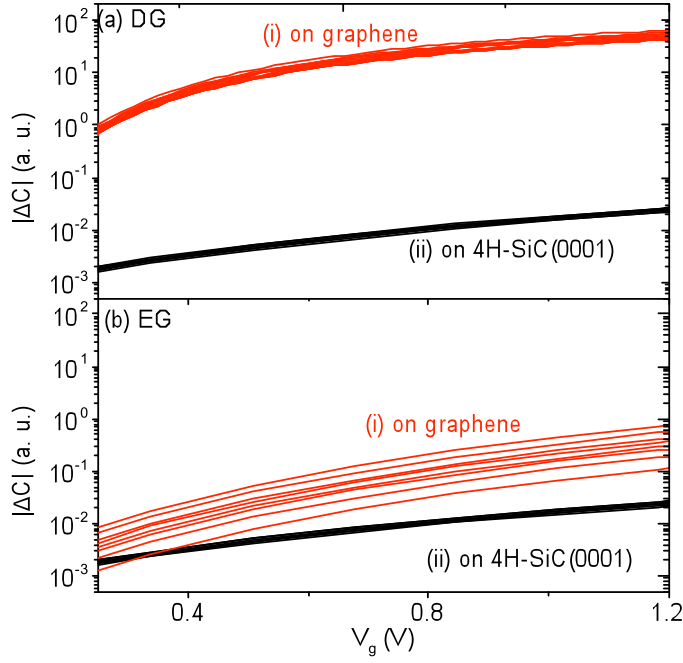


Figure 5.8: A typical set of SCS curves obtained on (a) graphene deposited on 4H-SiC(0001), (b) graphene epitaxially grown on 4H-SiC(0001). Two families of curves corresponding to SCS signal (i) on graphene and (ii) on 4H-SiC(0001) can be distinguished.

#### 5.4. Effect on the local transport properties

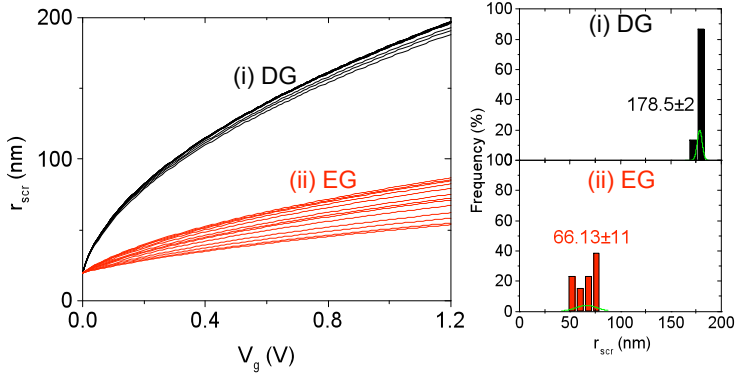


Figure 5.9: Screening length as evaluated in DG and EG. Wider variations in  $r_s$  for EG can be observed and are indicative of local variations in electrostatic properties in EG.

properties (Fermi velocity, conductance, mobility) in EG. In view of this, further investigations are carried out in the following section.

### 5.4 Effect on the local transport properties

Ideally, in a very clean graphene sheet (i.e. with no adsorbed impurities) sufficiently isolated from its environment to be considered free standing, charge carriers can exhibit a giant intrinsic mobility [21] and can travel for micrometers without scattering at room temperature. Indeed, very high values of mobility ( $> 2 \times 10^5 \text{ cm}^2 \text{V}^{-1} \text{s}^{-1}$ ) and electron mean free path have been observed in vacuum and at low temperature (5K) in ‘suspended’ graphene, obtained by locally etching the substrate under the sheet, after a cleaning by current-induced heating [22]. However, graphene for electronics applications is commonly supported by a dielectric substrate (typically  $\text{SiO}_2$  or high- $\kappa$  dielectrics) or by semi-insulating SiC. The values of the electron mean free path and mobility observed in supported graphene layers are usually significantly lower than in suspended ones. So far, graphene on silicon dioxide substrate has shown field-effect mobility ranging from 0.1 to  $2 \times 10^4 \text{ cm}^2 \text{V}^{-1} \text{s}^{-1}$  [23, 24].

Several factors that can affect the transport of carriers in graphene and de-

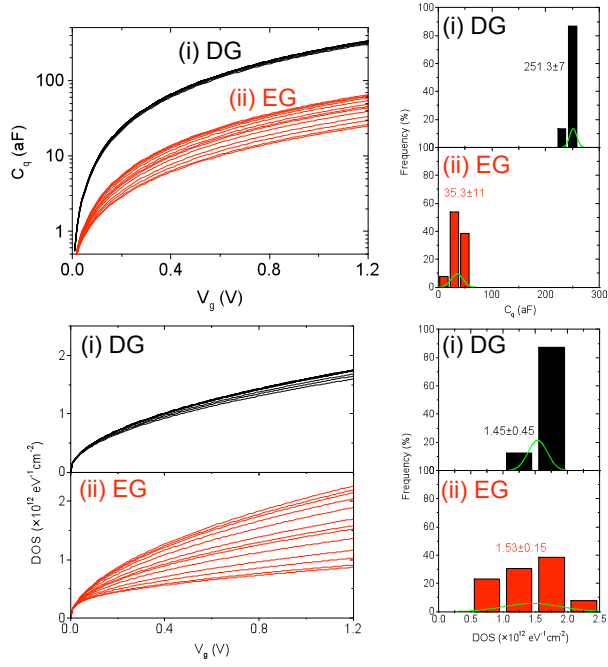


Figure 5.10: Local variations, as evaluated from screening length ( $r_s$ ), in quantum capacitance ( $C_q$ ) are shown in (a) and (b) while those in local density of states (LDOS) are shown in (c) and (d) for (i) DG and (ii) EG.



## 5.4. Effect on the local transport properties

---

grade its electron mean free path and mobility have been identified and are still under active debate. Carrier scattering with charged impurities [25, 26, 27, 28, 29, 30, 31, 32, 33] (either adsorbed on graphene surface or trapped at the interface with the substrate) is typically indicated as one of the main mechanisms limiting mobility of graphene 2DEG. Since charged impurities interact with graphene 2DEG by a screened Coulomb potential, the strength of the interaction is expected to decrease significantly with increasing the permittivity of the substrate and/or of the dielectric layer deposited on graphene. To date, contrasting experimental results have been reported in the literature on the effect of increasing the ‘environment’ permittivity on graphene transport properties. As an example, Jang et al. [34] observed an improvement in mobility placing solid ice on the surface of graphene (on  $\text{SiO}_2$ ) due to increased dielectric screening of long-range impurity scattering. On the contrary, Ponomarenko et al. [35], observed no significant changes in carrier mobility, placing graphene on various substrates and in high- $\kappa$  media. They also suggested that scattering by charged impurities is not the only mechanism that limits the mean free path attainable for substrate-supported graphene. Inelastic scattering by surface polar phonons (SPP) of the substrate [36] has been indicated as an additional mechanism limiting the carrier mobility in graphene. It has been shown theoretically that, due to the polar nature of the substrates commonly used for graphene (like  $\text{SiO}_2$  and  $\text{SiC}$ ), a long-range polarization field is associated to the thermally induced lattice vibrations at the surface of the substrate (i.e. the SPP) [36]. This field electrostatically couples with the 2DEG, resulting in a sizeable degradation of mobility at room temperature. Recently, the experimental evidence of such SPP scattering at room temperature has been reported, based on temperature dependent transport measurements performed on devices in graphene deposited on  $\text{SiO}_2$  substrate [21]. It has also been predicted that for graphene on  $\text{SiC}$ , the SPP scattering has a weaker effect on the electron mobility than for graphene on  $\text{SiO}_2$ , due to weaker polarizability of  $\text{SiC}$  and relatively high phonon frequencies associated with the hard Si-C bonds [36]. However, experimental demonstration of this beneficial effect of using a  $\text{SiC}$  substrate has not been shown to date.

### 5.4.1 Local electron mean free path

We evaluated the local electron mean free path for (i) graphene exfoliated and deposited on 4H- $\text{SiC}$ (0001) (DG- $\text{SiC}$ ), (ii) graphene epitaxially grown on 4H- $\text{SiC}$ (0001) (EG- $\text{SiC}$ ), and (iii) graphene deposited on  $\text{SiO}_2$  (DG- $\text{SiO}_2$ ). The experimental results have been explained considering significant effects of the substrate permittivity and of substrate SPP on electron dynamics in graphene.

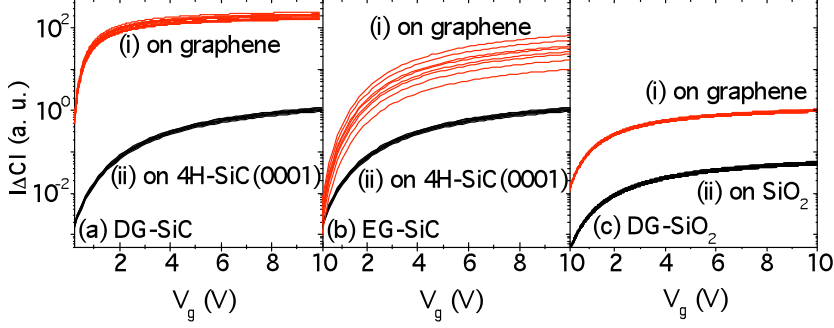


Figure 5.11: Representative characteristics obtained by SCapS on (a) graphene deposited on 4H-SiC(0001) (DG-SiC), (b) graphene epitaxially grown on 4H-SiC(0001) (EG-SiC), and (c) graphene deposited on SiO<sub>2</sub> (DG-SiO<sub>2</sub>). Two distinct families of curves correspond to tip placement (i) “on graphene” and (ii) “on substrate” are indicated. A typical scan comprises of an array of 5×5 positions with an interstep distance of 1×1 μm<sup>2</sup>.

The DG-SiO<sub>2</sub> sample was prepared by mechanical exfoliation of graphene from HOPG and deposited on 100 nm SiO<sub>2</sub> thermally grown on degenerately doped n<sup>+</sup>Si. DG-SiC and EG-SiC were obtained by the same methods described in the previous section. The electron mean free path at room temperature was ‘locally’ evaluated at different positions on the graphene by the method based on capacitance measurements made with the probe of an SCM. Details of the method are explained in the Section 3.3. In the case of DG-SiO<sub>2</sub>, the SiO<sub>2</sub> film works as the gate dielectric and the n<sup>+</sup>Si substrate works as the semiconductor of a metal-insulator-semiconductor (MIS) capacitor. Similarly, both in the case of DG-SiC and of EG-SiC, the very lowly doped SiC film works as the gate dielectric, whereas the n<sup>+</sup>SiC substrate works as the semiconductor back gate of the capacitor. Capacitance measurements were carried out using SCapS. All details about the method are described in Sections 2.2.1 and 3.2.1. Bias amplitude  $V_g$  was varied from 0 to 10 V at bias frequency of  $\omega = 100$  kHz.

In Figure 5.11 are reported representative capacitance-voltage characteristics obtained on DG-SiC (a), EG-SiC (b) and DG-SiO<sub>2</sub> (c) on arrays of 5×5 positions with an inter-step distance of 1 μm × 1 μm. For reference, SCapS measurements were carried also on bare SiO<sub>2</sub> and SiC regions of the samples. When the tip is in contact on graphene, upon application of a positive bias, an accumulation

#### 5.4. Effect on the local transport properties

of electrons is induced in the graphene sheet. These electrons spread over the  $A_{eff}$  around the tip/graphene contact.  $A_{eff}$  represents the effective area of the graphene/insulator/semiconductor capacitor and can be evaluated as  $A_{eff} = A_{tip}(|\Delta C_{gr}|/|\Delta C_{sub}|)$  where  $|\Delta C_{gr}|$  and  $|\Delta C_{sub}|$  are the absolute values of capacitance variations measured on graphene/substrate and on substrate not covered by graphene, respectively. It has been shown in Section 3.3 that  $A_{eff}$  is related to the local electron mean-free path ( $l_{gr}$ ) in graphene by the relation,

$$A_{eff} = \pi r_s^2 = \pi l_{gr}^2 \quad (5.5)$$

where  $l_{gr}$  is the length over which the electrons diffuse in graphene under biased conditions following ‘few’ subsequent scattering events. Figure 5.12(a) shows the evaluated  $l_{gr}$  for DG-SiC, EG-SiC and DG-SiO<sub>2</sub>.  $l_{gr}$  is reported versus  $n_{Vg}-n_0$ , being  $n_{Vg}$  the carrier density induced in graphene by the gate bias  $V_g$  and  $n_0$  the carrier density at  $V_g=0$ . The values of  $n_{Vg}-n_0$  are obtained as,

$$n_{Vg} - n_0 = \frac{\varepsilon_0 \varepsilon_{ins} V_g}{q t_{ins}} \quad (5.6)$$

where  $\varepsilon_{ins}$  and  $t_{ins}$  are the relative dielectric constant and the thickness of the insulating layer under graphene, all the other symbols carry their usual meaning. The histograms of the  $l_{gr}$  values at a fixed value of  $n_{Vg}-n_0=1.5 \times 10^{11} \text{cm}^{-2}$  are reported in Figure 5.12(b) for DG-SiC (i), EG-SiC (ii) and DG-SiO<sub>2</sub>(iii).

It is worth noting that  $l_{gr}$  in EG-SiC is on average 37% of  $l_{gr}$  in DG-SiC, but the spread of the  $l_{gr}$  values in EG-SiC is much larger than in DG-SiC. These differences can be explained in terms of the peculiar structure of EG/4H-SiC(0001) interface.

This can be explained as follows. The precursor of graphene formation is a C-rich layer with  $(6\sqrt{3} \times 6\sqrt{3})R30^\circ$  reconstruction. As has been mentioned in Section 5.2, this layer is an intermediate buffer layer between the Si face of SiC and the first graphene layer, which may be more or less defective with more or less dangling bonds at the interface with the Si face. Also the nanoscale measurements of the current transport across EG/4H-SiC(0001) interface indicated that a laterally inhomogeneous distribution of positive charges is associated to these dangling bonds between the buffer layer and the bulk substrate. This interface charge can explain both the lower average value and the larger spread in the local  $l_{gr}$  values in the case of EG-SiC than in the case of DG-SiC. It is also worth noting that  $l_{gr}$  on DG/SiC is on average  $\sim 4\times$  than on DG/SiO<sub>2</sub> and the spread of the  $l_{gr}$  values are comparable in the two cases. This difference can be explained in terms of the higher permittivity of SiC ( $\varepsilon_{SiC}=9.7$ ) than SiO<sub>2</sub>

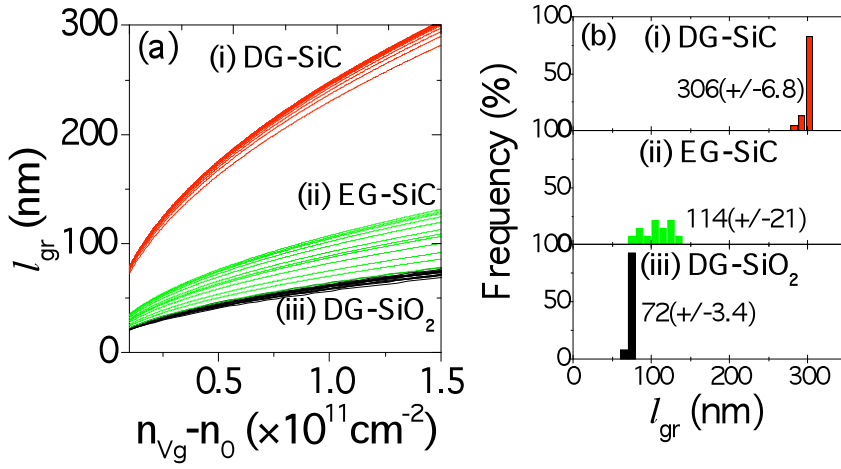


Figure 5.12: Evaluated electron mean-free path in graphene ( $l_{gr}$ ) for (i) DG-SiC, (ii) EG-SiC, and (iii) DG-SiO<sub>2</sub> is depicted in (a). In (b) are depicted the corresponding histograms plotted at  $n_{Vg} - n_0 = 1.5 \times 10^{11} \text{ cm}^{-2}$ . An average increase of  $\sim 4\times$  and  $\sim 1.5\times$  can be seen in  $l_{gr}$  for DG-SiC and EG-SiC, respectively, as compared to  $l_{gr}$  for DG-SiO<sub>2</sub>.

#### 5.4. Effect on the local transport properties

( $\epsilon_{SiO_2}=3.9$ ) and of the lower coupling of the 2DEG with surface polar phonons in SiC than in SiO<sub>2</sub>. This is better discussed in the following.

##### 5.4.2 Charge scattering at the graphene/substrate interface

The electron mean-free path limited by scattering on charged impurities ( $l_{ci}$ ) in graphene could be expressed as a function of the carrier density as [37],

$$l_{ci}(n) = \frac{16\epsilon_0\epsilon\hbar\nu_F^2}{Z^2q^4N_{ci}} \left(1 + \frac{q^2}{\pi\hbar\nu_F\epsilon_0\epsilon}\right)^2 \sqrt{\pi n} \quad (5.7)$$

$Z$  is the net charge of the impurity (assumed to be 1 for this study),  $N_{ci}$  is the impurity density and  $\epsilon$  is the average between the relative permittivity of the substrate ( $\epsilon_{ins}$ ) and of vacuum permittivity ( $\epsilon_{vac}=1$ ). The electron mean free path limited by scattering with a SPP phonon mode of characteristic frequency  $\omega_v$  can be expressed as [38],

$$l_{SPP_v} = \sqrt{\frac{\beta}{\hbar\omega_v}} \frac{\hbar\nu_F 4\epsilon_0}{q^2} \frac{q\nu_F}{F_v^2} \frac{\exp(k_0 z_0)}{N_{SPP,v}} \frac{\hbar\sqrt{\pi}}{q} \quad (5.8)$$

where  $k_0 \approx \sqrt{(2\omega_v/\nu_F^2)^2 + \chi n}$ ,  $\chi \approx 10.5$ ,  $\beta \approx 0.153 \times 10^{-4}$  eV [38] and  $z_0 \approx 0.35$  nm is the separation between the polar substrate and graphene flake.  $N_{SPP,v}$  is SPP phonon occupation number. The magnitude of the polarization field is given by the Fröhlich coupling constants,  $F_v^2$  [39].

In Figure 5.13(a) and (b) the average of the  $l_{gr}$  vs.  $n_{VG}-n_0$  curves measured on different tip positions on DG-SiC and DG-SiO<sub>2</sub> are fitted with the equivalent mean free path obtained by,

$$l_{eq\_sim}^{-1} = l_{ci}^{-1} + \sum_v l_{SPP,v}^{-1} \quad (5.9)$$

The characteristic SPP frequencies and the corresponding Fröhlich coupling constants for SiO<sub>2</sub> and 4H-SiC substrate are listed in Table 5.1. The only fitting-parameter used in Equation 5.9 is  $N_{ci}$ . We found the charged-impurity density limiting the mean free path to be  $\sim 7 \times 10^{10} \text{ cm}^{-2}$  for DG-SiC, and  $\sim 1.8 \times 10^{11} \text{ cm}^{-2}$  for DG-SiO<sub>2</sub>. The calculated  $l_{SPP}$  and  $l_{ci}$  versus  $n_{VG}-n_0$  curves are also reported in both cases. It is worth noting that  $l_{SPP}$  for DG-SiC is more than five times  $l_{SPP}$  for DG-SiO<sub>2</sub>. As a result, scattering by charged impurities is the limiting scattering mechanism in DG-SiC (see Figure 5.13(a)), whereas a

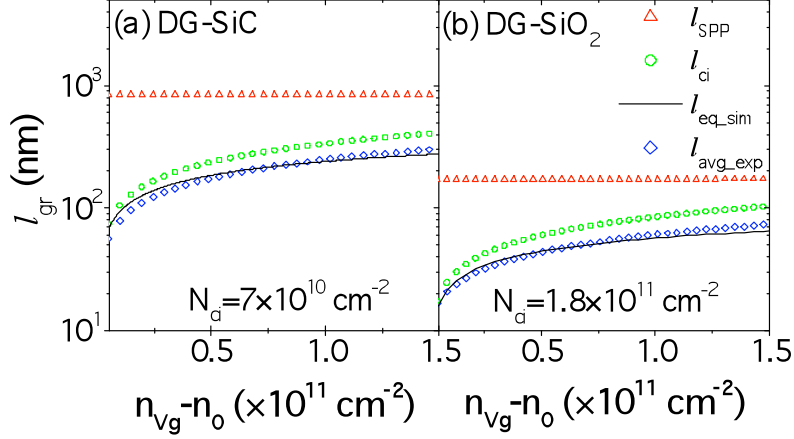


Figure 5.13: A representative graph of prominent limiting contributions to the room temperature electron mean free path in graphene evaluated for the cases of (a) DG-SiC and (b) DG-SiO<sub>2</sub>:  $l_{SPP}$  (red up-triangles) and  $l_{ci}$  (green circles). The  $l_{ci}$  is simulated by varying the charged-impurity density  $N_{ci}$ . The best match between  $l_{eq\_sim}$  (black solid line) and  $l_{avg\_exp}$  (blue diamonds) was found for  $N_{ci} = 7 \times 10^{10} \text{ cm}^{-2}$  (DG-SiC),  $1.8 \times 10^{11} \text{ cm}^{-2}$  (DG-SiO<sub>2</sub>).

	SiO <sub>2</sub>	4H-SiC
$\hbar\omega_{SPP,1}$ (meV)	58.9	116.0
$\hbar\omega_{SPP,2}$ (meV)	156.4	-
$F_1^2$ (meV)	0.237	0.735
$F_1^2$ (meV)	1.612	-

Table 5.1: The characteristic SPP frequencies and the corresponding Fröhlich coupling constants for SiO<sub>2</sub> and 4H-SiC.

## 5.5. Summary

---

significant contribution is played by scattering with SPP in the case of DG-SiO<sub>2</sub>, especially at higher carrier densities (see Figure 5.13(b)).

## 5.5 Summary

In this analysis we investigated the local electrical properties of graphene/4H-SiC(0001) interface and the role of interface related charge scattering mechanisms on the local electrostatic and transport properties in graphene 2DEG. In particular, the nanoscale current transport studies on graphene deposited on n<sup>-</sup>4H-SiC(0001) and graphene grown epitaxially on n<sup>-</sup>4H-SiC(0001) by SCurS revealed that graphene forms a Schottky barrier on top of SiC. More importantly, the Schottky barrier height is modified differently on DG-SiC and EG-SiC. Due to Fermi-level pinning towards the conduction band, a much reduced SBH has been observed on EG as compared to DG. This effect shows that positively charged states localize at the interface between the C-rich ( $6\sqrt{3}\times 6\sqrt{3}$ )R30° reconstructed buffer layer and the Si face. The local spectroscopic data over a few  $\mu\text{m}$  lateral region showed that the energy distribution of these states is nonuniform and varying rapidly at the nanoscale.

Furthermore, the local capacitive behavior revealed distinct variations in the electrostatic properties of EG-SiC. We found a  $\sim 63\%$  smaller screening length ( $r_s$ ), and  $\sim 86\%$  lower  $C_q$  along with significant variations in the LDOS for EG-SiC in comparison with DG-SiC. Such detrimental effects are attributed to the non-ideal graphene/SiC interface for EG grown on 4H-SiC(0001).

Moreover, the local electron mean-free path ( $l_{gr}$ ) in graphene deposited on 4H-SiC(0001) (DG-SiC), graphene epitaxially grown on 4H-SiC(0001) (EG-SiC) was probed and compared with graphene deposited on SiO<sub>2</sub> (DG-SiO<sub>2</sub>). We observed a  $\sim >4\times$  increase in  $l_{gr}$  for DG-SiC compared to DG-SiO<sub>2</sub> owing predominantly to lesser SPP phonon scattering ( $\sim <5\times$ ) and better dielectric screening of charged-impurities compared to SiO<sub>2</sub> substrates. On the other hand,  $l_{gr}$  on EG was observed to be on average  $\sim 0.4$  times than on DG-SiC and exhibits large variations from point to point, due to the presence of a laterally inhomogeneous positively charged layer at EG/SiC interface.





# References

- [1] C. Berger, Z. Song, Z. Li, W. Wu, N. Brown, C. Naud, et al., *Science* 312, 1191 (2006)
- [2] X. Li, W. Cai, J. An, S. Kim, J. Nah, D. Yang, R. Piner, A. Velamakanni, I. Jung, E. Tutuc, S. K. Banerjee, L. Colombo, R. S. Ruoff, *Science* 324 1312 (2009)
- [3] W. A. de Heer, C. Berger, et al.: <http://arxiv.org/abs/1003.4776>
- [4] A. Mattausch and O. Pankratov, *Phys. Rev. Lett.* 99, 076802 (2007)
- [5] F. Varchon, R. Feng, J. Hass, X. Li, B. N. Nguyen, C. Naud, P. Mallet, J.-Y. Veuillen, C. Berger, E. H. Conrad, and L. Magaud, *Phys. Rev. Lett.* 99, 126805 (2007)
- [6] K. V. Emtsev, F. Speck, Th. Seyller, L. Ley, and J. D. Riley, *Phys. Rev. B* 77, 155303 (2008)
- [7] K. V. Emtsev, Th. Seyller, F. Speck, L. Ley, P. Stojanov, J. D. Riley, and R. C. G. Leckey, *Mater. Sci. Forum* 556-557, 525 (2007)
- [8] F. Giannazzo, F. Roccaforte, V. Raineri, and S. F. Liotta, *EPL* 74, 686 (2006)
- [9] F. Giannazzo, F. Roccaforte, F. Iucolano, V. Raineri, F. Ruffino, and M. G. Grimaldi, *J. Vac. Sci. Technol. B* 27, 789 (2009)
- [10] N. Camara, J.-R. Huntzinger, G. Rius, A. Tiberj, N. Mestres, F. Perez-Murano, P. Godignon, and J. Camassel, *Phys. Rev. B* 80, 125410 (2009)
- [11] G. Giovannetti, P. A. Khomyakov, G. Brocks, V. M. Karpan, J. van den Brink, and P. J. Kelly, *Phys. Rev. Lett.* 101, 026803 (2008)

- [12] H. Na, H. Kim, K. Adachi, N. Kiritani, S. Tanimoto, H. Okushi, and K. Arai, *J. Electron. Mater.* 33, 89 (2004)
- [13] I. Deretzis and A. La Magna, *Appl. Phys. Lett.* 95, 063111 (2009)
- [14] T. Ohta, A. Bostwick, T. Seyller, K. Horn, and E. Rotenberg, *Science* 313, 951 (2006)
- [15] S. A. Reshanov, K. V. Emtsev, F. Speck, K.-Y. Gao, T. K. Seyller, G. Pensl, and L. Ley, *Phys. Status Solidi B* 245, 1369 (2008)
- [16] S. Sonde, F. Giannazzo, V. Raineri, and E. Rimini, *J. Vac. Sci. Technol. B*, 27, 868 (2009)
- [17] F. Giannazzo, S. Sonde, V. Raineri, and E. Rimini, *Nano Lett.*, 9, 23(2009)
- [18] S. Sonde, F. Giannazzo, V. Raineri, and E. Rimini, *Phys. Status Solidi B*, 247, 907 (2010)
- [19] F. Giannazzo, S. Sonde, V. Raineri, and E. Rimini, *Appl. Phys. Lett.*, 95, 263109 (2009)
- [20] S. Sonde, F. Giannazzo, V. Raineri, R. Yakimova, J.-R. Huntzinger, A. Tiberj, and J. Camassel, *Phy. Rev B*, 80, 241406(R) (2009)
- [21] J. H. Chen, C. Jang, S. Xiao, M. Ishigami and M. S. Fuhrer, *Nat. Nanotechnol.* 3, 206 (2008)
- [22] K. I. Bolotin, K. J. Sikes, Z. Jiang, M. Klima, G. Fudenberg, J. Hone, P. Kim and H. L. Stormer, *Solid State Commun.* 146, 351, (2008)
- [23] Y.-W. Tan, Y. Zhang, K. Bolotin, Y. Zhao, S. Adam, E.H. Hwang, S.D. Sarma, H.L. Stormer, P. Kim, *Phys. Rev. Lett.* 99, 246803 (2007)
- [24] F. Giannazzo, S. Sonde, V. Raineri, and E. Rimini, *Appl. Phys. Lett.* 95, 263109 (2009)
- [25] J. H. Chen, C. Jang, S. Adam, M. S. Fuhrer, E. D. Williams and M. Ishigami, *Nat. Phys.* 4, 377 (2008)
- [26] T. Ando, *J. Phys. Soc. Japan* 75, 074716 (2006)
- [27] K. Nomura and A. H. MacDonald, *Phys. Rev. Lett.* 98, 076602 (2007)

## REFERENCES

---

- [28] V. V. Cheianov and I. Fel'koV, Phys. Rev. Lett. 97, 226801 (2006)
- [29] E. H. Hwang, S. Adam and S. Das Sarma, Phys. Rev. Lett. 98, 186806 (2007)
- [30] S. Adam, E. H. Hwang and V. M. Galitsky, Proc. Natl Acad. Sci. USA 104, 18392 (2007)
- [31] D. S. Novikov, Appl. Phys. Lett. 91, 102102 (2007)
- [32] M. Trushin and J. Schliemann, Phys. Rev. Lett. 99, 216602 (2007)
- [33] X. Z. Yan, Y. Romiah and C. S. Ting, Phys. Rev. B 77, 125409 (2008)
- [34] C. Jang, S. Adam, E. D. Williams, S. Das Sarma and M. S. Fuhrer, Phys. Rev. Lett. 101, 146805 (2008)
- [35] L. A. Ponomarenko, R. Yang, T. M. Mohiuddin, M. I. Katsnelson, K. S. Novoselov, S. V. Morozov, A. A. Zhukov, F. Schedin, E. W. Hill, A. K. Geim, Phys. Rev. Lett. 102, 206603 (2009)
- [36] S. Fratini, F. Guinea, Phys. Rev. B 77, 195415 (2008)
- [37] T. Stauber, N. M. R. Peres, and F. Guinea, Phys. Rev. B 76, 205423 (2007)
- [38] V. Perebeinos and P. Avouris, <http://arxiv.org/abs/1003.2455v1>
- [39] S. Q. Wang and G. D. Mahan, Phys. Rev. B 6, 4517 (1972)



# Chapter 6

## Conclusions

### 6.1 Introduction

The possibility of graphene as a complimentary material to Si for prospective nanoelectronics has called for nanoscale manipulation of its electronic properties. As a consequence of that development of techniques that can characterize and/or control the local effects in graphene are essential, since such local properties are inaccessible in standard transport measurements carried out on macroscopic graphene devices. During the course of this thesis, significant contributions were made towards this by developing methods for the characterization of local electrostatic and transport properties in graphene. Owing to nanoscale lateral resolution Atomic Force Microscopy based characterization methods are obvious and important tools to probe local properties in graphene. Scanning Capacitance Spectroscopy (SCapS), Scanning Current Spectroscopy (SCurS) and Torsion Resonance Conductive Atomic Force Microscopy (TR-CAFM) were employed for non-destructive electrical characterization of graphene.

Graphene samples for the study were obtained by mechanical exfoliation and thermal graphitization methods. In case of the exfoliated graphene samples, extensive characterization of the flakes was carried out with Optical Microscopy (OM), MicroRaman Spectroscopy ( $\mu$ R) and TappingMode Atomic Force Microscopy to locate monolayer graphene flakes. Exfoliated graphene was obtained on insulating (Silicon dioxide and Strontium Titanate) and semi-insulating (low doped Silicon Carbide) substrates. For epitaxial graphene the identification and coverage homogeneity was checked with  $\mu$ R and TR-CAFM (a high-resolution

current mapping technique, which is especially useful in studying the initial stages of graphene formation on SiC substrate). To evaluate the number of layers on epitaxial graphene, in addition to  $\mu\text{R}$ , we performed extensive calibration based on height measurements on selectively etched out trenches in graphitized SiC and high-resolution transmission electron microscopy imaging.

We developed a method to evaluate the electrostatic properties, quantum capacitance and density of states, in graphene on insulating and semi-insulating substrates by locally measuring capacitance with SCapS. This method was extended to show that the screening length evaluated with SCapS in graphene is equivalent to the local electron mean free path in graphene. Together, these methods proved to be a powerful tool to probe local variations in electrostatic and transport properties in graphene.

These methods were applied to graphene irradiated with controlled amount of high-energy ions to study the effect of defect formation in graphene on electrical properties of 2DEG. This study was supported by extensive  $\mu\text{Raman}$  spectroscopic and high-resolution TappingMode Atomic Force Microscopy investigations.

Furthermore, the graphene/SiC interface was analyzed for electrical properties by studying nanoscale current transport across it. In particular, the role of buffer layer on the local work function variations in epitaxial graphene was clarified. Moreover, the effect of interface related scattering mechanisms on local electrostatic and transport properties was evaluated. In the following, Section 6.2 summarizes important conclusions.

## 6.2 Conclusions

To investigate nanoscale capacitive behavior of graphene deposited on  $\text{SiO}_2$  layers grown on  $\text{n}^+\text{Si}$ , the graphene/ $\text{SiO}_2/\text{n}^+\text{Si}$  stack can be modelled as Metal / Oxide / Semiconductor (MOS) capacitor. During this study it was observed that the capacitor effective area ( $A_{eff}$ ) responding to the AC bias applied to the backgate is much smaller than the geometrical area of the graphene sheet under study.  $A_{eff}$  increases linearly with the bias (i.e., proportionally to the induced charge density in graphene) and symmetrically for bias inversion. For each bias  $V_g$ , the value of  $A_{eff}$  is related to the minimum area necessary to accommodate the non stationary charges (electrons/holes) induced by the AC bias, according to the graphene density of states (DOS) at  $V_g$ . Interestingly, decreasing the  $\text{SiO}_2$  thickness from 300 to 100 nm, the slope of the  $A_{eff}$  versus bias curve strongly increases (by a factor of  $\sim 50$ ). The local quantum capacitance  $C_q$  (and in turn

## 6.2. Conclusions

---

the DOS) in the contacted graphene region can be calculated starting from the screening length (i.e., the radius of the disk with area  $A_{eff}$ ). SCapS allows determining the lateral variations in the values of  $C_q$  and DOS for different tip positions.

The  $C_q$  showed substantially higher values for graphene on high- $\kappa$  dielectric substrate strontium titanate (DG-STO) as compared to on  $\text{SiO}_2$  (DG- $\text{SiO}_2$ ) due predominantly to the increased effectively biased area in DG-STO, as a consequence of better dielectric screening of commonly observed charged impurities, on graphene and/or at the graphene/substrate interface, by the use of high permittivity substrate.

Furthermore, the screening length, evaluated by SCapS was shown to be equivalent to the local electron mean free path in graphene, by using the concepts of diffusivity, mobility and the Einstein relation. This continuum treatment is justifiable on the mesoscopic length scale (from 10 to 100 nm) investigated by SCapS.

Ion irradiation by high-energy ions (in our study 500 keV  $\text{C}^+$  ions) introduces defects into graphene sheets deposited on  $\text{SiO}_2$  in a controlled way. This was confirmed by combined use of Raman spectroscopy and AFM. Higher irradiation fluence resulted in higher amount of defects. Defects strongly influence the local electrical properties in graphene, particularly, giving an increase of the quantum capacitance per unit area, and lowering of Fermi velocity in/around the damaged regions. Also, defect scattering was observed to be the limiting mechanism in irradiated graphene, giving lower local electron mean free path and mobility compared to the pristine graphene where the limiting mechanism was observed to be the charged-impurity scattering.

Another important issue addressed was the clarification of the local electrical properties of graphene/4H-SiC(0001) interface and the role of interface related charge scattering mechanisms on the local electrostatic and transport properties in graphene 2DEG. Due to Fermi-level pinning towards the conduction band, a much reduced Schottky barrier height was obtained on EG-SiC as compared to DG-SiC. This is a direct consequence of positively charged states localize at the interface between the C-rich  $(6\sqrt{3} \times 6\sqrt{3})\text{R}30^\circ$  reconstructed buffer layer and the Si face. These states were observed to be non-uniformly distributed at the interface. Furthermore, the buffer layer related states affect the local capacitive behavior showing  $\sim 63\%$  smaller screening length, and  $\sim 86\%$  lower  $C_q$  along with significant variations in the LDOS for EG-SiC in comparison with DG-SiC.

Moreover, the local electron mean-free path ( $l_{gr}$ ) in graphene deposited on 4H-SiC(0001) (DG-SiC), showed  $\sim 4\times$  increase in  $l_{gr}$  for DG-SiC compared to DG- $\text{SiO}_2$  owing predominantly to lesser SPP phonon scattering ( $\sim 5\times$ ) and

better dielectric screening of charged-impurities compared to  $\text{SiO}_2$  substrates. On the other hand,  $l_{gr}$  on EG was observed to be on average  $\sim 0.4$  times than on DG-SiC and exhibits large variations from point to point, due to the presence of a laterally inhomogeneous positively charged layer at EG/SiC interface.



# List of Publications

## Journal contributions

This thesis is based on following publications:

1. “Screening length and quantum capacitance in graphene by scanning probe microscopy”, Giannazzo F., **Sonde S.**, Raineri V., Rimini E., NANO LETTERS, vol. 9; p. 23-29 (2009).
  - ISSN: 1530-6984, doi: 10.1021/nl801823n
2. “Dielectric thickness dependence of capacitive behavior in graphene deposited on silicon dioxide”, **Sonde S.**, Giannazzo F., Raineri V., Rimini E., JOURNAL OF VACUUM SCIENCE & TECHNOLOGY. B, vol. 27; p. 868-873 (2009).
  - ISSN: 1071-1023, doi: 10.1116/1.3081890
3. “Electrical properties of the graphene/4H-SiC (0001) interface probed by scanning current spectroscopy”, **Sonde S.**, Giannazzo F., Raineri V., Yakimova R., Huntzinger J.-R., Tiberj A., and Camassel J., PHYSICAL REVIEW. B (R), vol. 80; p. 2414061-2414064 (2009).
  - ISSN: 1098-0121, doi: 10.1103/PhysRevB.80.241406
4. “Investigation of graphene-SiC interface by nanoscale electrical characterization”, **Sonde S.**, Giannazzo F., Raineri V., Rimini E., PHYSICA STATUS SOLIDI B, vol. 247; p. 912-915 (2009).
  - ISSN: 0370-1972, doi: 10.1002/pssb.200982969

5. "Ion irradiation and defect formation in single layer graphene", Compagnini G., Giannazzo F., **Sonde S.**, Raineri V., Rimini E., CARBON, vol. 47; p. 3201-3207 (2009).
  - ISSN: 0008-6223, doi: 10.1016/j.carbon.2009.07.033
6. "Irradiation damage in graphene on SiO<sub>2</sub> probed by local mobility measurements", Giannazzo F., **Sonde S.**, Raineri V., Rimini E., APPLIED PHYSICS LETTERS, vol. 95; p. 2631091-2631093 (2009).
  - ISSN: 0003-6951, doi: 10.1063/1.328086
  - Also selected for publication on Virtual Journal of Nanoscale Science & Technology.
7. "Nanoscale capacitive behaviour of ion irradiated graphene on silicon oxide substrate", **Sonde S.**, Giannazzo F., Raineri V., Rimini E., PHYSICA STATUS SOLIDI B, vol. 247; p. 907-911, (2009).
  - ISSN: 0370-1972, doi: 10.1002/pssb.200982968
8. "Uniformity of epitaxial graphene on On-axis and Off-axis SiC probed by Raman spectroscopy and nanoscale current mapping", **Sonde S.**, Giannazzo F., Huntzinger J. -R., Tiberj A., Syvajarvi M., Yakimova R., Raineri V., Camassel J., MATERIALS SCIENCE FORUM, vol. 645-648; p. 607-610 (2010).
  - ISSN: 0255-5476, doi: 10.4028/www.scientific.net/MSF.645-648.607
9. "Role of ion irradiation induced lattice defects on nanoscale capacitive behavior of graphene", **Sonde S.**, Giannazzo F., Raineri V., Di Franco S., Marino A., Rimini E., SOLID STATE PHENOMENA, vol. 156-158; p. 305-311 (2010).
  - ISSN: 1012-0394, doi: 10.4028/www.scientific.net/SSP.156-158.305
10. "Optical, morphological and spectroscopic characterization of graphene on SiO<sub>2</sub>", Giannazzo F., **Sonde S.**, Raineri V., Patanè G., Compagnini G., Aliotta F., Ponterio R., Rimini E., PHYSICA STATUS SOLIDI C, vol. 7, p. 1251-1255 (2010).
  - ISSN: 1610-1634, doi: 10.1002/pssc.200982967

## List of Publications

---

11. "Role of graphene/substrate interface on the local electron mean free path in graphene", **Sonde S.**, Vecchio C., Giannazzo F., Yakimova R., Raineri V., Rimini E., APPLIED PHYSICS LETTERS, vol. 97; p. 132101-132103, (2010).
  - ISSN: 0003-6951, doi: 10.1063/1.3489942
  - Also selected for publication on Virtual Journal of Nanoscale Science & Technology.
12. "Effect of graphene/4H-SiC(0001) interface on electrostatic properties in graphene", **Sonde S.**, Vecchio C., Giannazzo F., Yakimova R., Raineri V., Rimini E., submitted to PHYSICA E.
13. "Influence of substrate dielectric permittivity on quantum capacitance in graphene", **Sonde S.**, Vecchio C., Giannazzo F., LoNigro R., Raineri V., Rimini E., submitted to PHYSICA E.
14. "Local electrical properties of the 4H-SiC(0001)/graphene interface", **Sonde S.**, Vecchio C., Giannazzo F., Yakimova R., Rimini E., Raineri V., to be published in MATERIALS SCIENCE FORUM.
15. "Temperature dependent structural evolution of graphene layers on 4H-SiC(0001)", **Sonde S.**, Vecchio C., Giannazzo F., Bongiorno C., Di Franco S., Rambach M., Rimini E., Raineri V., to be published in MATERIALS SCIENCE FORUM.
16. "Nanoscale structural characterization of epitaxial graphene grown on off-axis 4H-SiC (0001)", Vecchio C., Giannazzo F., **Sonde S.**, Yakimova R., Rimini E., Raineri V., submitted to NANOSCALE RESEARCH LETTERS.

## Past publications

1. “Origin and suppression of junction leakage in Germanium-On-Silicon structures”, **Sonde S.**, Simoen E., Claeys C., Satta A., De Jaeger B., Nicholas G., Meuris M., ECS TRANSACTIONS, vol. 6; p. 31-39, (2007).
  - ISSN: 1938-5862, doi: 10.1149/1.2727385
2. “On the origin of the 1/f noise in shallow germanium p+-n junctions”, Todi R. M., **Sonde S.**, Simoen E., Claeys C., Sundaram K. B., APPLIED PHYSICS LETTERS, vol. 90; p. 0435011-0435013 (2007).
  - ISSN: 0003-6951, doi: 10.1063/1.2431759
3. “Processing factors impacting the leakage current and flicker noise of germanium p+-n junctions on silicon substrates”, Simoen E., **Sonde S.**, Claeys C., Satta A., De Jaeger B., Todi R., Meuris M., JOURNAL OF THE ELECTROCHEMICAL SOCIETY, vol. 155; p. 145-150 (2008).
  - ISSN: 0013-4651, doi: 10.1149/1.2823492
4. “Impact of Donor Concentration, Electric Field, and Temperature Effects on the Leakage Current in Germanium p+/n Junctions”, Eneman G., Wiot M., Brugere A., Casain O. S. I., **Sonde S.**, Brunco D. P., De Jaeger B., Satta A., Hellings G., De Meyer K., Claeys C., Meuris M., Heyns M., Simoen E., IEEE TRANSACTIONS ON ELECTRON DEVICES, vol. 55; p. 2287-2296 (2008).
  - ISSN: 0018-9383, doi: 10.1109/TED.2008.927660

## Conference contributions

1. **Symposium on Carbon Nanotubes and Graphene**, 01.04.2009, University of Catania, Italy.
  - Oral: “Graphene on SiC.”
2. **Hetero-SiC’09 and WASMPE’09**, 06.05.2009-08.05.2009, Catania, Italy.
  - Oral: “Nanoscale electrical characterization of graphene on 4H-SiC.”
3. **E-MRS 2009 Spring meeting**, 08.06.2009-12.06.2009, Strasbourg, France.
  - Oral: “Nanoscale capacitive behavior of ion irradiated graphene.”
  - Poster: “Nanoscale electrical characterization of graphene on SiC.”
  - Poster: “Optical, morphological and spectroscopic characterization of graphene on SiO<sub>2</sub>.”
4. **Graphene Week 2010**, 19.04.2010-23.04.2010, University of Maryland, USA.
  - Poster: “Nanoscale electrical properties of graphene/SiC(0001).”
  - Poster: “Local transport properties of pristine and ion irradiated graphene.”
5. **E-MRS 2010 Spring meeting**, 07.06.2010-12.06.2010, Strasbourg, France.
  - Oral: “Electronic transport properties of graphene on 4H-SiC(0001).”
  - Poster: “Electrostatic and transport properties of graphene on STO.”
6. **E-MRS 2010 Fall meeting**, 13.09.2010-16.09.2010, Warsaw, Poland.
  - Oral: “Nanometer scale capacitance measurements as a probe to evaluate local mean free path in graphene.”
7. **CARBOMAT 2010**, 06.10.2010-08.10.2010, Catania, Italy.
  - Oral: “Role of graphene/substrate interface on local transport properties.”

Sushant Sonde, PhD in Nanoscience, Scuola Superiore of the University of Catania, 2010.

# Curriculum vitae

**Sushant Sudam Sonde**

21.10.1980 Born in Pune, India

## Education

1998 – 2002	Bachelor of Engineering (Electrical)	Govt. College of Engineering, University of Pune, India
2005 – 2007	Master of Engineering (Micro – Optoelectronics)	Fachhochschule Deggendorf, Deggendorf, Germany
2008 – 2010	International Ph.D. in Nanoscience	Scuola Superiore di Catania, University of Catania, Italy

## Awards

- **Oberbürgermeister-Dieter-Goerlitz-Preis 2007** conferred by the City of Deggendorf, Germany, in appreciation of outstanding achievements of innovative young people.
- **Young Scientist Award 2009** at the European Material Research Society Spring Meeting 2009, Strasbourg, France.

## Research experience

2005 – 2007	Student research assistant	Fachhochschule Deggendorf, Deggendorf, Germany
Jun 2006 – Nov 2006	International scholar	IMEC vzw, Leuven, Belgium
2008 – 2010	Ph.D. student	CNR – IMM Catania, Italy

## Professional experience

2002 – 2005	Electrical Engineer	Brintons Carpets Asia Pvt. Ltd., Pune, India
-------------	---------------------	----------------------------------------------



# Acknowledgments

This thesis is a result of support, time and energies invested by some very special people. First of all, I am deeply grateful to the Scuola Superiore di Catania and CNR-IMM (Istituto per la Microelettronica e Microsistemi) for providing the facilities and platform to realize this thesis work. The time I spent here has been very special and of immense learning. I would like to express my sincere appreciation and gratitude especially towards,

- Prof. Emanuele Rimini, for giving me the opportunity to perform the study, for his constant encouragement, constructive suggestions and for being a figure of inspiration throughout,
- Dr. Vito Raineri, for being my mentor; for keeping faith in me, despite repeated failures; for always finding time and energy to advise me even on the minutest issues and for giving me an eye for bigger picture,
- Dr. Filippo Giannazzo, for his guidance, help and support from day one, in including extra-technical issues; for being a persistent example of modesty and a paragon of work ethics throughout.

Prof. Rimini, Dr. Raineri and Dr. Giannazzo, thank you for introducing me to Graphene, Scanning Probe Microscopy and thank you for your immense contribution towards my education as a graduate research student. I sincerely acknowledge your support given to me even during the toughest times. My learning with you will definitely go a long way in helping me in my future pursuits. I extend my sincere gratitude towards Dr. Corrado Spinella, the incumbent director of CNR-IMM, Catania and Prof.ssa Maria Grazia Grimaldi, one of the coordinators of the PhD program, for their warm support..

I would also like to acknowledge support and help from my collaborators during the preparation of this thesis work. Prominently, I would like to thank Prof. Giuseppe Compagnini, University of Catania; Prof. Rositza Yakimova, University of Linköping, Sweden; Prof. Jean Camassel, University of Montpellier II, France; Dr. Raffaella LoNigro, CNR-IMM; Dr. Giuseppe D'Arrigo, CNR-IMM; Dott. Salvatore Di Franco, CNR-IMM; Dott. Antonio Marino, CNR-IMM. Additionally, at this time, I would like to acknowledge all my peers for their valuable suggestions at all times.

The entire group members deserve a special mention. Dr. Fabrizio Roccaforte and Dott. Salvatore Di Franco together (and by all means on their own) have been a constant source of witty humor to the group. It has been a pleasure knowing Dr. Patrick Fiorenza, who always interested me with his multifaceted personality, apart from that I appreciate his efforts during my initial AFM training. Dr. Pietro Delugas, Dr. Ming-Hung Weng, the former members of the group; Dott.ssa Alessia Frazzetto, Ing. Carmelo Vecchio and Dott. Giuseppe Greco, the newer members of the group, all have brought new perspectives to me.

I would also like to mention the secretarial staff at Scuola Superiore di Catania, especially Dott.ssa Bice Immè and Dott.ssa Maria Sanfilippo for being warm, considerate and for helping me, at many times, by going out of their ways. Mention also must be made of other colleagues at Scuola Superiore and friends in Catania, in particular, Jens Eriksson and Ioannis Deretzis for their support, suggestions, humor and for helping make a pleasant working/living environment.

A special word of thanks goes to Dott.ssa. Maria Cristina Maugeri and her parents, Signora Graziella and Signor Alfio Maugeri, for introducing me, with enormous patience and affection, to new ways of life. I genuinely appreciate the way they accepted and supported me.

Sushant Sudam Sonde.

Catania, 2010.